JSCSEN 79(3)277–387(2014)

ISSN 1820-7421(Online)

Journal of the Serbian Chemical Society

Electronic Version

VOLUME 79

No 3

BELGRADE 2014

Available on line at

www.shd.org.rs/JSCS/

Journal of the Serbian Chemical Society
JSCS-info@shd.org.rs • www.shd.org.rs/JSCS

J. Serb. Chem. Soc. Vol. 79, No. 3 (2014)

CONTENTS

Published by the Serbian Chemical Society
Karnegijeva 4/III, P. O. Box 36, 11120 Belgrade 35, Serbia
Printed by the Faculty of Technology and Metallurgy
Karnegijeva 4, P. O. Box 35-03, 11120 Belgrade, Serbia

Journal of the Serbian Chemical Society
JSCS-info@shd.org.rs • www.shd.org.rs/JSCS
J. Serb. Chem. Soc. 79 (3) 277–282 (2014)
JSCS–4582
UDC 542.913:547.53.024'861.3+
547.532'78:615.281/.282
Original scientific paper

Synthesis and biological evaluation of 5-substituted derivatives of benzimidazole

VESNA P. VASIĆ[1], JELENA Z. PENJIŠEVIĆ[2], IRENA T. NOVAKOVIĆ[2#], VLADIMIR V. ŠUKALOVIĆ[2], DEANA B. ANDRIĆ[1*] and SLAĐANA V. KOSTIĆ-RAJAČIĆ[2]

[1]*Faculty of Chemistry, University of Belgrade, Studentski trg 12–16, Belgrade, Serbia and* [2]*ICTM – Center of Chemistry, University of Belgrade, Njegoševa 12, Belgrade, Serbia*

(Received 18 April, revised 22 May 2013)

Abstract: A series of eight novel 5-substituted derivatives of benzimidazole was synthesized by condensation of the corresponding diamine with ethyl 4-[4--(2-chlorophenyl)piperazin-1-yl]butanoate in refluxing 4 M hydrochloric acid. *In vitro* antibacterial activity against ten strains, namely *Bacillus subtilis*, *Clostridium sporogenes*, *Streptosporangium longisporum*, *Micrococcus flavus*, *Sarcina lutea*, *Staphylococcus aureus*, *Escherichia coli*, *Pseudomonas aeruginosa*, *Salmonella enteritidis* and *Proteus vulgaris* and antifungal activity against two fungal strains, namely *Candida albicans* and *Saccharomyces cerevisiae*, were evaluated. Of all the compounds screened for activity, 2-{3-[4-(2-chlorophenyl)piperazin-1-yl]propyl}-5-iodo-1*H*-benzimidazole and 2-{3-[4-(2-chlorophenyl)piperazin-1-yl]propyl}-5-methyl-1*H*-benzimidazole were associated with higher antifungal activity than commercial drugs.

Keywords: arylpiperazines; benzimidazoles; antibacterial activity; antifungal activity.

INTRODUCTION

One of the main objectives of organic and medicinal chemistry is the design, synthesis and production of molecules having value as human therapeutic agents.[1–3] The synthesis of nitrogen-containing heterocyclic systems has been attracting interest over the past decade because of their utility in various applications.[4–7] Substituted benzimidazoles and arylpiperazines derivatives have been one of the most extensively studied classes of heterocyclic compounds, receiving much attention from synthetic organic chemists because of their broad spectrum of biological properties, such as antiviral, anticancer, antibacterial, antifungal and many others.[8–11]

* Corresponding author. E-mail: deanad@chem.bg.ac.rs
# Serbian Chemical Society member.
doi: 10.2298/JSC130418058V

These results were an inspiration to synthesize compounds containing a system that involves the combination of these pharmacophores in one molecular framework to give the title structure in order to screen their antimicrobial activities. Resent observations showed that the antimicrobial activities of 4-substituted piperazines varied significantly depending of the substituent group at the 4-piperazine position, suggesting the necessity of an H-bond acceptor and/or donor group at the 4N-position.[12] Prompted by these observations and in continuation the search for bioactive molecules, a series of novel 5-substituted benzimidazoles was designed and synthesized. The design emphasized the strategy of combining two chemically different but pharmacologically compatible molecules, benzimidazole and arylpiperazine, with an alkyl chain that provides hydrophobic interactions and the 2-chlorophenyl group in the piperazine part of the molecule that ensured H-bonding. The aim was to determine the influence of the substituent in the benzimidazole part of the molecule on the antimicrobial activities of the molecules.

EXPERIMENTAL

General

The ^{1}H-NMR and ^{13}C-NMR spectra were recorded at 200 and 50 MHz, respectively, on a Gemini 2000 (Varian, Oxford). The spectra were recorded in deuterochloroform with tetramethylsilane as the internal standard; the chemical shifts (δ) are reported in parts per million (ppm). LC/MS was performed on a 6210 Time-of-Flight LC-MS system (Agilent Technologies, Germany). For data analysis, MassHunter Workstation Software was used.

The infrared (IR) spectra were run on a Thermo Scientific spectrometer. For analytical thin-layer chromatography (TLC), POLYGRAM SIL G/UV$_{254}$ plastic-backed thin-layer silica gel plates were used (Macherey-Nagel, Germany). Chromatographic purifications were performed on Merck-60 silica gel columns (diameter 70 mm, h = 45 mm; the same for all compounds), 230–400 mesh ASTM, under medium pressure (dry column flash chromatography). All reagents and solvents used in this work were obtained from Alfa–Aesar and used without further purification. Solvents were routinely dried over anhydrous Na_2SO_4 prior to evaporation.

Analytic and spectral data for compounds **3** and **20**–**27** are given in the Supplementary material to this paper.

Chemistry

*Synthesis of ethyl 4-[4-(2-chlorophenyl)piperazin-1-yl]butanoate (**3**).* Suspension of 1-(2-chlorophenyl)piperazine monohydrochloride (**2**) (25 g, 107.3 mmol), triethylamine (10.84 g, 107.3 mmol), K_2CO_3 (30 g, 214.6 mmol) and ethyl 4-bromobutanoate (**1**) (20.93 g, 107.3 mmol) in 2-butanone (120 mL) was stirred for 24 h at 80 °C. After cooling, the mixture was poured into cold water and the organic layer was extracted with CH_2Cl_2 and concentrated *in vacuo*. The resulting ester was purified by silica gel column chromatography using a gradient of methanol (0–5 %, predicted by TLC) in dichloromethane. Yield: 22.6 g (68 %).

*General procedure for the reduction of 2-nitroaniline (**4**) and 4-substituted 2-nitroanilines **5**–**11***

Ra/Ni (0.4–0.5 g) was added in small portions to a stirred solution of 6.5 mmol of the required nitro compound (**4**–**11**) in 12 mL EtOH, 12 mL 1,2-dichloroethane and 2 mL (20

mmol) hydrazine hydrate at 30 °C. After completion of the Ra/Ni addition, the mixture was heated in a water bath (50 °C, 60 min) and filtered through celite. The filtrate was evaporated *in vacuo* and crude product used for further syntheses.

*General procedure for the synthesis of 1*H*-benzimidazoles **20**–**27***

Diamines **12**–**19** (5.56 mmol), ester **3** (4.2 g, 13.5 mmol) and 4 M HCl (28 mL) were heated at100 °C for 24 h. After cooling to ambient temperature, the reaction mixture was poured into ice-cold water and neutralized with a saturated solution of sodium hydroxide. The product was extracted with CH_2Cl_2 and concentrated *in vacuo*. The resulting 1*H*-benzimidazoles were purified by silica gel column chromatography using a gradient of methanol (0–5 %) in dichloromethane.

Antimicrobial activity

Sterile 96-well polystyrene microtiter plates with well capacities of 300 µL were used and 100 µL of fresh Mueller Hinton broth were added to each well of the plate. One hundred microliters of a stock solution (10 mg/mL) of the compound in DMSO were added to each well of the first column. Then, 100 µL of the solution were removed from the first column and mixed thoroughly with the broth in the corresponding wells of the second column. Subsequently, a 100 µL aliquot was removed from each well in this column and mixed with contents of the corresponding well of the next column. This doubling dilution was performed in all rows across the plate. Two rows in each plate were used as controls. One row was used as a positive control and contained a broad-spectrum antibiotic, chloramphenicol, to determine the sensitivity of Gram-positive and Gram-negative bacterial species, and the antimycotics nystatin and fluconazole, to determine the sensitivity of the fungal species. The other row contained the solvent (DMSO) as a negative control. In each well of the plate, 10 µL of bacterial cultures (10^6 cells per mL) for antibacterial activity and 10 µL of fungi-cultures (10^5 spores per mL) were inoculated. The microtitre plate was incubated at 37 °C for 24 h for bacteria or at 30 °C for 48 h for the fungi. Subsequently, the bacterial and fungi growth were measured. The *MIC* was determined as the lowest concentration that resulted in inhibition of bacterial and fungal growth.

RESULTS AND DISCUSSION

Synthesis of 5-substituted derivatives of benzimidazole, depicted in Scheme 1, started with the preparation of ethyl 4-[4-(2-chlorophenyl)piperazin-1-yl]butanoate (**3**) from 1-(2-chlorophenyl)piperazine monohydrochloride (**2**) and ethyl 4-bromobutanoate (**1**) in 2-butanone. 2-Nitroaniline (**4**) and 4-substituted 2-nitroanilines **5**–**11** were reduced by Ra-Ni/hydrazine to give the diamines **12**–**19**, which were converted to the benzimidazoles **20**–**27** by condensation with the starting ester **3** in refluxing 4 M HCl.

The micro-broth dilution assay was used to evaluate the antimicrobial efficacy of all newly synthesized compounds against Gram-positive and Gram-negative bacteria and fungal cells. The results are presented in Tables I and II for the antibacterial and antimycotic activities, respectively.[13]

The Gram-positive bacteria used were *Bacillus subtilis* (ATCC 6633), *Clostridium sporogenes* (ATCC 19404), *Streptosporangium longisporum* (ATCC 25212), *Micrococcus flavus* (ATCC 10240), *Sarcina lutea* (ATCC 9341) and *Staphylo-*

coccus aureus (ATCC 6538). The Gram-negative bacteria used were *Escherichia coli* (ATCC 25922), *Pseudomonas aeruginosa* (ATCC 9027), *Salmonella enteritidis* (ATCC 13076) and *Proteus vulgaris* (ATCC 13315). The fungi tested were *Candida albicans* (ATCC 10231) and *Saccharomyces cerevisiae* (ATCC 9763).

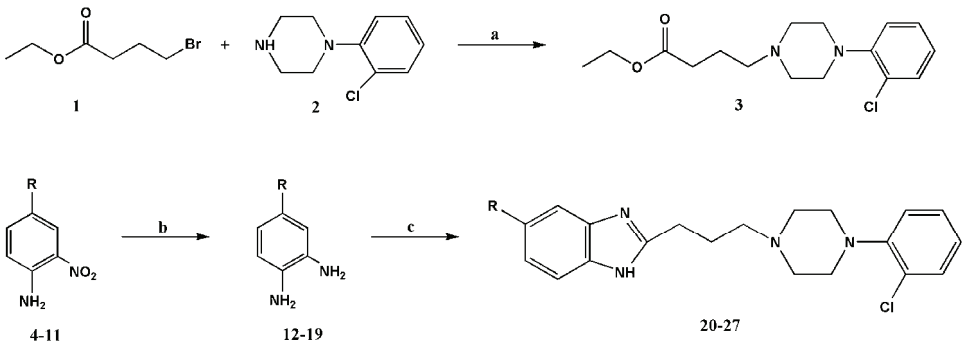

No	20	21	22	23	24	25	26	27
R	H	F	Cl	Br	I	CH_3	CF_3	OCH_3

Scheme 1. Synthesis of 5-substituted derivatives of benzimidazole. Reagents: a) Et_3N, K_2CO_3 and 2-butanone; b) 1,2-dichloroethane, EtOH, NH_2NH_2 and Raney Ni; c) 4 M HCl, ester **3**.

TABLE I. Antibacterial activity (*MIC* / mg mL^{-1}) of compounds **20**–**25**

Bacteria	Compound						
	20	**21**	**22**	**23**	**24**	**25**	Chloramphenicol
B. subtilis	1.250	1.250	1.250	1.250	0.625	0.312	0.015
C. sporogenes	1.250	2.500	1.250	1.250	1.250	1.250	0.250
S. longisporum	1.250	1.250	1.250	1.250	0.625	0.625	0.066
M. flavus	1.250	2.500	1.250	1.250	0.625	0.625	0.031
S. lutea	1.250	1.250	1.250	1.250	0.625	1.250	0.125
S. aureus	1.250	2.500	2.500	0.625	0.312	0.312	0.015
P. vulgaris	1.250	2.500	1.250	1.250	0.625	2.500	0.125
P. aeruginosa	1.250	2.500	2.500	1.250	0.312	2.500	0.250
S. enteritidis	1.250	2.500	2.500	1.250	1.250	1.250	0.043
E. coli	1.250	–	–	0.312	0.625	0.312	0.043

TABLE II. Antifungal activity (*MIC* / mg mL^{-1}) of compounds **20**–**25**

Fungi	Compound							
	20	**21**	**22**	**23**	**24**	**25**	Nystatin	Fluconazole
C. albicans	1.250	1.250	1.250	1.250	0.625	0.078	2.250	0.313
S. cerevisiae	1.250	1.250	1.250	1.250	0.625	0.313	1.250	

Results revealed that, among all the synthesized and tested compounds, compounds **26** and **27** did not show antibacterial activity. The most potent

against the Gram-positive and Gram-negative bacteria were 2-{3-[4-(2-chlorophenyl)piperazin-1-yl]propyl}-5-iodo-1*H*-benzimidazole (**24**) and 2-{3-[4-(2-chlorophenyl)piperazin-1-yl]propyl}-5-methyl-1*H*-benzimidazole (**25**).

A comparison of activity data of all tested compounds and antifungal activity of nystatin and fluconazole indicated that all synthesized derivatives showed the same or better activity against *C. albicans* and *S. cerevisiae* than nystatin (except for 5-(trifluoromethyl) and 5-methoxy derivatives, **26** and **27**, respectively). The 5-methyl derivative **25** was four times more biologically active against *C. albicans* than fluconazole.

CONCLUSIONS

The synthesis of a series of eight novel 2-{3-[4-(2-chlorophenyl)piperazin-1-yl]propyl}-5-substituted-1*H*-benzimidazoles is presented, emphasizing the strategy of combining two chemically different but pharmacologically compatible heterocyclic molecules (benzimidazole and arylpiperazine) in one frame. The synthesized compounds were tested *in vitro* for their antibacterial and antifungal activities. The results indicate that, although the length of the aliphatic chain affects lipophilicity and 2-chlorophenyl group in the piperazine part of molecule provides for H-bonding (properties which are mandatory for antibacterial and antifungal activity), only the substituent in benzimidazole part of the molecule was crucial for the activity. Although the title compounds did not exhibit significant antibacterial activity, all of them (except **26** and **27**) exhibited the same or better antifungal activity than commercial nystatin and fluconazole. In some case of the fungi *C. albicans*, this activity was 4 times higher. More specifically, 5-iodo **24** and 5-methyl **25** derivatives exhibited the best activities against both fungal species.

SUPPLEMENTARY MATERIAL

Analytic and spectral data for compounds **3** and **20**–**27** are available electronically from http:// //www.shd.org.rs/JSCS/, or from the corresponding author on request.

Acknowledgement. These results are part of Project 172032, supported by the Ministry of Education, Science and Technological Development of the Republic of Serbia.

ИЗВОД

СИНТЕЗА И БИОЛОШКО ИСПИТИВАЊЕ 5-СУПСТИТУИСАНИХ ДЕРИВАТА БЕНЗИМИДАЗОЛА

ВЕСНА П. ВАСИЋ[1], ЈЕЛЕНА З. ПЕЊИШЕВИЋ[2], ИРЕНА Т. НОВАКОВИЋ[2], ВЛАДИМИР В. ШУКАЛОВИЋ[2], ДЕАНА Б. АНДРИЋ[1] и СЛАЂАНА В. КОСТИЋ-РАЈАЧИЋ[2]

[1]Хемијски факултет, Универзитет у Београду, Студентски трг 12–16, Београд и [2]ИХТМ – Центар за хемију, Универзитет у Београду, Његошева 12, Београд

Синтетисана је серија од осам нових, 5-супституисаних бензимидазола, конденза-цијом одговарајућег диамина са етил-4-[4-(2-хлорфенил)пиперазин-1-ил]-бутаноатом у 4 M HCl, на температури рефлуктовања. Одређена је *in vitro* антибактеријска активност

на десет сојева, *Bacillus subtilis*, *Clostridium sporogenes*, *Streptosporangium longisporum*, *Micrococcus flavus*, *Sarcina lutea*, *Staphylococcus aureus*, *Escherichia coli*, *Pseudomonas aeruginosa*, *Salmonella enteritidis* и *Proteus vulgaris,* и антифунгална активност на два соја, *Candida albicans* и *Saccharomyces cerevisiae*. Од свих новосинтетисаних једињења за 2-{3-[4-(2--хлорфенил)пиперазин-1-ил]пропил}-5-јод-1*H*-бензимидазол (**24**) и 2-{3-[4-(2-хлорфенил)пиперазин-1-ил]пропил}-5-метил-1*H*-бензимидазол (**25**) се може истаћи да поседују бољу антифунгалну активност од комерцијалних лекова.

(Примљено 18. априла, ревидирано 22. маја 2013)

REFERENCES

1. J. Jin, X.-B. Wang, L.-Y. Kong, *Bioorg. Med. Chem. Lett*. **21** (2011) 909
2. S. Demirayak, U. Abu Mohsen, A. Cagri Karaburun, *Eur. J. Med. Chem*. **37** (2002) 255
3. H. Göker, S. Ozden, S. Yıldız, D. W. Boykin, *Eur. J. Med. Chem.* **40** (2005) 1062
4. A. T. Mavrova, K. K. Anichina, D. I. Vuchev, J. A. Tsenov, M. S. Kondeva, M. K. Micheva, *Bioorg. Med. Chem.* **13** (2005) 5550
5. Z. He, J. Yang, W. Baogen, L. Risen, E. E. Swayze, *Bioorg. Med. Chem. Lett*. **14** (2004) 1217
6. R. A. Ng, J. C. Lanter, V. C. Alford, G. F. Allan, T. Sbriscia, S. G. Lundeen, Z. Sui, *Bioorg. Med. Chem. Lett*. **17** (2007) 1784
7. D. Kumar, M. R. Jacob, M. B. Reynolds, S. M. Kerwin, *Bioorg. Med. Chem*. **10** (2002) 3997
8. O. Cox, H. Jackson, V. A. Vargas, A. Bàez, J. I. Colón, B. C. Gonzalez, M. De León, *J. Med. Chem.* **25** (1982) 1378
9. M. F. Brana, J. M. Castellano, G. Keilhauer, A. Machuca, Y. Martín, C. Redondo, E. Schlick, N. Walker, *Anti-Cancer Drug Des.* **9** (1994) 527
10. K. K. Singh, S. C. Joshi, C. S. Mathela, *Indian J. Chem.* **50** (2011) 196
11. H. Göker, C. Kus¸ D. W. Boykin, S. Yildiz, N. Altanlar, *Bioorg. Med. Chem.* **10** (2002) 2589
12. X. J. Wang, N. Wu, G. J. Du, S. Q. Zhao, M. Zan, I. Q. Gu, *Arch. Pharm. Chem. Life Sci*. **342** (2009) 377
13. NCCLS (National Committee for Clinical Laboratory Standards), *Approval standard document M7-A5*, Vilanova, PA, 2000.

Journal of the Serbian Chemical Society
JSCS@tmf.bg.ac.rs • www.shd.org.rs/JSCS
J. Serb. Chem. Soc. 79 (3) S33–S36 (2014) *Supplementary material*

SUPPLEMENTARY MATERIAL TO

Synthesis and biological evaluation of 5-substituted derivatives of benzimidazole

VESNA P. VASIĆ[1], JELENA Z. PENJIŠEVIĆ[2], IRENA T. NOVAKOVIĆ[2], VLADIMIR V. ŠUKALOVIĆ[2], DEANA B. ANDRIĆ[1]* and SLAĐANA V. KOSTIĆ-RAJAČIĆ[2]

[1]*Faculty of Chemistry, University of Belgrade, Studentski trg 12–16, Belgrade, Serbia and* [2]*ICTM – Center of Chemistry, University of Belgrade, Njegoševa 12, Belgrade, Serbia*

J. Serb. Chem. Soc. 79 (3) (2014) 277–282

ANALYTIC AND SPECTRAL DATA FOR COMPOUNDS **3** AND **20**–**27**

*Ethyl 4-[4-(2-chlorophenyl)piperazin-1-yl]butanoate (**3**).* ^{1}H-NMR (200 MHz, $CDCl_3$, δ / ppm): 1.26 (3H, *t*, *J* = 6.6 Hz, CH_3), 1.85 (2H, *m*, CH_2), 2.33––2.48 (4H, *m*, CH_2COO and CH_2N), 2.63 (4H, *t*, *J* = 4.6 Hz, CH_2), 3.07 (4H, *t*, *J* = 5.0 Hz, CH_2), 4.16 (2H, *q*, *J* = 7.4 Hz, OCH_2), 6.91–7.37 (4H, *m*, 2-chlorophenyl group); ^{13}C-NMR (50 MHz, $CDCl_3$, δ / ppm): 14.15 (1C, CH_3), 22.09 (1C, CH_2), 32.19 (1C, **C**H_2COO), 51.13 (2C, CH_2), 53.18 (2C, CH_2), 57.57 (1C, CH_2N), 60.18 (1C, OCH_2), 120.26 (1C, CH–C_6, 2-chlorophenyl-group), 123.50 (1C, CH–C_4, 2-chlorophenyl-group), 127.49 (1C, CH–C_5, 2-chlorophenyl group), 128.67 (1C, C–C_2, 2-chlorophenyl group), 130.55 (1C, CH–C_3, 2-chlorophenyl group), 149.28 (1C, C–C_1, 2-chlorophenyl group), 173.50 (1C, CO).

*2-{3-[4-(2-Chlorophenyl)piperazin-1-yl]propyl}-1*H*-benzimidazole (**20**).* Yield: 579 mg (29 %); IR (ATR, cm^{-1}): 2957, 1617, 1588, 1480, 1234; ^{1}H-NMR: (200 MHz, $CDCl_3$, δ / ppm): 2.04 (2H, *m*, CH_2), 2.65 (2H, *t*, *J* = 5.6 Hz, CH_2N), 2.74 (4H, *t*, *J* = 5.2 Hz, CH_2), 3.08 (2H, *t*, *J* = 6.6 Hz, CH_2), 3.17 (4H, *t*, *J* = 4.4 Hz, CH_2), 6.97–7.59 (8H, *m*, 2-chlorophenyl group and benzimidazole), 9.64 (1H, *bs*, NH); ^{13}C-NMR (50 MHz, $CDCl_3$, δ / ppm): 23.52 (1C, CH_2), 29.08 (1C, CH_2), 51.13 (2C, CH_2), 53.29 (2C, CH_2), 58.79 (1C, CH_2N), 114.58 (2C, CH–C_4 and CH–C_7, benzimidazole), 120.19 (1C, CH–C_6, 2-chlorophenyl group), 121.79 (2C, CH–C_5 and C_6, benzimidazole), 124.01 (1C, CH–C_4, 2-chlorophenyl-group), 127.72 (1C, CH–C_5, 2-chlorophenyl-group), 128.80 (1C, C–C_2, 2-chlorophenyl-group), 130.75 (1C, CH–C_3, 2-chlorophenyl-group), 138.92 (2C, C–C_{3a} and C–C_{7a}, benzimidazole), 148.83 (1C, C–C_1, 2-chlorophenyl group), 155.51 (1C, C–C_2, benzimidazole); MS (*m*/*z*): 355.16927 ([M+H]$^+$, $C_{20}H_{23}ClN_4$).

* Corresponding author. E-mail: deanad@chem.bg.ac.rs

*2-{3-[4-(2-Chlorophenyl)piperazin-1-yl]propyl}-5-fluoro-1*H-*benzimidazole* ***(21)***. Yield: 1.38 g (96 %); IR (ATR, cm^{-1}): 2955, 1629, 1591, 1480, 1235; ^{1}H-NMR (200 MHz, $CDCl_3$, δ / ppm): 2.04 (2H, *m*, CH_2), 2.70 (2H, *t*, *J* = 5.6 Hz, CH_2N), 2.80 (4H, *t*, *J* = 4.9 Hz, CH_2), 3.12 (2H, *t*, *J* = 6.2 Hz, CH_2), 3.21 (4H, *t*, *J* = 4 Hz, CH_2), 6.89–7.42 (7H, *m*, 2-chlorophenyl group and benzimidazole), 13.06 (1H, *bs*, NH); ^{13}C-NMR (50 MHz, $CDCl_3$, δ / ppm): 23.07 (1C, CH_2), 29.61 (1C, CH_2), 51.24 (2C, CH_2), 53.38 (2C, CH_2), 59.08 (1C, CH_2N), 109.57 (1C, CH–C_4, benzimidazole), 110.08 (1C, CH–C_6, benzimidazole), 120.07 (1C, CH–C_7, benzimidazole), 120.17 (1C, CH–C_6, 2-chlorophenyl group), 124.17 (1C, CH–C_4, 2-chlorophenyl-group), 127.82 (1C, CH–C_5, 2-chlorophenyl group), 128.85 (1C, C–C_2, 2-chlorophenyl group), 130.84 (1C, CH–C_3, 2-chlorophenyl group), 136.40 (1C, C–C_{7a}, benzimidazole), 138.80 (1C, C–C_{3a}, benzimidazole), 148.72 (1C, C–C_1, 2-chlorophenyl group), 156.78 (1C, C–C_2, benzimidazole), 161.48 (1C, C–C_5, benzimidazole); MS (*m*/*z*): 373.15986 ($[M+H]^+$, $C_{20}H_{22}ClFN_4$).

*5-Chloro-2-{3-[4-(2-chlorophenyl)piperazin-1-yl]propyl}-1*H-*benzimidazole* ***(22)***. Yield: 58 mg (11 %); IR (ATR, cm^{-1}): 2951, 1618, 1586, 1477, 1232; ^{1}H-NMR (200 MHz, $CDCl_3$, δ / ppm): 2.05 (2H, *m*, CH_2), 2.70 (2H, *t*, *J* = 5 Hz, CH_2N), 2.80 (4H, *t*, *J* = 4.9 Hz, CH_2), 3.13 (2H, *t*, *J* = 6 Hz, CH_2), 3.21 (4H, *t*, *J* = 4.2 Hz, CH_2), 7.00–7.52 (7H, *m*, 2-chlorophenyl group and benzimidazole), 13.00 (1H, *bs*, NH); ^{13}C-NMR (50 MHz, $CDCl_3$, δ / ppm): 23.11 (1C, CH_2), 29.37 (1C, CH_2), 51.16 (2C, CH_2), 53.31 (2C, CH_2), 58.92 (1C, CH_2N), 114.47 (2C, CH–C_4 and CH–C_7, benzimidazole), 120.19 (1C, CH–C_6, 2-chlorophenyl group), 122.24 (1C, CH–C_6, benzimidazole), 124.16 (1C, CH–C_4, 2-chlorophenyl group), 127.27 (1C, CH–C_5, 2-chlorophenyl group), 127.80 (1C, C–C_5, benzimidazole), 128.82 (1C, C–C_2, 2-chlorophenyl group), 130.80 (1C, CH–C_3, 2-chlorophenyl group), 138.80 (2C, C–C_{3a} and C–C_{7a}, benzimidazole), 148.68 (1C, C–C_1, 2-chlorophenyl group), 156.77 (1C, C–C_2, benzimidazole); MS (*m*/*z*): 389.12990 ($[M+H]^+$, $C_{20}H_{22}Cl_2N_4$).

*5-Bromo-2-{3-[4-(2-chlorophenyl)piperazin-1-yl]propyl}-1*H-*benzimidazole* ***(23)***. Yield: 154 mg (27 %); IR (ATR, cm^{-1}): 2954, 1617, 1587, 1479, 1232; ^{1}H-NMR (200 MHz, $CDCl_3$, δ / ppm): 2.04 (2H, *m*, CH_2), 2.68 (2H, *t*, *J* = 5.6 Hz, CH_2N), 2.79 (4H, *t*, *J* = 5.2 Hz, CH_2), 3.10 (2H, *t*, *J* = 4.6 Hz, CH_2), 3.16 (4H, *t*, *J* = 4.6 Hz, CH_2), 6.99–7.78 (7H, *m*, 2-chlorophenyl group and benzimidazole), 9.09 (1H, *bs*, NH); ^{13}C-NMR (50 MHz, $CDCl_3$, δ / ppm): 23.32 (1C, CH_2), 29.19 (1C, CH_2), 51.11 (2C, CH_2), 53.33 (2C, CH_2), 58.87 (1C, CH_2N), 114.60 (2C, CH–C_4 and CH–C_7, benzimidazole), 120.22 (1C, CH–C_6, 2-chlorophenyl group), 121.86 (1C, C–C_5, benzimidazole), 124.12 (1C, CH–C_4, 2-chlorophenyl group), 124.87 (1C, CH–C_6, benzimidazole), 127.78 (1C, CH–C_5, 2-chlorophenyl group), 128.85 (1C, C–C_2, 2-chlorophenyl-group), 130.80 (1C, CH–C_3, 2-chlorophenyl group), 138.92 (2C, C–C_{3a} and C–C_{7a}, benzimidazole), 148.77

(1C, C–C_1, 2-chlorophenyl group), 156.62 (1C, C–C_2, benzimidazole). MS (*m*/*z*): 433.07952 ($[M+H]^+$, $C_{20}H_{22}BrClN_4$).

*2-{3-[4-(2-Chlorophenyl)piperazin-1-yl]propyl}-5-iodo-1*H-*benzimidazole* ***(24)***. Yield: 333 mg (61 %); IR (ATR, cm^{-1}): 2956, 1618, 1590, 1480, 1233; ^{1}H--NMR (200 MHz, $CDCl_3$, δ / ppm): 2.04 (2H, *m*, CH_2), 2.66 (2H, *t*, *J* = 5.6 Hz, CH_2N), 2.75 (4H, *t*, *J* = 5.2 Hz, CH_2), 3.12 (2H, *t*, *J* = 6.2 Hz, CH_2), 3.20 (4H, *t*, *J* = 6.2 Hz, CH_2), 6.94–7.59 (6H, *m*, 2-chlorophenyl group and benzimidazole), 7.87 (1H, *s*, C_4 benzimidazole), 9.08 (1H, *bs*, NH); ^{13}C-NMR (50 MHz, $CDCl_3$, δ / ppm): 23.47 (1C, CH_2), 29.08 (1C, CH_2), 51.13 (2C, CH_2), 53.29 (2C, CH_2), 58.81 (1C, CH_2N), 95.01 (1C, C–C_5, benzimidazole), 114.58 (1C, CH–C_7, benzimidazole), 120.21 (1C, CH–C_6, 2-chlorophenyl group), 121.84 (1C, CH–C_4, benzimidazole), 124.05 (1C, CH–C_4, 2-chlorophenyl-group), 127.74 (1C, CH–C_5, 2-chlorophenyl group), 128.82 (1C, C–C_2, 2-chlorophenyl group), 130.78 (2C, CH–C_3, 2-chlorophenyl group and CH–C_6 benzimidazole), 138.90 (2C, C–C_{3a} and C–C_{7a}, benzimidazole), 148.81 (1C, C–C_1, 2-chlorophenyl group), 155.51 (1C, C–C_2, benzimidazole); MS (*m*/*z*): 481.06633 ($[M+H]^+$, $C_{20}H_{22}ClIN_4$).

*2-{3-[4-(2-Chlorophenyl)piperazin-1-yl]propyl}-5-methyl-1*H-*benzimidazole* ***(25)***. Yield: 559 mg (29 %); IR (ATR, cm^{-1}): 2948, 1629, 1538, 1479, 1230; ^{1}H--NMR (200 MHz, $CDCl_3$, δ / ppm): 2.03 (2H, *m*, CH_2), 2.45 (3H, *s*, CH_3), 2.66 (2H, *t*, *J* = 5.6 Hz, CH_2N), 2.77 (4H, *t*, *J* = 5.2 Hz, CH_2), 3.10 (2H, *t*, *J* = 6.2 Hz, CH_2), 3.20 (4H, *t*, *J* = 4.8 Hz, CH_2), 7.00–7.45 (7H, *m*, 2-chlorophenyl group and benzimidazole), 9.22 (1H, *bs*, NH); ^{13}C-NMR (50 MHz, $CDCl_3$, δ / ppm): 21.59 (1C, CH_3), 23.43 (1C, CH_2), 29.15 (1C, CH_2), 51.18 (2C, CH_2), 53.35 (2C, CH_2), 58.85 (1C, CH_2N), 114.45 (2C, CH–C_4 and CH–C_7, benzimidazole), 120.24 (1C, CH–C_6, 2-chlorophenyl group), 123.25 (1C, CH–C_6, benzimidazole), 124.07 (1C, CH–C_4, 2-chlorophenyl group), 127.74 (1C, CH–C_5, 2-chlorophenyl group), 128.87 (1C, C–C_2, 2-chlorophenyl group), 130.82 (1C, CH–C_3, 2-chlorophenyl group), 131.55 (1C, C–C_5, benzimidazole), 138.80 (2C, C–C_{3a} and C–C_{7a}, benzimidazole), 148.86 (1C, C–C_1, 2-chlorophenyl group), 155.09 (1C, C–C_2, benzimidazole); MS (*m*/*z*): 369.18450 ($[M+H]^+$, $C_{21}H_{25}ClN_4$).

*2-{3-[4-(2-Chlorophenyl)piperazin-1-yl]propyl}-5-(trifluoromethyl)-1*H-*-benzimidazole* ***(26)***. Yield: 640 mg (78 %); IR (ATR, cm^{-1}): 2944, 1632, 1590, 1481, 1234; ^{1}H-NMR (200 MHz, $CDCl_3$, δ / ppm): 2.06 (2H, *m*, CH_2), 2.74 (2H, *t*, *J* = 5 Hz, CH_2N), 2.84 (4H, *t*, *J* = 5 Hz, CH_2), 3.15 (2H, *t*, *J* = 6.2 Hz, CH_2), 3.22 (4H, *t*, *J* = 5 Hz, CH_2), 7.01–7.69 (6H, *m*, 2-chlorophenyl group and benzimidazole), 7.83 (1H, *s*, C_4 benzimidazole), 9.05 (1H, *bs*, NH); ^{13}C-NMR (50 MHz, $CDCl_3$, δ / ppm): 22.89 (1C, CH_2), 29.51 (1C, CH_2), 51.15 (2C, CH_2), 53.33 (2C, CH_2), 58.92 (1C, CH_2N), 112.65 (1C, CH–C_4, benzimidazole), 114.38 (1C, CH–C_7, benzimidazole), 118.89 (1C, CH–C_6, 2-chlorophenyl group), 120.19 (1C, CH–C_6, benzimidazole), 122.24 (1C, CF_3), 123.83 (1C, C–C_5, benzimidazole), 124.30 (1C, CH–C_4, 2-chlorophenyl group), 127.85 (1C,

CH–C_5, 2-chlorophenyl group), 128.89 (1C, C–C_2, 2-chlorophenyl group), 130.86 (1C, CH–C_3, 2-chlorophenyl group), 138.20 (2C, C–C_{3a} and C–C_{7a}, benzimidazole), 148.61 (1C, C–C_1, 2-chlorophenyl group), 157.99 (1C, C–C_2, benzimidazole). MS (*m*/*z*): 423.15682 ($[M+H]^+$, $C_{21}H_{22}ClF_3N_4$).

*2-{3-[4-(2-Chlorophenyl)piperazin-1-yl]propyl}-5-methoxy-1*H-*benzimidazole (**27**)*. Yield: 178 mg (71 %); IR (ATR, cm^{-1}): 2948, 1631, 1590, 1483, 1232; ^{1}H-NMR (200 MHz, $CDCl_3$, δ / ppm): 2.04 (2H, *m*, CH_2), 2.67 (2H, *t*, *J* = 5.6 Hz, CH_2N), 2.80 (4H, t, *J* = 5.4 Hz, CH_2), 3.09 (2H, *t*, *J* = 6.2 Hz, CH_2), 3.19 (4H, *t*, *J* = 4.6 Hz, CH_2), 3.82 (3H, *s*, OCH_3), 6.82–7.45 (7H, *m*, 2-chlorophenyl group and benzimidazole), 9.01 (1H, *bs*, NH); ^{13}C-NMR (50 MHz, $CDCl_3$, δ / / ppm): 23.34 (1C, CH_2), 28.71 (1C, CH_2), 50.93 (2C, CH_2), 53.20 (2C, CH_2), 55.81 (1C, OCH_3), 58.56 (1C, CH_2N), 97.83 (1C, CH–C_4, benzimidazole), 111.03 (1C, CH–C_6, benzimidazole), 115.05 (1C, CH–C_7, benzimidazole), 120.21 (1C, CH–C_6, 2-chlorophenyl group), 124.14 (1C, CH–C_4, 2-chlorophenyl group), 127.74 (1C, CH–C_5, 2-chlorophenyl group), 128.82 (1C, C–C_2, 2-chlorophenyl group), 130.78 (1C, CH–C_3, 2-chlorophenyl group), 133.41 (1C, C–C_{7a}, benzimidazole), 139.16 (1C, C–C_{3a}, benzimidazole), 148.70 (1C, C–C_1, 2-chlorophenyl group), 155.00 (1C, C–C_2, benzimidazole), 155.96 (1C, C–C_5, benzimidazole); MS (*m*/*z*): 385.17957 ($[M+H]^+$, $C_{21}H_{25}ClN_4O$).

Journal of the Serbian Chemical Society
JSCS-info@shd.org.rs • www.shd.org.rs/JSCS
J. Serb. Chem. Soc. *79* (3) 283–289 (2014) UDC 547.495.2+547.496.3+542.913:57:615.27
JSCS–4583 *Original scientific paper*

Synthesis and biological evaluation of novel urea and thiourea derivatives of valaciclovir

VENKATA RAMANA KATLA[1], RASHEED SYED[1], MADHAVA GOLLA[1], ADAM SHAIK[2] and NAGA RAJU CHAMARTHI[1]*

[1]*Department of Chemistry, Sri Venkateswara University, Tirupati - 517 502, India and* [2]*Department of Biochemistry, Sree Vidyaniketan P.G College, Tirupati - 517 502, India*

(Received 12 July, revised 4 September 2012)

Abstract: Series of novel urea and thiourea derivatives of valaciclovir were efficiently synthesized in high yields and their antiviral activity was evaluated. (*S*)-2-[(2-amino-6-oxo-6,9-dihydro-3*H*-purin-9-yl)methoxy]ethyl 2-amino-3-methylbutanoate (valaciclovir) (**1**) was reacted with various aromatic isocyanates/thiocyanates **2a**–**j** in the presence of *N*,*N*´-dimethyl piperazine as a base in THF:pyridine (4:1) to obtain the valaciclovir urea/thiourea derivatives **3a**–**j**. The structures of the title compounds (**3a**–**j**) were confirmed by their IR, NMR (^{1}H and ^{13}C) mass spectral data and elemental analysis. The newly synthesized compounds were screened for their antiviral activity against Tobacco mosaic virus (TMV) and antioxidant activity was evaluated by the 1,1-diphenyl-2-picrylhydrazyl radical (DPPH) and superoxide dismutase (SOD) scavenging methods. The title compounds exhibited potent antiviral and good antioxidant activities.

Keywords: isocyanate; isothiocyanate; *N*,*N*´-dimethylpiperazine; tobacco mosaic virus; antiviral activity; antioxidant activity.

INTRODUCTION

Urea and thiourea are important functional groups in numerous natural products and drug intermediates, and are used as neutral receptor for various anions (anion complexation),[1] and building blocks for various heterocycles. Urea and thiourea derivatives possess many promising biological activities, such as herbicidal,[2] antimicrobial,[3] antioxidant,[4] antiviral[5], anti-HIV[6] and antitumor[7] activity, while urea derivatives exhibit anti-inflammatory,[8] antimalarial[9] and antidiabetic activities.[10] Thiourea and urea derivatives have been used as purification agents for organic and inorganic effluents, industrial, agricultural and mining wastes,[11] spinning mixtures, paper and paints, as well as wrinkle proofing agents for cotton and cotton polyester fabrics.[12,13] These compounds could also be used for the

* Corresponding author. E-mail: rajuchamarthi10@gmail.com
doi: 10.2298/JSC120716095K

detoxification of super antigens from body fluids[14] and for the treatment of hemoglobinopathies in the cases of sickle cell anemia and Beta (β) thalassemia,[15] and thiourea derivatives were reported to be non-nucleoside inhibitors (NNIs) of the reverse transcriptase (RT) enzyme of the human immunodeficiency virus (HIV).[16] Thiocarlide is a pharmacologically important thiourea drug used as a therapeutic agent in the treatment of tuberculosis.[17] Thiourea inhibitors of plant viruses have also given rise to widespread interest in both the biological and chemical sectors.[18]

Valaciclovir is a prodrug that is used for viral infection. Valaciclovir is an esterified version of acyclovir that has greater oral bioavailability (about 55 %) than acyclovir (10–20 %). Specific antivirals are used for specific viruses. Unlike most antibiotics, antiviral drugs do not destroy their target pathogen; instead, they inhibit their development. Hence, the design of a safe and effective drug requires extended knowledge of the genetic and molecular functions of organisms. Hence, researchers have been focusing on the development of effective antiviral drugs by embedding effective pharmocophores into origin drugs or on the understanding of the structure and function of viruses to find new drugs. In recent years, the impact of climate anomalies and the areas of crops affected by plant virus diseases are on the rise, resulting in tremendous economic losses in the world. Tobacco mosaic virus (TMV) disease is an important class of common disease occurring in tobacco plants growing all over the world. In continuation of ongoing research work, novel urea and thiourea derivatives of valaciclovir have been designed, synthesized and tested against tobacco mosaic virus and antioxidant activity.

EXPERIMENTAL

Sigma-Aldrich, Merck and Lancaster chemicals were used as such without further purification. Solvents used for spectroscopic and other physical studies were reagent grade and were further purified by literature methods.[19] Melting points were determined by Guna Digital Melting Point apparatus using a calibrated centigrade thermometer and are uncorrected. IR spectra were obtained in KBr optics on a Perkin-Elmer Model 281-B spectrophotometer and expressed in wave numbers (cm^{-1}). ^{1}H- and ^{13}C-NMR spectra were recorded in DMSO-d_6 on a Bruker Avance III 500 MHz spectrometer operating at 500 MHz for ^{1}H-, 125 MHz for ^{13}C--NMR. The ^{1}H- and ^{13}C-chemical shifts were expressed in ppm with reference to tetramethylsilane. ESI mass spectra were recorded on a Finnigan MAT 1020 mass spectrometer. Elemental analyses were performed at University of Hyderabad, India.

Analytic and spectral data for compounds **3a**–**j** are given in the Supplementary material to this paper.

*General procedure for synthesis of title compounds **3a–j***

(*S*)-2-[(2-Amino-6-oxo-6,9-dihydro-3*H*-purin-9-yl)methoxy]ethyl 2-amino-3-methylbutanoate (valaciclovir) **1** (0.001 mol), various aromatic isocyanates/thiocyanates **2a**–**j** (0.001 mol) were dissolved in dry THF:pyridine (20 mL) and refluxed under stirring for 3–5 h at

about 60 °C. Identification of the product and completion of the reaction was monitored by TLC using ethyl acetate:hexane (4:1) as an eluent. After completion of the reaction, the mixture was concentrated on a rotary-evaporator and the residue was purified by column chromatography on silica gel (100–200 mesh) using petroleum ether:ethyl acetate (2:3, boiling range: 40–60 °C) as an eluent. The structures of the title compounds **3a**–**j** were established by spectral and elemental analysis. The obtained yields of **3a**–**j** were in the range 72–82 %.

Antiviral bioassay

Purification of tobacco mosaic virus (TMV). Using the Gooding method,[20] the upper leaves of *Nicotiana tabacum* L. inoculated with TMV were selected and ground in phosphate buffer, 6×10^{-3} mg/mL, pH 7.4, then filtered through a double layer pledget. The filtrate was centrifuged at 10000 g, treated twice with poly(ethylene glycol) 400 (PEG 400) and centrifuged. The whole procedure was performed at 4 °C. The absorbance values, A_{260}, were estimated at 260 nm using an ultraviolet spectrophotometer. The virus concentration is given:

$$\text{Virus concentration} = \frac{A_{260} \times \text{dilution ratio}}{\varepsilon_{0.1\ \%,\ 260\ \text{nm}} \times 1\ \text{cm}} \times 100 \quad (1)$$

Curative effect of the compounds against TMV in vivo. Growing leaves of *Nicotiana tabacum* L. of the same age were selected. TMV (concentration of 6×10^{-3} mg mL) was dipped and inoculated on the whole leaves, then the leaves were washed with water and dried. The compound solution (500 μg mL^{-1}) was smeared on the left side and the solvent was smeared on the right side for control. The local number of lesions were then counted and recorded 3–4 days after inoculation.[21] Triplicated experiments were carried out for each compound and average value was taken as final result. The inhibition rate of the compound was then calculated according to the formula:

$$\text{Inhibition rate} = 100(x-y)/x \quad (2)$$

where x = average local lesion no. of control and y = average local lesion no. of tested sample.

Antioxidant activity

The anti-oxidant activities of the synthesized compounds were evaluated 1,1-diphenyl-2--picrylhydrazyl (DPPH) and superoxide radical scavenging activity methods.

DPPH radical-scavenging activity. The DPPH radical scavenging activity was measured in a reaction mixture containing 0.2 mL of DPPH (1 mM) solution, 0.8 mL of methanol (99 %) and 2 mL of tested solutions (100 μg/mL). The solution was rapidly mixed and scavenging capacity was calculated by observing the decrease in absorbance at 517 nm of the reaction mixture after half an hour at ambient temperature.[22] The percentage of DPPH radical scavenging activity was calculated by the following formula:

$$\text{DPPH radical scavenging activity (\%)} = \left(1 - \frac{A_{517(\text{sample})}}{A_{517(\text{control})}}\right) \times 100 \quad (3)$$

Ascorbic acid was used as a standard for comparison of the activity. The experiments were repeated in triplicate and the average value was taken as the final result.

Superoxide radical scavenging activity (SRSA). Superoxide radicals were identified by a spectrophotometric method to study the effect of various concentrations of the test compounds on the reduction of nitroblue tetrazolium (NBT), according to a previously described procedure.[23] The superoxide radicals were generated in a non-enzymatic phenazine metho-sulfate–nicotinamide adenine dinucleotide (PMS/NADH) system. The non-enzymatic

generation of superoxide radicals was measured in reaction mixtures containing 3 mL of 100 μg mL^{-1} solution of test compounds, 400 μL of PMS (15 μM), 1 ml of NADH (460 μM) and 1 ml of NBT (150 μM) in phosphate buffer (20 mM, pH 7.4), and then incubated for 5 min at ambient temperature. The change in absorbance was read at 560 nm against blank samples. The percentage of superoxide radical scavenging activity was measured using the Eq. (3). Ascorbic acid was used as a standard.

RESULTS AND DISCUSSION

Chemistry

The synthesis of title compounds was accomplished by reacting (*S*)-2-[(2--amino-6-oxo-6,9-dihydro-3*H*-purin-9-yl)methoxy]ethyl 2-amino-3-methylbutanoate (valaciclovir, **1**) with various isocynates/isothiocynates **2a**–**j** in the presence of *N*,*N*´-dimethylpiperazine as a base in THF:pyridine solvent (20 mL) at 60 °C. The progress of the reaction was monitored by TLC. The resulting title compounds **3a**–**j** were obtained in high yields in 3–5 h (Scheme 1). The chemical structures of the title compounds **3a**–**j** were deduced by IR, NMR (^{1}H and ^{13}C), mass spectral and elemental analysis, the results of which are given in the Supplementary material to this paper. IR absorptions bands for **3a**–**j** were observed in the regions 1183–1206, 1648–1672 and 3412–3448 cm^{-1}, assigned to C=S, C=O and N–H, respectively. The ^{1}H-NMR spectra exhibited broad signals for NH protons at 10.8–12.4 ppm. ^{13}C-NMR chemical shifts were observed in the δ regions 166.8–182.4 ppm for C=S and 148.4–152.6 for C=O.

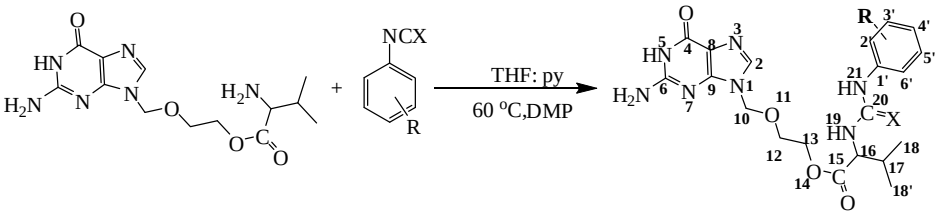

1 **2** DMP- 1,4 Dimethylpiperzine **3(a-j)**

Compound	R	X	Compound	R	X
3a	H	S	**3f**	4-Br	O
3b	4-F	S	**3g**	4-F	O
3c	4-Cl	S	**3h**	3-Cl, 4-Cl	O
3d	4-NO_2	S	**3i**	3-Cl, 4-F	O
3e	3-Br	S	**3j**	3-CF_3, 4-Cl	O

Scheme 1. Synthesis of urea and thiourea derivatives of valaciclovir (**3a**–**j**).

Antiviral activity

The newly synthesized derivatives **3a**–**j** were screened for their antiviral activity against tobacco mosaic virus (TMV) by the Gooding method.[20] The bioassay results obtained at 500 μg mL^{-1} of the synthesized compounds and vala-

ciclovir as the positive control are shown in Table I. It is clear that the title compounds **3a**–**j** showed high antiviral activities against the tobacco mosaic virus. Among the compounds **3a**–**j**, thiourea derivative **3a** bind to phenyl ring and **3e** bearing 3-bromophenyl ring exhibited high TMV inhibition.

TABLE I. TMV inhibitory activity of title compounds **3a**–**j** in concentration of 500 μg mL^{-1}

Compound	Inhibition rate, %
3a	87.2±0.06
3b	84.4±0.12
3c	82.3±0.14
3d	79.1±0.17
3e	89.2±0.05
3f	83.2±0.08
3g	80.4±0.13
3h	78.1±0.09
3i	85.4±0.07
3j	77.2±0.02
Valaciclovir (positive control)	91.3±0.05

Antioxidant activity

Antioxidant activity of the synthesized compounds **3a**–**j** was investigated using DPPH and SRSA scavenging activity methods and the percentage of the scavenging activity are shown in Table II. The bio-screening data revealed that all the title compounds showed potent to moderate antioxidant activity in tested methods.In tested methods, valaciclovir thiourea derivative **3a** bearing phenyl ring, **3e** bonded to 3-bromophenyl ring, urea derivative **3f** containing 4-brom-o-phenyl ring and **3i** attached to 3-chloro-4-flourophenyl ring exhibited promising antioxidant activity quite close to the standard, ascorbic acid. In overall observation of the antioxidant activity of the synthesized compounds, thiourea derivatives showed better activity than urea derivatives.

TABLE II. Antioxidant activities (%) of the title compounds **3**(**a**–**j**)

Entry	DPPH	SRSA
3a	79.5±1.3	75.1±1.7
3b	72.3±1.4	71.1±1.6
3c	73.131.2	70.5±1.6
3d	75.5±1.8	71.0±1.9
3e	81.7±1.1	76.2±1.4
3f	78.0±1.4	74.6±1.1
3g	74.9±1.2	72.4±1.6
3h	71.9±1.7	69.1±1.9
3i	76.8±1.1	70.8±1.7
3j	70.7±1.6	68.6±1.0
Ascorbic acid	83.4±1.6	78.5±1.4

CONCLUSIONS

Synthesis of (*S*)-2-[(2-amino-6-oxo-6,9-dihydro-3*H*-purin-9-yl)methoxy]ethyl 2-amino-3-methylbutanoate (valaciclovir) derivatives of thiourea and urea was accomplished by reacting various aromatic isocyanates/thiocyanates in the presence of *N*,*N*´-dimethylpiperazine as a base in high yields (72–82 %) and in short reaction times. The obtained compounds exhibited good antiviral and promising antioxidant activities.

SUPPLEMENTARY MATERIAL

Analytic and spectral data for compounds **3a**–**j** are available electronically from http://www.shd.org.rs/JSCS/, or from the corresponding author on request.

Acknowledgement. The authors express their grateful thanks to DST-PURSE Program, S. V. University, Tirupati, India, for giving financial assistance through DST-PURSE, JRF-Fellowship.

И З В О Д

СИНТЕЗА И БИОЛОШКА АКТИВНОСТ УРЕА И ТИОУРЕА ДЕРИВАТА ВАЛАЦИКЛОВИРА

VENKATA RAMANA KATLA[1], RASHEED SYED[1], MADHAVA GOLLA[1], ADAM SHAIK[2] и NAGA RAJU CHAMARTHI[1]

[1]*Department of Chemistry, Sri Venkateswara University, Tirupati - 517 502, India и* [2]*Department of Biochemistry, Sree Vidyaniketan P.G College, Tirupati - 517 502, India*

Синтетисана је серија уреа и тиоуреа деривата валацикловира и испитивана је њихова активност. (*S*)-2-[(2-Амино-6-оксо-6,9-дихидро-3*H*-пурин-9-ил)метокси]етил-2--амино-3-метилбутаноат (валацикловир) је реаговао са различитим ароматичним изоцијанатима/тиоцијанатима у присуству *N*,*N*´-диметилпиперазина дајући уреа/тиоуреа деривате валациколовира. Структуре добијених једињења су утврђене методама IR, NMR (^{1}H и ^{13}C), MS и елементалном анализом. За новосинтетисана једињења испитана је активност спрам вируса мозаика дувана (TMV), као и антиоксидативна активност методама ца примрном 1,1-дифенил-2-пикрилхидразил радикала (DPPH) и супероксид-дисмутазе (SOD). Сва једињења су испољила значајну антивирусну и антиоксидативну активност.

(Примљено 12. јула, ревидирано 4. септембра 2012)

REFERENCES

1. Y. Tobe, S. I. Sasaki, M. Mizuno, K. Hirose, K. Neamura, *J. Org Chem.* **63** (1998) 7481
2. P. A. Yonova, G. M. Stoilkova, *J. Plant Growth Regul.* **23** (2004) 280
3. H. M. Abdel-Rahman, M. A. Morsy, *J. Enzyme Inhib. Med. Chem.* **22** (2007) 57
4. O. Adeoye, A. A. Ayandele, O. A. Odunola, *J. Agric. Biol. Sci.* **2** (2007) 4
5. J. D. Bloom, R. G. Dushin, K. J. Curran, F. Donahue, E. B. Norton, E. Terefenko, T. R. Jonas, A. A. Ross, B. Feld, S. A. Lang, M. Di-Grandi, *J. Bioorg. Med. Chem.* **14 (**2004) 3401
6. T. K. Venkatachalam, E. A. Sudbeck, C. Mao, F. M. Uckun, *Bioorg. Med. Chem.* **11** (2001) 523

7. Z. Shusheng, Z. Tianrong, C. Kun, X. Youfeng, Y. Bo, *Eur. J. Med. Chem.* **43** (2008) 2778
8. J. N. Dominguéz, C. León, J. Rodrigues, N. Gamboa de Dominguez, J. Gut, P. J. Rosenthal, *J. Med. Chem.* **48 (**2005) 3654
9. J. E. Audia, D. A. Evrard, G. R. Murdoch, J. J. Droste, J. S. Nissen, K. W. Schenck, P. Fludzinski, V. L. Lucaites, D. L. Nelson, M. L. Cohen, *J. Med. Chem.* **39** (1996) 2773
10. H. Pluempe, W. Pulls, *CA* **74** (1971) 1251154n
11. D. W. Ludovici, M. J. Kukla, P. G. Grous, S. Krishnan, K. Andries, M.-P. de Béthune, H. Azijn, R. Pauwels, E. De Clercq, E. Arnold, P. A. J. Janssen, *Bioorg. Med. Chem. Lett.* **11** (2001) 2225
12. W. Paulus, H. Chienpflug, H. Genth, *CA* **84** (1976) 121876h
13. C. J. Martin, H. R. Meen, H. M. Lewis, *CA* **84** (1976) 46003
14. J. Smith, L. J. Liras, S. E. Schneider, E. V. Anslys, *J. Org. Chem.* **61** (1996) 8811
15. L. D. Longo, *Environ. Health Perspect.* **74** (1987) 93
16. A. Liav, S. K. Angala, P. J. Brennan, M. Jackson, *Bioorg Med Chem Lett.* **8** (2008) 2649
17. X. J. Zou, G. Y. Jin, Z. Yang, *Chem. J. Chin. Univ.* **23** (2002) 403
18. H. Nakano, H. Haroda, T. Funaoka, K. Akashi, *CA* **78** (1973) 43086
19. W. L. F. Armarego, D. D. Perrin, *Purification of Laboratory Chemicals*, 4th ed., Butterworth, Heinemann, Oxford, UK, 1997
20. G. V. Gooding, T. T. Hebert, *Phytopathology* **57** (1967) 1285
21. B. A. Song, H. P. Zhang, H. Wang, S. Yang, L. H. Jin, D. Y. Hu, L. L. Pang, W. Xue, *J. Agric. Food Chem.* **53** (2005) 7886
22. N. Cotelle, J. L. Bemier, J. P. Catteau, J. Pommery, J. C. Wallet, E. M. Wallet, *Free radic. Biol. Med*. **20** (1996) 35
23. M. V. Ramirez-Mares, E. G. De Mejia, *Food Chem. Toxicol*. **41** (2003) 1527
24. W. H. Habig, M. J. Pabst, W. B. Jakoby, *J. Biol. Chem.* **249** (1974) 7130
25. G. L. Ellman, *Arch. Biochem. Biophys.* **82** (1959) 70.

Journal of the Serbian Chemical Society
JSCS@tmf.bg.ac.rs • www.shd.org.rs/JSCS
J. Serb. Chem. Soc. 79 (3) S37–S40 (2014) *Supplementary material*

SUPPLEMENTARY MATERIAL TO

Synthesis and biological evaluation of novel urea and thiourea derivatives of valaciclovir

VENKATA RAMANA KATLA[1], RASHEED SYED[1], MADHAVA GOLLA[1], ADAM SHAIK[2] and NAGA RAJU CHAMARTHI[1*]

[1]*Department of Chemistry, Sri Venkateswara University, Tirupati - 517 502, India and* [2]*Department of Biochemistry, Sree Vidyaniketan P.G College, Tirupati - 517 502, India*

J. Serb. Chem. Soc. 79 (3) (2014) 283–289

ANALYTIC AND SPECTRAL DATA FOR COMPOUNDS **3a**–**j**

*2-[(2-Amino-6-oxo-6,9-dihydro-3*H*-purin-9-yl)methoxy]ethyl 3-methyl-2-{[(phenylamino)thioxomethyl]amino}butanoate (**3a**)*. Yield: 82 %; m.p. 144–146 °C; Anal. Calcd. for $C_{20}H_{25}N_7O_4S$: C, 52.27; H, 5.48; N, 21.34 %. Found: C, 52.29, H, 5.42; N, 21.25 %; IR (KBr, cm^{-1}): 3412 (N–H), 3138 (NH_2), 1183 (C=S), 724 (C–S); ^{1}H-NMR (500 MHz, DMSO-d_6, δ / ppm): 10.8 (1H, *s*, N–H), 8.21 (1H, *s*, Ar-H), 7.86 (2H, *s*, NH_2), 7.68–6.94 (5H, *m*, Ar-H), 5.24 (2H, *t*, *J* = = 7.6 Hz, CH_2), 5.18 (2H, *t*, *J* = 6.8 Hz, CH_2), 4.58 (2H, *s*, CH_2), 4.20 (1H, *s*, NH-Ar), 3.41 (1H, *s*, NH–C=S), 2.84 (1H, *d*, *J* = 5.2 Hz, H-16), 1.64–1.48 (1H, *m* (C**H**–$(CH_3)_2$), 1.24 (6H, *d*, *J* = 5.6 Hz (CH–(C**H**$_3)_2$); ^{13}C-NMR (125 MHz, DMSO-d_6, δ / ppm): 166.8 (C_{20} of C=S), 159.8 (C_{15} of C=O), 158.2 (C_4 of HN–C=O), 152.4 (C_6), 146.2, 142.4, 136.2, 128.2, 126.8, 126.4, 124.6, 126.2, 118.6, 67.4, 65.2 (C_{16}), 64.2, 61.2, 32.4, 19.4, 18.5; MS (*m*/*z*): 459 M^+.

*2-[(2-Amino-6-oxo-6,9-dihydro-3*H*-purin-9-yl)methoxy]ethyl 2-{[((4-fluorophenyl)amino)thioxomethyl]amino}-3-methylbutanoate (**3b**)*. Yield: 80 %; m.p. 150–152 °C; Anal. Calcd. for $C_{20}H_{24}N_7O_4S$: C, 50.31; H, 5.07; N, 20.53 %. Found: C, 50.25, H, 5.01; N, 20.48 %; IR (KBr, cm^{-1}): 3416 (N–H), 3118 (NH_2), 1188 (C=S), 728 (C–S); ^{1}H-NMR (500 MHz, DMSO-d_6, δ / ppm): 11.2 (1H, *s*, N–H), 8.12 (1H, *s*, Ar-H), 8.02 (2H, *s*, NH_2), 7.62–6.92 (4H, *m*, Ar-H), 5.12 (2H, *t*, *J* = 7.4 Hz, CH_2), 4.96 (2H, *t*, *J* = 7.4 Hz, CH_2), 4.32 (2H, *s*, CH_2), 4.16 (1H, *s*, NH-Ar), 3.21 (1H, *s*, NH–C=S), 2.04 (1H, *d*, *J* = 4.6 Hz, H-16), 1.92–1.82 (1H, *m* (C**H**–$(CH_3)_2$), 1.12 (6H, *d*, *J* = 5.2 Hz (CH–(C**H**$_3)_2$); ^{13}C-NMR (125 MHz, DMSO-d_6, δ / ppm): 168.2 (C_{20} of C=S), 159.2 (C_{15} of C=O), 156.2 (C_4 of HN–C=O), 153.8 (C_6), 144.2, 139.6, 135.4, 129.2, 128.6, 127.5, 127.2, 125.4, 116.4, 66.8, 65.7, 65.4 (C_{16}), 60.6, 33.6, 19.6, 19.2; MS (*m*/*z*): 477 M^+.

* Corresponding author. E-mail: rajuchamarthi10@gmail.com

*2-[(2-Amino-6-oxo-6,9-dihydro-3*H*-purin-9-yl)methoxy]ethyl {[((4-chlorophenyl)amino)thioxomethyl]amino}-3-methylbutanoate (**3c**)*. Yield: 79 %; m.p. 148–150 °C; Anal. Calcd. for $C_{20}H_{24}ClN_7O_4S$: C, 48.63; H, 4.90; N, 19.85 %. Found: C, 48.71, H, 4.83; N, 19.68 %; IR (KBr, cm^{-1}): 3422 (N–H), 3130 (NH_2), 1194 (C=S), 732 (C–S); ^{1}H-NMR (500 MHz DMSO-d_6, δ / ppm): 11.6 (1H, *s*, N–H), 8.32 (1H, *s*, Ar-H), 7.64–6.82 (4H, *m*, Ar-H), 7.54 (2H, *s*, NH_2), 5.24 (2H, *t*, *J* = 7.6 Hz, CH_2), 4.82 (2H, *t*, *J* = 6.9 Hz, CH_2), 4.32 (1H, *s*, NH-Ar), 4.28 (2H, *s*, CH_2), 4.2 (1H, *s*, NH–C=S), 2.42 (1H, *d*, *J* = 4.6 Hz, H-16), 1.42–1.34 (1H, *m* (C**H**–$(CH_3)_2$), 1.22 (6H, *d*, *J* = 5.4 Hz (CH–(C**H**$_3)_2$); ^{13}C-NMR (125 MHz DMSO-d_6, δ / ppm): 174.6 (C_{20} of C=S), 171.6 (C_{15} of C=O), 154.2 (C_6), 152.5 (C_4 of HN–C=O), 145.6, 141.5, 135.4, 129.2, 128.6, 127.5, 127.2, 125.4, 118.2, 69.2, 67.2 (C_{16}), 66.4, 61.5, 31.4, 19.7, 19.4; MS (*m*/*z*): 493 M^+.

*2-[(2-Amino-6-oxo-6,9-dihydro-3*H*-purin-9-yl)methoxy]ethyl 3-methyl-2--{[((4-nitrophenyl)amino)thioxomethyl]amino}butanoate (**3d**)*. Yield: 78 %; m.p. 128–130 °C; Anal. Calcd. for $C_{20}H_{24}N_8O_6S$: C, 47.61; H, 4.79; N, 22.21 %. Found: C, 47.56, H, 4.75; N, 22.17 %; IR (KBr, cm^{-1}): 3428 (N–H), 3116 (NH_2), 1206 (C=S), 738 (C–S); ^{1}H-NMR (500 MHz, DMSO-d_6, δ / ppm): 11.4 (1H, *s*, N–H), 8.42 (1H, *s*, Ar-H), 7.72 (2H, *s*, NH_2), 7.52–6.88 (4H, *m*, Ar-H), 5.18 (2H, *t*, *J* = 7.1 Hz, CH_2), 4.64 (2H, *t*, *J* = 6.4 Hz, CH_2), 4.62 (1H, *s*, NH–C=S), 4.56 (1H, *s*, NH-Ar), 4.32 (2H, *s*, CH_2), 2.26 (1H, *d*, *J* = 4.6 Hz, H-16), 1.42–1.26 (1H, *m* (C**H**–$(CH_3)_2$), 1.08 (6H, *d*, *J* = 5.2 Hz (CH–(C**H**$_3)_2$); ^{13}C-NMR (125 MHz DMSO-d_6, δ / ppm): 182.4 (C_{20} of C=S), 172.4 (C_{15} of C=O), 155.4 (C_6), 151.6 (C_4 of HN–C=O), 146.2, 140.4, 136.2, 128.7, 128.4, 128.2, 128.0, 127.4, 117.4, 68.6, 67.2, 66.2 (C_{16}), 63.7, 30.6, 19.5, 19.2; MS (*m*/z): 504 M^+.

*2-[(2-Amino-6-oxo-6,9-dihydro-3*H*-purin-9-yl)methoxy]ethyl 2-{[((3-bromophenyl)amino)thioxomethyl]amino}-3-methylbutanoate (**3e**)*. Yield: 76 %; m.p. 110–112 °C; Anal. Calcd. for $C_{20}H_{24}BrN_7O_4S$: C, 44.61; H, 4.49; N, 18.21 %. Found: C, 44.51; H, 4.36; N, 18.32 %; IR (KBr, cm^{-1}): 3426 (N–H), 3112 (NH_2), 1198 (C=S), 720 (C–S); ^{1}H-NMR (500 MHz DMSO-d_6, δ / ppm): 10.9 (1H, *s*, N–H), 8.28 (1H, *s*, Ar-H), 7.84 (2H, *s*, NH_2), 7.32–6.94 (4H, *m*, Ar-H), 5.24 (2H, *t*, *J* = 7.6 Hz, CH_2), 4.82 (1H, *s*, NH–C=S), 4.46 (2H, *t*, *J* = 6.4Hz, CH_2), 4.32 (1H, *s*, NH-Ar), 4.12 (2H, *s*, CH_2), 2.12 (1H, *d*, *J* =5.8 Hz, H-16), 1.42–1.24 (1H, *m* (C**H**–$(CH_3)_2$), 1.14 (6H, *d*, *J* = 6.4 Hz, (CH–(C**H**$_3)_2$); ^{13}C-NMR (125 MHz DMSO-d_6, δ / ppm): 172.8 (C_{20} of C=S), 171.6 (C_{15} of C=O), 157.2 (C_6), 152.4 (C_4 of HN–C=O), 147.6, 138.6, 137.4, 127.6, 127.2, 126.8, 126.4, 124.6, 116.8, 69.2, 68.4, 65.4 (C_{16}), 65.2, 31.2, 18.9, 18.6; MS (*m*/*z*): 537 M^+.

*2-[(2-Amino-6-oxo-6,9-dihydro-3*H*-purin-9-yl)methoxy]ethyl 2-[3-(4-bromophenyl)ureido]-3-methylbutanoate (**3f**)*. Yield: 77 %; m.p. 118–120 °C; Anal. Calcd. for $C_{20}H_{24}BrN_7O_5$: C, 45.99; H, 4.63; N, 15.30 %. Found: C, 45.86; H, 4.52; N, 15.26 %; IR (KBr, cm^{-1}): 3432 (N–H), 3109 (NH_2), 1656 (C=O), 1070 (C–O); ^{1}H-NMR (500 MHz, DMSO-d_6, δ / ppm): 11.2 (1H, *s*, N–H), 8.36 (1H, *s*,

Ar-H), 7.62 (2H, *s*, NH_2), 7.46–6.87 (4H, *m*, Ar-H), 5.12 (2H, *t*, *J* = 7.1 Hz, CH_2), 4.64 (1H, *s*, NH–C=S), 4.32 (2H, *t*, *J* = 6.2 Hz, CH_2), 4.26 (1H, *s*, NH-Ar), 4.06 (2H, *s*, CH_2), 2.24 (1H, *d*, *J* = 6.4 Hz, H-16), 1.36–1.24 (1H, *m* (C**H**––$(CH_3)_2$), 1.22 (6H, *d*, *J* = 4.6 Hz (CH–(C**H**$_3)_2$); ^{13}C-NMR (125 MHz, DMSO--d_6, δ / ppm): 169.2 (C_{15} of C=O), 158.4 (C_6), 151.6 (C_4 of HN–C=O), 148.4 (C_{20} of C=O), 145.8, 137.5, 136.2, 128.2, 127.9, 127.6, 126.8, 123.8, 118.2, 69.5, 68.4, 66.5 (C_{16}), 64.8, 30.6, 19.4, 18.8; MS (*m*/*z*): 521 M^+.

*2-[(2-Amino-6-oxo-6,9-dihydro-3*H*-purin-9-yl)methoxy]ethyl 2-[3-(4-fluorophenyl)ureido]-3-methylbutanoate (**3g**)*. Yield: 81 %; m.p. 106–108 °C; Anal. Calcd. for $C_{20}H_{24}FN_7O_5$: C, 52.06; H, 5.24; N, 21.25 %. Found: C, 52.01, H, 5.17; N, 21.18 %; IR (KBr, cm^{-1}): 3440 (N–H), 3152 (NH_2), 1648 (C=O), 1035 (C–O); ^{1}H-NMR (500 MHz, DMSO-d_6, δ / ppm): 12.4 (1H, *s*, N–H), 8.02 (1H, *s*, Ar-H), 7.92–6.74 (4H, *m*, Ar-H), 7.76 (2H, *s*, NH_2), 5.64 (2H, *t*, *J* = 7.2 Hz, CH_2), 4.86 (1H, *s*, NH–C=S), 4.36 (1H, *s*, NH-Ar),) 4.28 (2H, *t*, *J* = 6.1 Hz, CH_2), 4.12 (2H, *s*, CH_2), 2.12 (1H, *d*, *J* = 5.6 Hz, H-16), 1.82–1.64 (1H, *m* (C**H**––$(CH_3)_2$), 1.38 (6H, *d*, *J* = 6.8 Hz (CH–(C**H**$_3)_2$); ^{13}C-NMR (125 MHz, DMSO--d_6, δ / ppm): 170.4 (C_{15} of C=O), 157.2 (C_6), 153.4 (C4 of HN–C=O), 152.6 (C_{20} of C=O), 146.4, 139.8, 139.4, 127.2, 126.6, 125.8, 125.2, 124.6, 117.5, 68.2, 67.6, 67.2, 65.2, (C_{16}), 31.6, 19.8, 19.4; MS (*m*/*z*) : 461 M^+.

*2-[(2-Amino-6-oxo-6,9-dihydro-3*H*-purin-9-yl)methoxy]ethyl 2-[3-(3,4-dichlorophenyl)ureido]-3-methylbutanoate (**3h**)*. Yield: 75 %; m.p. 102–104 °C; Anal. Calcd. for $C_{20}H_{23}Cl_2N_7O_5$: C, 46.89; H, 4.52; N, 19.14 %. Found: C, 46.80, H, 4.46; N, 19.10 %; IR (KBr, cm^{-1}): 3438 (N–H), 3112 (NH_2), 1652 (C=O), 1074 (C–O); ^{1}H-NMR (500 MHz, DMSO-d_6, δ / ppm): 12.2 (1H, *s*, N–H), 8.12 (1H, *s*, Ar-H), 7.94–6.84 (3H, *m*, Ar-H), 7.62 (2H, *s*, NH_2), 5.52 (2H, *t*, *J* = = 7.8 Hz, CH_2), 4.74 (1H, *s*, NH–C=S), 4.32 (2H, *t*, *J* = 6.3 Hz, CH_2), 4.28 (1H, *s*, NH-Ar), 4.14 (2H, *s*, CH_2), 2.22 (1H, *d*, *J* = 5.6 Hz, H-16), 1.86–1.64 (1H, *m* (C**H**–$(CH_3)_2$), 1.26 (6H, *d*, *J* = 6.2 Hz (CH–(C**H**$_3)_2$); ^{13}C-NMR (125 MHz, DMSO-d_6, δ / ppm): 171.5 (C_{15} of C=O), 158.4 (C_6), 155.6 (C_4 of C=O), 150.8 (C_{20} of C=O), 148.2, 138.2, 136.8, 127.4, 126.8, 126.6, 126.2, 125.8, 118.2, 69.2, 67.4, 66.4 (C_{16}), 62.6, 19.6, 32.4, 19.2; MS (*m*/*z*): 512 M^+.

*2-[(2-Amino-6-oxo-6,9-dihydro-3*H*-purin-9-yl)methoxy]ethyl 2-[3-(3-chloro-4-fluorophenyl)ureido]-3-methylbutanoate (**3i**)*. Yield: 72 %; m.p. 100–102 °C; Anal. Calcd. for $C_{20}H_{23}ClFN_7O_5$: C, 48.44; H, 4.67; N, 19.77 %. Found: C, 48.39, H, 4.58; N, 19.72 %; IR (KBr, cm^{-1}): 3442 (N–H), 3132 (NH_2), 1668 (C=O), 1035 (C–O); ^{1}H-NMR (500 MHz, DMSO-d_6, δ / ppm): 11.9 (1H, *s*, N–H), 8.24 (1H, *s*, Ar-H), 7.86–6.92 (3H, *m*, Ar-H), 7.74 (2H, *s*, NH_2), 5.42 (2H, *t*, *J* = = 7.6 Hz, CH_2), 4.62 (1H, *s*, NH–C=S), 4.46 (2H, *t*, *J* = 6.4 Hz, CH_2), 4.16 (1H, *s*, NH-Ar), 4.24 (2H, *s*, CH_2), 2.34 (1H, *d*, *J* = 5.7 Hz, H-16), 1.91–1.74 (1H, *m* (C**H**–$(CH_3)_2$), 1.34 (6H, *d*, *J* = 5.2 Hz (CH–(C**H**$_3)_2$); ^{13}C-NMR (125 MHz, DMSO-d_6, δ / ppm): 172.4 (C_{15} of C=O), 159.6 (C_6), 156.2 (C_4 of HN–C=O),

152.6 (C_{20} of C=O), 149.5, 139.7, 139.2, 128.5, 127.7, 126.8, 126.2, 125.2, 119.4, 69.6, 68.2, 67.6 (C_{16}), 63.7, 31.8, 20.2, 19.8; MS (*m*/*z*): 496 M^+.

*2-[(2-Amino-6-oxo-6,9-dihydro-3*H*-purin-9-yl)methoxy]ethyl 2-{3-[4-chloro-3-(trifluoromethyl) phenyl]ureido}-3-methylbutanoate (**3j**)*. Yield: 74 %; m.p. 122–124 °C; Anal. Calcd. for $C_{21}H_{23}ClF_3N_7O_5$: C, 46.20; H, 4.25; N, 17.96 %. Found: C, 46.14, H, 4.18; N, 17.89 %; IR (KBr, cm^{-1}): 3448 (N–H), 3142 (NH_2), 1672 (C=O), 1053 (C–O); ^{1}H-NMR (500 MHz, DMSO-d_6, δ / ppm): 12.2 (1H, *s*, N–H), 8.22 (1H, *s*, Ar-H), 7.92–6.74 (3H, *m*, Ar-H), 7.58 (2H, *s*, NH_2), 5.32 (2H, *t*, *J* = 7.4 Hz, CH_2), 4.56 (1H, *s*, NH–C=S), 4.54 (2H, *t*, *J* = 6.4 Hz, CH_2), 4.36 (2H, *s*, CH_2), 4.28 (1H, *s*, NH-Ar), 2.28 (1H, *d*, *J* = 4.4 Hz, H-16), 1.84–1.62 (1H, *m* (C**H**–$(CH_3)_2$), 1.26 (6H, *d*, *J* = 6.6 Hz (CH–(C**H**$_3)_2$); ^{13}C-NMR (125 MHz, DMSO-d_6, δ / ppm): 171.6 (C_{15} of C=O), 157.6 (C_4 of HNC=O), 156.4 (C_6), 151.2 (C_{20} of C=O), 148.8, 140.8, 139.4, 128.2, 127.9, 126.5, 125.8, 124.8, 118.2, 68.6, 67.4, 66.4 (C_{16}), 62.6, 30.4, 19.8, 19.2; MS (*m*/*z*): 545 M^+.

Journal of the Serbian Chemical Society
JSCS-info@shd.org.rs • www.shd.org.rs/JSCS
J. Serb. Chem. Soc. *79* (3) 291–302 (2014)
JSCS–4584
UDC 542.9+546.562'141:
547.759.32:548.7:543.57
Original scientific paper

Transition metal complexes with thiosemicarbazide-based ligands. Part 60. Reactions of copper(II) bromide with pyridoxal *S*-methylisothiosemicarbazone (PLITSC). Crystal structure of $[Cu(PLITSC–H)H_2O]Br·H_2O$

VUKADIN M. LEOVAC[1*#], LJILJANA S. VOJINOVIĆ-JEŠIĆ[1#], SONJA A. IVKOVIĆ[2#], MARKO V. RODIĆ[1#], LJILJANA S. JOVANOVIĆ[1#], BERTA HOLLÓ[1#] and KATALIN MÉSZÁROS SZÉCSÉNYI[1#]

[1]*Faculty of Sciences, University of Novi Sad, Trg D. Obradovića 3, 21000 Novi Sad, Serbia and* [2]*Faculty of Environmental Protection, University EDUCONS, V. Putnika bb, 21208 Sremska Kamenica, Serbia*

(Received 22 June, revised 20 August 2013)

Abstract: The synthesis and structural characterization of a square-planar copper(II) complex with pyridoxal *S*-methylisothiosemicarbazone (PLITSC) of the formula $[Cu(PLITSC–H)H_2O]Br·H_2O$ (**1**) as the first Cu(II) complex with a monoanionic form of this ligand were described. Complex **1** together with two previously synthesized complexes $[Cu(PLITSC)Br_2]$ (**2**) and [Cu(PLITSC)-Br(MeOH)]Br (**3**) were characterized by elemental analysis, IR and electronic spectroscopy and by the methods of thermal analysis, conductometry and magnetochemistry.

Keywords: copper(II) complexes; pyridoxal *S*-methylisothiosemicarbazone; crystal structure; spectra; thermal analysis.

INTRODUCTION

Metal complexes with Schiff base derivatives of pyridoxal, which is one of the six natural forms of vitamin B6, due to their interesting chemical, structural and biological characteristics, have been the subject of many studies.[1] A special group of Schiff base derivatives of pyridoxal consists of its compounds with semi-, thiosemi- and isothiosemicarbazones, which were found to coordinate as ONO, ONS and ONN ligands, respectively.[2] The coordination chemistry of pyridoxal thiosemicarbazone (PLTSC) began in 1986 with the papers of Ferrari Belicchi *et al.*[3] and since then, this ligand has been used for the syntheses of many complexes, not only with transition, but also with some non-transition

* Corresponding author. E-mail: vukadin.leovac@dh.uns.ac.rs
# Serbian Chemical Society member.
doi: 10.2298/JSC130622084L

metals.[2–8] In contrast to this ligand, the coordination chemistry of the *S*-methyl derivative, *i.e.*, pyridoxal *S*-methylisothiosemicarbazone (PLITSC) commenced later with the papers of Leovac *et al.*,[2,9,10] which is the reason for the smaller number of described complexes [Cu(II),[2] Fe(III),[2,9,10] Co(III),[2,11] Ni(II),[12] V(V) and Mo(VI)[13]]. It was found that this tridentate ONN ligand can be coordinated as neutral, mono- and di-anionic species, which was proven by, among other methods, X-ray structural analysis of its complexes.[2,11–15] The structures of two square-pyramidal Cu(II) complexes with the neutral ligand, [Cu(PLITSC)-$NO_3(H_2O)$]NO_3[14] and [Cu(PLITSC)Br(MeOH)]Br,[15] and one square-planar complex with its di-anionic form [Cu(PLITSC–2H)NH_3]·H_2O·0.5 MeOH[2] have been already determined. In this paper, we describe the synthesis and structure of the first Cu(II) complex with a monoanionic PLITSC ligand [Cu(PLITSC–H)-H_2O]Br·H_2O (**1**) and its IR and UV–Vis spectral, thermal and some other physical characteristics are described. The same data are given for the previously synthesized copper(II) bromide complexes of PLITSC [Cu(PLITSC)Br_2] (**2**) and [Cu(PLITSC)Br(MeOH)]Br (**3**) and compared with the corresponding data of the newly synthesized compound **1**.

EXPERIMENTAL

Reagents

All employed chemicals were commercial products of analytical reagent grade, except for the ligand pyridoxal *S*-methylisothiosemicarbazone, which was prepared by the reaction of EtOH solutions of pyridoxal hydrochloride and *S*-methylisothiosemicarbazide hydroiodide, and subsequent neutralization with an aqueous solution of Na_2CO_3.[14]

Synthesis of the complexes

*[Cu(PLITSC–H)H_2O]Br·H_2O (**1**)*. A mixture of PLITSC (0.075 g, 0.25 mmol) and $CuBr_2$ (0.065 g, 0.3 mmol) was dissolved in a mixture of 8 cm^3 EtOH and 2 cm^3 H_2O with mild heating. After 4 days at room temperature, the brown single crystals, obtained from the brown–green solution were filtered off and washed with EtOH. Yield: 0.030 g.

The other two complexes were prepared according to procedures described in the literature,[15,16] *i.e.*, by the reactions of $CuBr_2$ and the ligand in ethanol (**2**) or methanol (**3**).

Analytical methods

Elemental analyses (C, H, N, S) of air-dried complexes were realized by standard micromethods.

The molar conductivities of freshly prepared EtOH and MeOH solutions of the complexes ($c = 1\times10^{-3}$ mol dm^{-3}) were measured on a Jenway 4010 conductivity meter.

The magnetic susceptibility measurements were conducted at room temperature on an MSB-MK1 magnetic susceptibility balance, Sherwood Scientific Ltd., Cambridge, UK.

The IR spectra were recorded as KBr pellets on a Thermo Nicolet NEXUS 670 FT-IR spectrophotometer in the range of 4000–400 cm^{-1}.

The electronic spectra of the complexes in DMF and MeOH solutions were recorded on a T80+ UV/Vis spectrometer PG Instruments Ltd. in the spectral range 270–1100 nm (DMF) and 210–1100 nm (MeOH).

Thermal data were obtained using a TA Instruments SDT-Q600 TGA/DSC instrument at 20 °C min^{-1} heating rate under a dynamic N_2 atmosphere (flow rate of 100 cm^3 min^{-1}) in alumina crucibles and with sample masses of ≈2 mg.

Single crystal X-ray crystallography

A single crystal of **1** was selected, glued on glass fiber and mounted on a Gemini S κ-geometry diffractometer (Agilent Technologies). A sealed tube with a Cu-anode was used as X-radiation source, which was monochromatized with a graphite crystal (CuKα, λ = 1.5418 Å). The diffraction pattern, obtained in the ω scan mode, was recorded with a Sapphire3 CCD area detector. Data collection, reduction, absorption correction (numerical, based on Gaussian integration over a multifaceted crystal model) and cell refinement were performed with CRYSALISPRO.[17] The structure was solved by a direct method using Sir92[18] and refined on F^2 with the SHELXL-2013 program[19] integrated in SHELXL[20] graphical user interface. Carbon bonded hydrogen atoms were introduced in idealized positions (CH, CH_2) and refined as riding with U_{iso} fixed as $1.2U_{eq}$ of the parent atoms, while in the case of CH_3 groups, the torsion angle was refined and Uiso was fixed as $1.5U_{eq}$ of the parent atoms. Positions of hydrogen atoms bonded to heteroatoms were taken from ΔF map and refined as riding, while their U_{iso} were refined, except for H4A where Uiso was fixed as 1.2 Ueq of the N4. A summary of the crystallographic data is given in Table I. Structural data were validated and analyzed with PLATON.[21] Figures were produced using ORTEP-3 and PLATON.[22]

TABLE I. Crystallographic data for [Cu(H_2O)(PLITSC–H)]Br·H_2O (**1**)

Crystal data		Data collection and refinement	
Molecular formula	$C_{10}H_{17}BrCuN_4O_4S$	Temperature, K	298(2)
Formula weight	432.79	Wavelength, Å	1.5418
Crystal system	Orthorhombic	θ range, °	3.6–72.2
Space group	$Pna2_1$	No. reflcns. measd.	3205
a / Å	6.9360 (3)	No. unique reflcns.	2010
b / Å	24.535 (1)	R_{int}	0.021
c / Å	8.9512 (4)	No. reflcns. with $I > 2\sigma I$	1838
V / Å^3	1523.3 (1)	No. restraints	1
Z	4	No. refined parameters	199
D_c / g cm^{-3}	1.887	Goodness-of-fit on F^2	1.05
μ (CuKα) / mm^{-1}	6.58	R and wR ($I > 2\sigma I$)	0.030 and 0.074
F(000)	868	R and wR (all data)	0.035 and 0.078
Crystal size, mm	0.40 × 0.20 × 0.03	$\Delta\rho_{max}$ and $\Delta\rho_{min}$, e Å^{-3}	0.40 and –0.33
Color / shape	Brown / plate		

RESULTS AND DISCUSSION

Synthesis and some physicochemical characteristics of the complexes

The newly synthesized complex Cu(PLITSC–H)H_2O]Br·H_2O (**1**) was obtained in the reaction of $CuBr_2$ and PLITSC (mole ratio 1:1) in warm 80 % ethanol. As can be seen from the formula, PLITSC is coordinated in its monoanionic form, which is obtained after deprotonation of the thioureido moiety. Since it was shown[15,16] that in the reaction of the same reactants but in the pure solvents (EtOH and MeOH), complexes **2** and **3** were formed containing the

neutral ligand form (Scheme 1), it could be concluded that the nature of the solvent has a striking influence on the form of the coordinated PLITSC. Namely, since the N–H bond weakens on coordination of the terminal nitrogen atom, the presence of water as a better proton acceptor than alcohol causes deprotonation of the ligand and the formation of **1**.

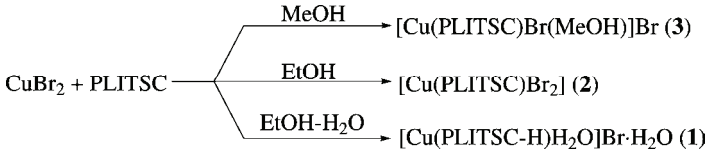

Scheme 1. Reactions of the syntheses of the complexes.

The type of the ligand deprotonation has a significant impact on the geometry of the complexes. Namely, the newly synthesized **1** with monodeprotonated PLITSC has a square-planar structure (*vide infra*). In contrast, in complex **3**, the square-pyramidal structure[15] is realized by a tridentate ONN coordination of the neutral PLITSC, one methanol molecule and one bromide ion. The change in the coordination geometry is a result of the increasing ligand field strength of PLITSC, caused by the deprotonation of the thioureido moiety, *i.e.* the increase in the donor ability of the coordinated terminal nitrogen atom. The structure of the desolvato complex **2** is most probably square pyramidal, realized by the tridentate coordination of PLITSC and the coordination of two bromido ligands. The value of the molar conductivity of ethanolic solution of **2** (Λ_M = 39 S cm^2 mol^{-1}) is characteristic for 1:1 electrolytes,[23] which refers to the coordination of only one bromide in solution with presumably [Cu(PLITSC)Br(EtOH)]$^+$ the most dominant species (Scheme 2). An almost identical value of Λ_M was found in an ethanolic solution of the similar [Cu(PLSC)Br$_2$] complex with the ONO tridentate pyridoxal semicarbazone (PLSC) ligand (Λ_M = 38 S cm^2 mol^{-1}). As it was shown by X-ray structure analysis that in [Cu(PLSC)Br$_2$], beside tridentate PLSC coordination, both bromides acted as co-ligands,[24] it might be supposed that two bromide ions are also coordinated in the crystals of complex **2**. Hence, it is reasonable to ascribe a penta-coordinated structure for complex **2**. It is noteworthy that [Cu(PLITSC)(H$_2$O)NO$_3$]NO$_3$ also has a square-pyramidal structure.[14] In contrast to the molar conductivity of an ethanolic solution of **2**, referring to a 1:1 electrolyte, the value of the molar conductivity of its methanolic solution (Λ_M = 141 S cm^2 mol^{-1}) corresponds to 2:1 electrolytes.[23] This means that due to stronger solvolysis effects of MeOH compared to EtOH, in methanolic solutions both bromido-ligands are replaced with two solvent molecules. The same holds for **3**, *i.e.*, the molar conductivity of its MeOH solution (Λ_M = 164 S cm^2 mol^{-1}) refers to the replacement of the coordinated bromide. This was not the case with its EtOH solution with a significantly lower

molar conductivity (Λ_M = 36 S cm^2 mol^{-1}). Hence, it could be concluded that **2** and **3** in the solutions of the cited alcohols behave in the same manner (Scheme 2). The molar conductivity of methanolic solution of **1** is in accordance with its coordination formula (Λ_M = 73 S cm^2 mol^{-1}).

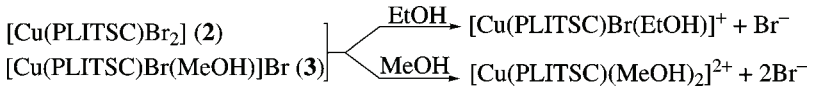

Scheme 2. Solvolysis reactions of complexes **2** and **3** in alcoholic solutions.

All three complexes are paramagnetic and the values of their effective magnetic moments are 1.78, 1.86 and 1.84 μ_B for **1**, **2** and **3,** respectively. The values are in the usual range for magnetically dilute Cu(II) compounds and only negligible spin–spin coupling, characteristic of dinuclear structures[25] might be present.

With the exception of **3**, which loses methanol, the other two complexes are stable at room temperature. All the complexes are well soluble in DMF, less soluble in MeOH and EtOH and insoluble in Et_2O.

Analytic and spectral data

[Cu(PLITSC–H)H$_2$O]Br·H$_2$O ***(1)***. Anal. Calcd. for $CuC_{10}H_{17}BrN_4O_4S$ (FW: 432.79): C, 27.73; H, 3.93; N, 12.94; S, 7.41 %. Found: C, 27.48; H, 3.90; N, 12.88; S, 7.49 %. IR (KBr, cm^{-1}): 3311, 3217, 2940, 2817, 1566, 1493, 1375, 1326, 1241, 1325, 1153, 1011, 905, 843, 718, 650; UV–Vis (DMF, λ / nm (log (ε / / M^{-1} cm^{-1}))): 320 (3.88), 366 (3.88), 390 (3.97), 424 (4.18), 444 (4.25), (MeOH, λ / nm (log (ε / M^{-1} cm^{-1}))): 243 (4.20), 265*sh* (4.18), 318 (3.74), 362*sh* (3.81), 380 (3.94), 413*sh* (415), 430 (4.23); molar conductivity (MeOH, Λ_M / S cm^2 mol^{-1}): 73; magnetic moment (μ_{eff} / μ_B): 1.78.

[Cu(PLITSC)Br$_2$] (2). Anal. Calcd. for $CuC_{10}H_{14}Br_2N_4O_2S$ (FW: 477.65): C, 25.14; H, 2.95; N, 11.73; S, 6.71 %. Found: C, 25.56; H, 3.02; N, 11.78; S, 6.39 %. IR (KBr, cm^{-1}): 3291, 3093, 2958, 2884, 2754, 1562, 1429, 1381, 1291, 1244, 1146, 1008, 907, 856, 782, 615. UV–Vis (DMF, λ / nm (log (ε / M^{-1} cm^{-1}))): 298 (4.00), 323 (3.97), 390*sh* (3.95), 414 (4.00), 442 (3.92), 642*sh* (2.15), (MeOH, λ / nm (log (ε / M^{-1} cm^{-1}))): 244 (4.30), 282 (3.90), 320 (3.91), 333*sh* (3.84), 388*sh* (3.95), 401 (3.99), 655 (1.90); molar conductivity (MeOH, Λ_M / S cm^2 mol^{-1}): 141 (EtOH, Λ_M / S cm^2 mol^{-1}): 39; magnetic moment (μ_{eff} / μ_B): 1.86.

[Cu(PLITSC)Br(MeOH)]Br (3). Anal. Calcd. for $CuC_{11}H_{18}Br_2N_4O_3S$ (FW: 509.70): C, 25.92; H, 3.56; N, 10.99; S, 6.29 %. Found: C, 25.86; H, 3.42; N, 10.78; S, 6.16 %. IR (KBr, cm^{-1}): 3323, 3239, 3112, 2945, 2816, 2718, 1566, 1546, 1437, 1387, 1326, 1307, 1242, 1158, 1036, 1000, 911, 853, 753, 576. UV–Vis (DMF, λ / nm (log (ε / M^{-1} cm^{-1}))): 298 (4.00), 325 (3.97), 392*sh* (3.94), 413 (3.99), 442 (3.83), 642*sh* (2.19), (MeOH, λ / nm (log (ε / M^{-1} cm^{-1}))): 244

(4.34), 285 (3.94), 320 (3.95), 334*sh* (3.88), 388*sh* (3.99), 401 (4.00), 655 (2.00); molar conductivity, (MeOH, Λ_M / S cm^2 mol^{-1}): 164, (EtOH, Λ_M / S cm^2 mol^{-1}): 36; magnetic moment (μ_{eff} / μ_B): 1.84.

IR and electronic spectra

In IR spectra, ν(OH) bands (H_2O, $–CH_2OH$, CH_3OH) and ν(NH) bands are observed at 3311 and 3217 (**1**), 3291 and 3093 (**2**) and 3323, 3239 and 3112 cm^{-1} (**3**). The well-defined ν(NH^+) band of the vibrations of the protonated pyridine nitrogen in the spectra of **1** and **2** are at 2817 and 2754 cm^{-1},[2,4] respectively, contrary to **3**, which in this range has one broad and unresolved band. The ν(C=N) band for all three complexes is located at ≈1565 cm^{-1} and in comparison to the same band of the free ligand (1655 cm^{-1}) is shifted to lower energy due to coordination of the azomethine nitrogen.[26,27] In contrast to this, as a result of the coordination of oxygen, a positive energy shift for the deprotonated phenolic hydroxyl, ν(C–O), was observed. In the spectrum of the ligand, the band is at 1255 cm^{-1} while it appears at 1326, 1291 and 1307 cm^{-1} in the spectra of the complexes **1**, **2** and **3**, respectively.[28,29]

In the available electronic spectral range, the spectra of the complexes display multiple, mainly unresolved bands of all kinds. Generally, the spectra of the complexes **2** and **3** are similar but different from those of **1**. The **s**imilarity of the spectra for **2** and **3** could be another proof of their similar structure.

In all the complexes, the strong band at the blue end of the spectra in MeOH (at about 244 nm) can be ascribed to π→π* pyridine ring absorptions which are, due to conjugation in the complexes, shifted by 25 nm to higher wavelengths compared to those of the ligand alone.[9,30] Other bands in the intraligand absorption region (λ < 360 nm) are poorly developed particularly in DMF due to partial overlapping of π→π* imine and n→π* of both imine and pyridine ring, which are also present in the spectra of the ligand.

All the complexes have very strong absorptions at about 400–450 nm, which belong to charge transfers and show complex solvation effects. The striking similarity of the spectra for **2** and **3** in each solvent, which is particularly obvious in this range, is a consequence of replacement of coordinated Br and MeOH by solvent molecules, thus forming the same complex structure (*vide infra*).

Additional characteristics of the CT bands at their long-wave sides is their complete overlapping with d–d transitions in the spectra for **1**, or partial merging for the other complexes, which therefore are seen as shoulders. In addition, very weak absorptions at wavelengths 850–900 nm cannot be precisely determined due to their overlapping with long-wave sides of comparatively stronger d–d bands. The recorded d–d transitions have negative solvatochromic effect because of better stabilization by solvation of the ground state molecule.

*Crystal structure of **1***

The molecular structure of the complex is shown in Fig. 1, whilst selected bond distances and angles are given in Table II. The asymmetric unit contains the complex cation, one water molecule and one bromide anion. The copper atom is situated in a square-planar environment made by ONN tridentate coordination of the organic ligand and one water molecule. Metal–ligand bond lengths are in the expected range (1.898 (4)–1.948 (5) Å), the M–O1 (phenoxide oxygen) being the shortest one and that of M–O3 (water oxygen) the longest one. The different metal–chelate ligand bond lengths are consistent with the electronic structure of PLITSC–H. Namely, due to the located negative charge, the phenoxide oxygen atom is the best electron donor, and as such builds the shortest bond. Due to ligand deprotonation (*vide infra*), the electron density is increased on the N1–C1–N2 fragment and is probably responsible for the slightly shorter Cu–N1 compared to the Cu–N3 bond.

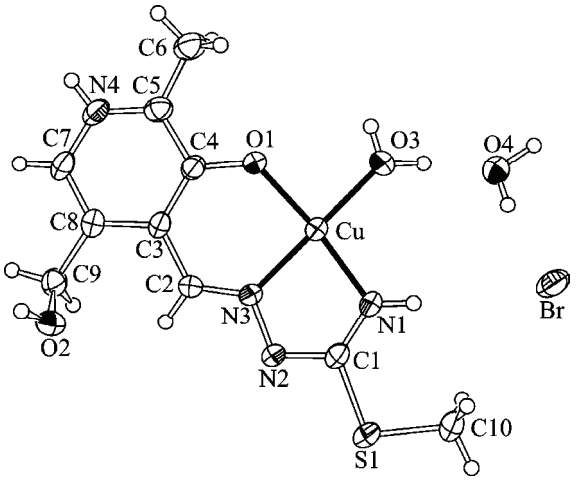

Fig. 1. Molecular structure of [Cu(PLITSC–H)(H_2O)]Br·H_2O (**1**).

TABLE II. Selected bond lengths and valence angles for **1**

Bond	Distance, Å	Bonds	Angle, °
Cu–O1	1.898 (4)	N1–Cu–N3	81.3 (2)
Cu–N1	1.926 (4)	O1–Cu–N3	92.4 (2)
Cu–N3	1.946 (5)	O3–Cu–N1	99.2 (2)
Cu–O3	1.948 (5)	O1–Cu–O3	87.5 (2)
C1–N1	1.307 (7)	O1–Cu–N1	171.8 (2)
C1–N2	1.337 (7)	O3–Cu–N3	175.7 (2)
N2–N3	1.370 (6)	N1–C1–N2	122.7 (5)
N3–C2	1.278 (7)	C1–N2–N3	122.7 (5)
C4–O1	1.301 (7)	N2–N3–C2	117.9 (5)
		C5–N4–C7	124.7 (5)

The chelate ligand is coordinated through phenoxide oxygen, azomethine and isothioamide nitrogen atoms in a monoanionic form, *i.e.*, in the same way as was found in $[VO_2(PLITSC–H)]\cdot 2H_2O$.[13] The tridentate coordination results in the formation of one five-membered (isothiosemicarbazide) and one six-membered (pyridoxylidene) planar metallocycles. The whole ligand molecule, besides the oxygen atom of the hydroxymethyl group, shows a high degree of planarity, which can be associated with its extended system of conjugated double bonds. It is interesting to note that the metallocycles and the pyridoxal ring lie virtually in the same plane, characterized by dihedral angles of 2.31(9)° between the five- and the six-membered metallocycles, and 2.9(1)° between the five-membered metallocycle and the pyridoxal ring. These values are close to those found in complex $[CuPLITSC(NO_3)(H_2O)]NO_3$,[14] but significantly lower than those in the complexes [Cu(PLITSC)Br(MeOH)]Br[15] (5.2 and 4.7°) and $[VO_2(PLITSC–H)]\cdot 2H_2O$ (12.0 and 7.8°),[13] in which the deformation of the square-pyramidal environment is more pronounced.

As in all the hitherto structurally characterized complexes,[12–15] PLITSC undergoes double spatial tautomerization, *i.e.*, migration of the phenolic hydrogen atom to pyridinic nitrogen atom, and migration of the hydrogen atom from the isothioamide nitrogen N1 to the neighboring nitrogen atom N2 of the hydrazine moiety. However, the nitrogen atom N2 under the given conditions is deprotonated, resulting in complex formation with the monoanionic form of PLITSC. This means that the pyridoxal moiety retains a zwitter-ionic form, which is confirmed by the value of the C6–N4–C8 angle (124.7 (5)°), which lies within the range characteristic for protonated pyridine rings.[4]

The fact that the structure of [Cu(PLITSC)Br(MeOH)]Br (**3**) is known[15] (CCDC-735806) enables the elucidation of the impact of the ligand deprotonation on the geometry of the formed complex, using comparative analysis. Namely, deprotonation of the hydrazine nitrogen atom leads to a slight shortening of the C1–N2 bond (1.337 (7) and 1.361 (3) Å in **1** and **3**, respectively) and elongation of C1–N1 bond (1.307 (7) and 1.273 (3) Å in **1** and **3,** respectively). This suggests that the electron pair is delocalized in the N2–C1–N1 fragment after the deprotonation, which is consistent with structural data reported for $[VO_2(PLITSC–H)]\cdot 2H_2O$.[13] Moreover, deprotonation leads to angular changes in the isothiosemicarbazide moiety, expressed through shrinkages of the N1–C1–N2 and C1–N2–N3 angles from 122.7 (5)° in **1** to 118.3 (2)° in **3** and from 122.7 (5)° in **1** to 115.2 (2)° in **3**, respectively.

Besides ionic interaction, association of the complex molecules in the solid state is determined by the presence of multiple hydrogen bond donors and acceptors. All the potential hydrogen donors, except for N1, are involved in the formation of intermolecular hydrogen bonds, with geometric parameters summarized in Table III. These secondary interactions link molecules in sheets extend-

TABLE III. Geometry of the intermolecular interactions for **1**. Symmetry codes: (i) *x*, *y*, *z*–1; (ii) *x*+½, –*y*+½, *z*+1; (iii) –*x*+½, *y*+½, *z*+½; (iv) *x*+½, –*y*+½, *z*; (v) *x*–½, –*y*+½, *z*; α = dihedral angle between planes I and J; β = angle between Cg(I)→Cg(J) vector and normal to plane I; γ = angle between Cg(I)→Cg(J) vector and normal to plane J; rings: (1) = Cu,N1,C1,N2,N3; (2) = Cu,O1,C4,C3,C2,N3; (3) = N4,C5,C4,C3,C8,C7

Hydrogen bonds				
D–H···A	*d*(D–H) / Å	*d*(H···A) / Å	*d*(D···A) / Å	∠(D–H···A) / °
O3–H3B···O2^{i}	0.81	1.92	2.708 (6)	164.1
O3–H3A···O4	0.96	1.79	2.745 (6)	174.6
O2–H2···O4^{ii}	0.93	1.89	2.728 (7)	149.7
N4–H4···Br^{iii}	0.84	2.40	3.233 (4)	173.3
O4–H4A···Br	0.79	2.52	3.196 (4)	143.1
O4–H4B···N2^{i}	0.98	1.89	2.797 (6)	153.4
π···π Stacking interactions				
Cg(I)···Cg(J)	*d*(Cg···Cg)	α / °	β / °	γ / °
Cg(1)···Cg(3)^{iv}	3.480 (3)	2.3 (2)	9.3	7.2
Cg(1)···Cg(3)^{v}	3.713 (3)	2.3 (2)	23.3	25.5
Cg(2)···Cg(2)^{v}	3.504 (3)	3.4 (1)	14.4	12.2

ing in the *bc* plane, as depicted in Fig. 2, which are in turn connected through O2–H2···O4^{ii} (symmetry code: (ii) *x*+½, –*y*+½, *z*+1) hydrogen bonds, as well as π···π stacking interactions (Table III), thus building a 3D supramolecular net-

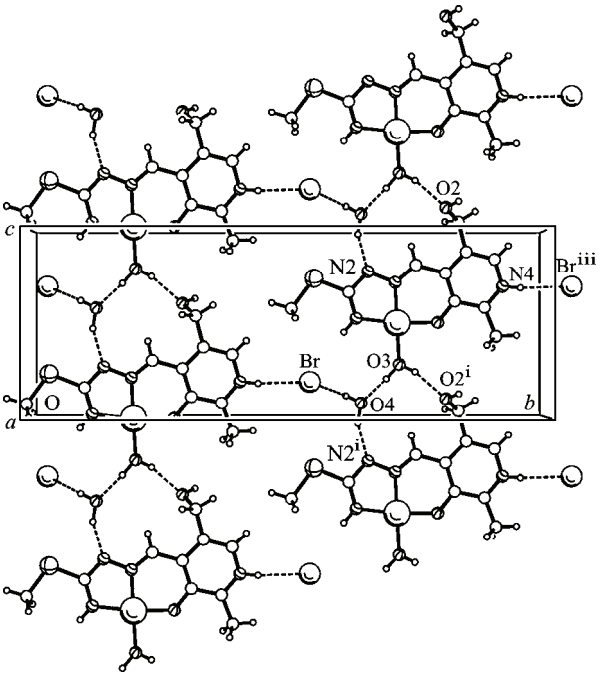

Fig. 2. Hydrogen bonded sheet in the *bc* plane of **1**. Symmetry codes are given in Table III.

work. Namely, zigzag puckered sheets are stacked in a way that the cations are lying parallel to each other at a *ca.* 3.4 Å distance. According to the literature,[31], mutual orientation of the stacked six-membered metallocycles corresponds to *cross* conformation, based on Cu–Cg(2)–Cg(2)^{v}–Cu^{v} torsion angle of 86.8 (8)° (Cg(2) is centroid of the six membered metallocycle; symmetry code: (v) *x*–½, –*y*+½, *z*). The five membered metallocycle is involved in asymmetrical π···π interactions through the pyridine rings of two neighboring sheets.

Thermal analysis

To present the decomposition patterns of compounds **1**–**3**, their derivative thermogravimetric (DTG) curves are shown in Fig. 3. The thermal decomposition of **1** started with the evaporation of both crystal and coordinated water with an onset temperature of 99 °C and a maximum decomposition rate at 168 °C. Before complete water removal, the decomposition of the organic ligand starts. The amount of water found to the minimum in the DTG curve (at 197 °C, 8.3 %) agrees with the calculated one (8.33 %). While the decomposition of **1** is obviously different, according to their similar composition, the decomposition of complexes **2** and **3** is very similar (see Fig. 3). Namely, the difference is in one coordinated methanol in compound **3**. During storage at room temperature, the methanol is almost completely lost, so the better-separated peaks in the DTG curve of **3** refer to the different structure of the starting compound. MeOH seems to be trapped in the crystals of the freshly prepared compound and at ≈150 °C, it evaporates in explosion-like steps. The decomposition in all three compounds is endothermic up to 250 °C, which at around 300 °C turns into an exothermic process. Under nitrogen, the decomposition is not complete at 700 °C.

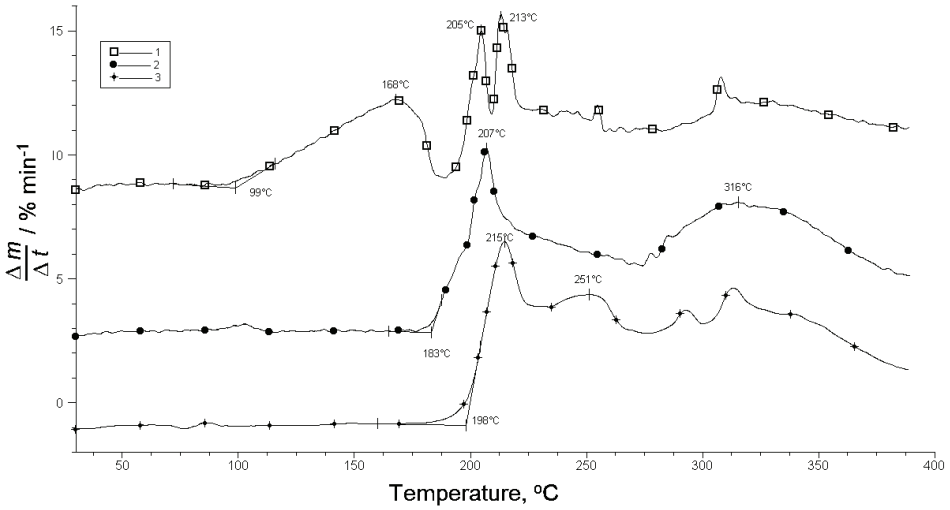

Fig. 3. DTG curves of complexes **1**–**3** in nitrogen atmosphere.

According to the thermal decomposition mechanism, it is very unlikely that the corresponding anhydrous compound of **1** could be prepared. Therefore, the thermal stability of **1** is rather low. Compounds **2** and **3** are practically stable up to about 180 °C, assuming that **3** had been left at room temperature until it had lost its MeOH. However, the thermal stability of complex **2** obtained by slow MeOH evaporation from **3**, due to different structure of the starting compound, is higher (see Fig. 3). Freshly prepared **3** is thermally stabile up to around 150 °C.

SUPPLEMENTARY MATERIAL

Crystallographic data reported for the complex [Cu(PLITSC–H)(H_2O)]Br·H_2O (**1**) have been deposited with CCDC, No. CCDC-942238. Copies of the data can be obtained free of charge *via* www.ccdc.cam.ac.uk.

Acknowledgements. This work was supported by the Provincial Secretariat for Science and Technological Development of Vojvodina and the Ministry of Education, Science and Technological Development of the Republic of Serbia (Grant No. 172014).

ИЗВОД

КОМПЛЕКСИ ПРЕЛАЗНИХ МЕТАЛА СА ЛИГАНДИМА НА БАЗИ ТИОСЕМИКАРБАЗИДА. ДЕО 60. РЕАКЦИЈЕ БАКАР(II)-БРОМИДА СА *S*-МЕТИЛИЗОТИОСЕМИКАРБАЗОНОМ ПИРИДОКСАЛА (PLITSC). КРИСТАЛНА СТРУКТУРА [Cu(PLITSC–H)H_2O]Br·H_2O

ВУКАДИН М. ЛЕОВАЦ[1], ЉИЉАНА С. ВОЈИНОВИЋ-ЈЕШИЋ[1], СОЊА А. ИВКОВИЋ[2], МАРКО В. РОДИЋ[1], ЉИЉАНА С. ЈОВАНОВИЋ[1], BERTA HOLLÓ[1] и KATALIN MÉSZÁROS SZÉCSÉNYI[1]

[1]*Природно–математички факултет, Универзитет у Новом Саду, Трг Д. Обрадовића 3, 21000 Нови Сад и* [2]*Факултет заштите животне средине, Универзитет EDUCONS, В. Путника бб, 21208 Сремска Каменица*

Синтетисан је и структурно окарактерисан квадратно-планарни комплекс бакра(II) са *S*-метилизотиосемикарбазоном пиридоксала (PLITSC) формуле [Cu(PLITSC–H)-H_2O]Br·H_2O (**1**), који представља први комплекс Cu(II) са моноанјонском формом наведеног лиганда. Комплекс **1** као и два раније синтетисана комплекса [Cu(PLITSC)Br_2] (**2**) и [Cu(PLITSC)Br(MeOH)]Br (**3**), окарактерисани су елементалном анализом, IR, UV–Vis спектрима, као и методама термичке анализе, кондуктометрије и магнетохемије.

(Примљено 22. јуна, ревидирано 20. августа 2013)

REFERENCES

1. J. S. Casas, M. D. Couce, J. Sordo, *Coord. Chem. Rev.* **256** (2012) 3036, and references therein
2. V. M. Leovac, V. S. Jevtović, Lj. S. Jovanović, G. A. Bogdanović, *J. Serb. Chem. Soc.* **70** (2005) 393, and references therein
3. M. Ferrari Belicchi, G. F. Gasparri, E. Leporati, C. Pelizzi, P. Tarasconi, G. Tosi, *J. Chem. Soc., Dalton Trans* (1986) 2455
4. S. Floquet, M. Carmen Munoz, R. Guillot, E. Riviere, G. Blain, J.-A. Real, M.-L. Boillot, *Inorg. Chim. Acta* **362** (2009) 56
5. E. W. Yemeli Tido, C. Faulmann, R. Roswanda, A. Meetsma, P. J. van Koningsbruggen, *Dalton Trans.* **39** (2010) 1643

6. V. Vrdoljak, J. Pisk, B. Prugovečki, D. Matković-Čalogović, *Inorg. Chim. Acta* **362** (2009) 4059
7. V. M. Leovac, Lj. S. Jovanović, V. Divjaković, A. Pevec, I. Leban, T. Armbruster, *Polyhedron* **26** (2007) 49
8. M. Belicchi Ferrari, F. Bisceglie, C. Casoli, S. Durot, I. Morgenstern-Badarau, G. Pelosi, E. Pilotti, S. Pinelli, P. Tarasconi, *J. Med. Chem.* **48** (2005) 1671
9. V. S. Jevtović, Lj. S. Jovanović, V. M. Leovac, L. J. Bjelica, *J. Serb. Chem. Soc.* **68** (2003) 929
10. Lj. S. Jovanović, V. S. Jevtović, V. M. Leovac, L. J. Bjelica, *J. Serb. Chem. Soc.***70** (2005) 187
11. V. Jevtović, D. Cvetković, D. Vidović, *J. Iran. Chem. Soc.* **8** (2011) 727
12. V. Jevtović, D. Vidović, *J. Chem. Crystallogr.* **40** (2010) 794
13. V. M. Leovac, V. Divjaković, M. D. Joksović, Lj. S. Jovanović, Lj. S. Vojinović-Ješić, V. I. Češljević, M. Mlinar, *J. Serb. Chem. Soc.* **75** (2010) 1063
14. V. M. Leovac, V. S. Jevtović, G. A. Bogdanović, *Acta Crystallogr., C* **58** (2002) 514
15. S. Ivković, V. Jevtović, *J. Eng. Process. Manag.* **2** (2010) 7
16. V. S. Jevtović, *Ph. D. Thesis*, Faculty of Science, University of Novi Sad, Novi Sad, 2002
17. CrysAlisPro Software system, version 1.171.35.19, Agilent Technologies UK Ltd., Oxford, 2011
18. A. Altomare, G. Cascarano, C. Giacovazzo, A. Gualardi, *J. Appl. Crystallogr.* **26** (1993) 343
19. G. M. Sheldrick, *Acta Crystallogr., A* **64** (2008) 112
20. C. B. Hübschle, G. M. Sheldrick, B. Dittrich, *J. Appl. Crystallogr.* **44** (2011) 1281
21. A. L. Spek, *Acta Crystallogr., D* **65** (2009) 148
22. L. J. Farrugia, *J. Appl. Crystallogr.* **30** (1997) 565
23. W. J. Geary, *Coord. Chem. Rev.* **7** (1971) 81
24. D. Poleti, Lj. Karanović, V. M. Leovac, V. S. Jevtović, *Acta Crystallogr., C* **59** (2003) 73
25. M. Belicchi Ferrari, G. G. Fava, C. Pelizzi, P. Tarasconi, G. Tosi, *J. Chem. Soc., Dalton Trans.* (1987) 227
26. E. W. Yemeli Tido, E. J. M. Vertelman, A. Meetsma, P. J. van Koningsbruggen, *Inorg. Chim. Acta* **360** (2007) 3896
27. M. R. Maurya, A. Kumar, M. Abid, A. Azam, *Inorg. Chim. Acta* **359** (2006) 2439
28. P. Kalaivani, R. Prabhakaran, E. Ramachandran, F. Dallemer, G. Paramaguru, R. Renganathan, P. Poornima, V. Vijaya Padma, K. Natarajan, *Dalton Trans.* **41** (2012) 2486
29. M. M. Lalović, V. M. Leovac, Lj. S. Vojinović-Ješić, M. V. Rodić, Lj. S. Jovanović, V. I. Češljević, *J. Serb. Chem. Soc.* **78** (2013) 1161
30. Lj. S. Jovanović, V. M. Leovac, unpublished results
31. D. N. Sredojević, Z. D. Tomić, S. D. Zarić, *Cryst. Growth Des.* **10** (2010) 3901.

Journal of the Serbian Chemical Society
JSCS-info@shd.org.rs • www.shd.org.rs/JSCS
J. Serb. Chem. Soc. *79* (3) 303–311 (2014) UDC 547.789.1+547.594.3:546.3–386:535.33
JSCS–4585 *Original scientific paper*

Heteroarylazo derivatives of cyclohexane-1,3-dione and their metal complexes

MUHAMMED BASHEER UMMATHUR[1]*, DAMODARAN KAMALAKSHY BABU[2] and KRISHNANNAIR KRISHNANKUTTY[3]

[1]PG Department of Chemistry, KAHM Unity Women's College, Manjeri, Kerala-676122, India, [2]Department of Chemistry, Zamorin's Guruvayurappan College, Calicut, Kerala-673014, India and [3]Department of Chemistry, University of Calicut, Kerala-673635, India

(Received 27 December 2012, revised 19 April 2013)

Abstract: The coupling of diazotized 2-aminothiazole and 2-aminobenzothiazole with cyclohexane-1,3-dione yielded a new type of tridentate ligand system (HL). Analytical, IR, ^{1}H-NMR, ^{13}C-NMR and mass spectral data indicate the existence of the compounds in the intramolecularly hydrogen bonded azo–enol tautomeric form. Monobasic tridentate coordination of the compounds in their [CuL(OAc)] and [ML_2] complexes [M = Ni(II) and Zn(II)] was established based on the analytical and spectral data. The Zn(II) chelates are diamagnetic while the Cu(II) and Ni(II) complexes showed a normal paramagnetic moment.

Keywords: heteroarylazo derivatives; 2-aminothiazole; 2-aminobenzothiazole; cyclohexane-1,3-dione; metal complexes; spectral data.

INTRODUCTION

Metallizable azo dyes containing one heterocyclic donor atom suitably located for the formation of annulated chelate complex were the subject of numerous studies,[1–3] the most common being those containing a hetero nitrogen atom in a position adjacent to the azo group.[4,5] They have wide application in analytical chemistry, metallurgy, the textile industry, optical data storage, photo switching and nonlinear optical materials,[6–10] and are also involved in many biological reactions.[11] In recent years, a significant number of tridentate azo compounds have been developed to improve the colouring properties, and to achieve more specificity and selectivity in chemical analysis.[12] Metal complexation alters the properties of a dye, both qualitatively and quantitatively.[13] However, the structural aspects of many of these dyestuffs and their metal complexes have not received as much attention as they deserve. In continuation of studies on

* Corresponding author. E-mail: mbummathur@gmail.com
doi: 10.2298/JSC121227042U

heteroarylazo derivatives of 1,3-diketones and their metal complexes,[14–19] the synthesis and characterization of two new heteroarylazo derivatives obtained by coupling the diazonium salts of 2-aminothiazole and 2-aminobenzothiazole with the active methylene group of cyclohexane-1,3-dione are reported herein. Typical metal complexes of these ligand systems were also synthesized and characterized.

EXPERIMENTAL

Methods, instruments and materials

The carbon, hydrogen and nitrogen contents were determined by microanalyses (Heraeus Elemental Analyzer from RSIC, Central Drug Research Institute, Lucknow, India, and Catalysis Division, Department of Chemistry, Indian Institute of Technology, Chennai, India) and the metal contents of the complexes by AAS (Perkin Elmer 2380 spectrometer). The electronic spectra of the compounds in methanol (10^{-4} mol L^{-1}) were recorded on a 1601 Shimadzu UV–Vis spectrophotometer, the IR spectra (KBr discs) on an 8101 Shimadzu FTIR spectrophotometer, the ^{1}H-NMR spectra ($CDCl_3$ or DMSO-d_6) on a Varian 300 NMR spectrometer and the mass spectra on a Jeol/SX-102 mass spectrometer (FAB using argon and *meta*-nitrobenzyl alcohol as the matrix). The molar conductance of the complexes were determined in DMF (≈10^{-3} mol L^{-1}) at room temperature (301±1 K). The magnetic susceptibilities were determined at room temperature on a Guoy-type magnetic balance, Sherwood Scientific Ltd., UK, at room temperature (301±1 K) using $Hg[Co(NCS)_4]$ as the standard.

Cyclohexane-1,3-dione, 2-aminothiazole, 2-aminobenzothiazole, methanol, urea and the metal acetates were of AR grade, purchased from Merck, Germany.

General procedure for the preparation of the 2-(thiazol-2-ylazo)cyclohexane-1,3-dione (HL^1) and 2-(benzothiazol-2-ylazo)cyclohexane-1,3-dione (HL^2) ligands

2-Aminothiazole/2-aminobenzothiazole was diazotized as reported previously.[20] After quenching the excess nitrous acid with urea, the diazonium salt solution (0.01 mol) was added dropwise to a well stirred ethanolic solution of cyclohexane-1,3-dione (0.01 mol, 20 mL) kept in an ice–salt bath and stirred well for ≈1 h. Sodium acetate (≈3 g) was added to adjust the pH to around 6. The precipitated product was filtered, washed with cold water and recrystallized from hot methanol.

Synthesis of the Ni(II), Cu(II) and Zn(II) complexes

A concentrated aqueous solution of metal(II) acetate, [$Ni(CH_3COO)_2{\cdot}4H_2O$, $Cu(CH_3COO)_2{\cdot}H_2O$ and $Zn(CH_3COO)_2{\cdot}2H_2O$] (0.01 mol, 15 mL) was added to a hot methanolic solution of the required ligand (0.02 mol, 20 mL). The mixture was refluxed on a water bath for ≈2 h. The precipitated complex after cooling to room temperature was filtered, washed with water, recrystallized from hot benzene and dried under vacuum over anhydrous $CaCl_2$.

RESULTS AND DISCUSSION

The yields, melting points and analytical data for the prepared ligands and complexes and the magnetic moments for the Ni and Cu complexes are given below.

HL^1. Yield: 60 %; m.p.: 151 °C; Anal. Calcd. for $C_9H_9N_3SO_2$: C, 48.43; H, 4.04; N, 18.83 %. Found: C, 48.20; H, 4.15; N, 18.68 %.

HL^2. Yield: 50 %; m.p.: 148 °C; Anal. Calcd. for $C_{13}H_{11}N_3SO_2$: C, 57.14; H, 4.03; N, 15.38 %. Found: C, 56.90; H, 4.10; N, 15.20 %.

Ni(L^1*)*$_2$. Yield: 60 %; m.p.: 250 °C; Anal. Calcd. for $C_{18}H_{16}N_6NiO_4S_2$: C, 42.97; H, 3.18; N, 16.71; Ni, 11.68 %. Found: C, 42.86; H, 3.12; N, 16.54; Ni, 11.70 %; Magnetic moment, μ_{eff}: 2.78 μ_B.

Ni(L^2*)*$_2$. Yield: 65 %; m.p.: >300 °C; Anal. Calcd. for $C_{26}H_{20}N_6NiO_4S_2$: C, 51.77; H, 3.32; N, 13.94; Ni, 9.74 %. Found: C, 51.56; H, 3.32; N, 14.01; Ni, 9.71 %; Magnetic moment, μ_{eff}: 2.74 μ_B.

Cu(L^1*)(OAc)*. Yield: 70 %; m.p.: 260 °C; Anal. Calcd. for $C_{12}H_{13}CuN_3O_4S$: C, 40.16; H, 3.63; N, 11.71; Cu, 17.72 %. Found: C, 40.08; H, 3.53; N, 11.65; Cu 17.50 %; Magnetic moment, μ_{eff}: 1.75 μ_B.

Cu(L^2*)(OAc)*. Yield: 75 %; m.p.: >300 °C; Anal. Calcd. for $C_{16}H_{15}CuN_3O_4S$: C, 47.00; H, 3.67; N, 10.28; Cu, 15.55 %. Found: C, 46.88; H, 3.61; N, 10.44; Cu 15.35 %; Magnetic moment, μ_{eff}: 1.74 μ_B.

Zn(L^1*)*$_2$. Yield: 70 %; m.p.: 270 °C; Anal. Calcd. for $C_{18}H_{16}N_6O_4S_2Zn$: C, 42.40; H, 3.14; N, 16.49; Zn, 12.84 %; Found: C, 42.32; H, 3.20; N, 16.40; Zn, 13.05 %.

Zn(L^2*)*$_2$. Yield: 60 %; m.p.: >300 °C; Anal. Calcd. for $C_{26}H_{20}N_6O_4S_2Zn$: C, 51.20; H, 3.28; N, 13.78; Zn, 10.73 %. Found: C, 51.14; H, 3.22; N, 13.72; Zn 10.78 %.

The observed analytical data of the hetero-arylazo derivatives (HL^1 and HL^2) indicate that the diazo-coupling reaction had occurred in a 1:1 ratio. The compounds are crystalline in nature and soluble in common organic solvents. They formed stable complexes with Ni(II), Cu(II) and Zn(II) ions. The analytical data together with the non-electrolytic nature in DMF (specific conductance <10 S cm^{-1} in 10^{-3} M solution) suggest [ML_2] stoichiometry of the complexes, except for the Cu(II) complexes that have [CuL(OAc)] stoichiometry. The Zn(II) chelates are diamagnetic while the Ni(II) and Cu(II) complexes showed a normal paramagnetic moment. The observed IR, ^{1}H-NMR, ^{13}C-NMR and mass spectral data are in conformity with Fig. 1 of the hetero-arylazo derivatives and Fig. 2 of the complexes. The Cu(II) complexes conform to Fig. 3.

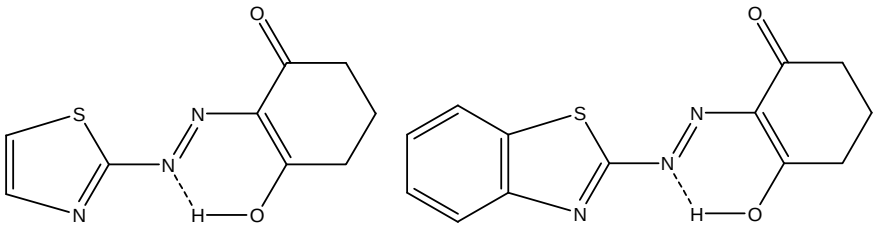

Fig. 1. Structural formulae of the a) HL^1 and b) HL^2 ligands.

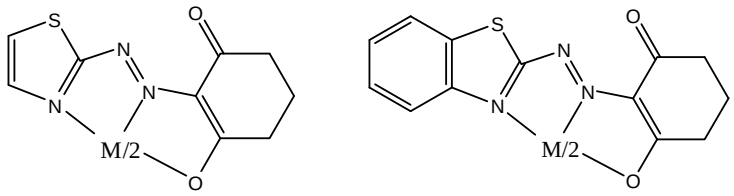

Fig. 2. Structural formulae of the Ni(II) and Zn(II) complexes; a) $[M(L^1)_2]$ and b) $[M(L^2)_2]$; M = Ni(II) or Zn(II).

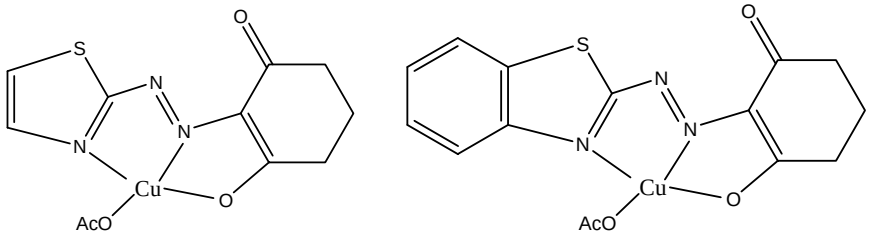

Fig. 3. Structural formulae of the a) $[Cu(L^1)(OAc)]$ and b) $[Cu(L^2)(OAc)]$ complexes.

IR spectra

The IR spectra of HL^1 and HL^2 show a strong band at ≈1720 cm^{-1} and a medium intensity band at ≈1610 cm^{-1}, assignable to the stretching of free carbonyl and ring C=N functions, respectively.[19,21] The two medium intensity bands observed at ≈1280 and 1480 cm^{-1} are due to C–O–H in-plane bending and N=N stretching, respectively.[16,21]. The medium intensity band present at ≈1460 cm^{-1} is assignable to CH_2 scissoring vibrations.[22] The broad band ranging from 3200 to 3500 cm^{-1} is due to strong O–H···N hydrogen bonding.[21] Thus, the IR spectra support the intramolecularly hydrogen bonded azo–enol tautomeric form of the compounds as in Fig. 1.

In the IR spectra of all the metal complexes, the free ligand bands at 1280 and 3200–3500 cm^{-1} were absent, indicating the replacement of enol protons by metal ions during complexation.[23,24] The free carbonyl band of the ligands is only marginally shifted in the spectra of the complexes, indicating the non-involvement of the carbonyl groups in the coordination. In the spectra, The band at ≈1480 cm^{-1} due to ν(N=N) and the band due to ring ν(C=N) at 1610 cm^{-1} of the free ligands were shifted appreciably to lower wave numbers,[15] indicating the involvement of these groups in complexation, as shown in Figs. 2 and 3. The IR spectra of the Cu(II) complexes showed a comparatively strong band at ≈1625 cm^{-1} and a medium intensity band at ≈1310 cm^{-1}. The energy separation between $\nu_{asym(COO-)}$ and $\nu_{sym(COO-)}$ was >144 cm^{-1}, which confirms the monodentate nature of the acetate ion,[25,26] since in the event of bidentate coordination,

the energy separation was reported[27] to be <144 cm^{-1}. The presence of new medium intensity bands at ≈420 and 540 cm^{-1}, assignable to ν(M–O) and ν(M–N) in the spectra of all the complexes[24,28,29] also support the structures shown in Figs. 2 and 3. Important bands that appeared in the spectra are given in Table I.

TABLE I. Characteristic IR stretching bands (cm^{-1}) of HL^1, HL^2 and their metal complexes; in the case of the copper complexes, the two additional bands given under C=O are due to the acetate groups

Compound	Free C=O	Cyclic C=N	N=N	M–N	M–O
HL^1	1715 *s*	1612 *m*	1472 *m*	–	–
$[Ni(L^1)_2]$	1712 *s*	1580 *m*	1442 *m*	538 *m*	426 *m*
$[Cu(L^1)(OAc)]$	1718 *s*, 1625 *s*, 1312 *m*	1582 *m*	1435 *m*	522 *m*	418 *m*
$[Zn(L^1)_2]$	1710 *s*	1593 *m*	1438 *m*	525 *m*	430 *m*
HL^2	1722 *s*	1612 *m*	1478 *m*	–	–
$[Ni(L^2)_2]$	1718 *s*	1588 *m*	1438 *m*	532 *m*	432 *m*
$[Cu(L^2)(OAc)]$	1720 *s*, 1622 *s*, 1310 *m*	1590 *m*	1445 *m*	528 *m*	422 *m*
$[Zn(L^2)_2]$	1720 *s*	1592 *m*	1448 *m*	530 *m*	420 *m*

NMR spectra

The ^{1}H-NMR spectra of HL^1 and HL^2 are characterized by the presence of a low-field, one-proton signal at δ ≈13.50 ppm, which is considerably lower than that reported for arylazo derivatives of 1,3-diketones existing in the hydrazone form.[15,30] Since azo–enol protons show a signal in the range δ 10–14 ppm, the signal at δ 13.5 ppm could be assigned to the intramolecularly hydrogen bonded enol proton.[31,32] The high resolution spectra show three types of alicyclic protons in the range δ 1.30–2.90 ppm, indicating the existence of three methylene groups in different electronic environments.[22,33] The hetero-aryl protons are observed in the range δ 7.30–8.40 ppm. The integrated intensities of the various signals agree well with the structure of the compounds presented in Fig. 1.

In the ^{1}H-NMR spectra of the diamagnetic Zn(II) complexes, the low field signal due to the intramolecularly hydrogen bonded OH protons disappeared, indicating their replacement by metal cations during complexation.[34] The integrated intensities of various signals agree well with the $[ML_2]$ stoichiometry of the complexes as presented in Fig. 2.

The ^{13}C-NMR spectra of HL^1 and HL^2 clearly indicate their existence in the azo–enol form. The carbonyl (C_1) and enolic (C_3) sp^2 carbon atoms appear as separate signals in the low field region, at δ ≈ 200 ppm. Separation of the C_4 and C_6 signals confirms the different electronic environment for these methylene carbons,[31] as shown in Fig. 1. The involvement of the enolate oxygen and the hetero nitrogen atom in bonding with the metal ion, as shown in Fig. 2, is evident from the positions of the various signals in the ^{13}C-NMR spectra of their Zn(II) complexes.

The assignments of the various observed signals are assembled in Table II.

TABLE II. ^{1}H-NMR and ^{13}C-NMR spectral data (δ / ppm) of HL^1, HL^2 and their Zn(II) complexes; *s* = singlet, *d* = doublet ($J \approx 3.7$ Hz), *t* = triplet ($J \approx 6.9$ Hz), *m* = multiplet

Compound	^{1}H-NMR			^{13}C-NMR				
	OH	Heteroaryl	Methylenic	C=O	C–O	CH_2	C–N	Heteroaryl
HL^1	13.52	7.50 (1H, *d*)	1.30 (2H, *m*)	192.94	198.24	18.21	166.31	140.87
	(1H, *s*)	7.90 (1H, *d*)	1.90 (2H, *t*)			39.24		132.34
			2.80 (2H, *t*)			39.39		116.12
$[Zn(L^1)_2]$	–	7.30 (2H, *d*)	1.40 (4H, *m*)	192.63	188.93	19.43	142.32	137.09
		7.80 (2H, *d*)	1.80 (4H, *t*)			36.55		129.37
			2.90 (4H, *t*)			39.75		119.33
HL^2	13.46	7.50–8.30	1.50 (2H, *m*)	192.59	197.34	17.92	151.21	133.07
	(1H, *s*)	(4H, *m*)	1.90 (2H, *t*)			39.17		132.51
			2.90 (2H, *t*)			39.37		126.67
								125.04
								122.31
								121.70
$[Zn(L^2)_2]$	–	7.60–8.40	1.40 (4H, *m*)	192.47	184.34	17.73	129.23	134.17
		(8H, *m*)	1.90 (4H, *t*)			38.12		132.34
			2.90 (4H, *t*)			39.68		126.22
								124.14
								122.00,
								121.61

Mass spectra

The formulation of the compounds as in Fig. 1 is clearly supported from the presence of an intense molecular ion peak in the mass spectra. The presence of peaks due to the elimination of N_2 from the molecular ion, characteristic of tautomers,[31,35,36] in the spectra support the azo structure of the compounds. Fragments due to the elimination of CH_2=CHCHO, heteroaryl groups, *etc*. are typical of the spectra.

The FAB mass spectra of the Cu(II) and Ni(II) complexes showed molecular ion peaks corresponding to [CuL(OAc)] and [NiL_2] stoichiometry. Peaks correspond to $[ML]^+$, L^+ and fragments of L^+ are also present in the spectra. The spectra of the Cu(II) complexes also showed peaks due to $[P - CH_3COO]^+$ and a number of fragments containing copper in the 3:1 natural abundance of ^{63}Cu and ^{65}Cu isotopes. The important mass spectral fragments and their assignments are assembled in Table III.

Electronic spectral and magnetic measurements data

The UV spectra of HL^1 and HL^2 showed two broad bands with maxima at ≈380 and ≈260 nm due to various n→π* and π→π* transitions. These absorption maxima shifted appreciably to low wave numbers in the spectra of the com-

plexes. The Cu(II) complexes showed a broad band centred at ≈660 nm. This, together with the measured μ_{eff} value (≈1.75 μ_B) suggests their square-planar geometry.[15,37] The Ni(II) chelates are paramagnetic (μ_{eff} value ≈2.80 μ_B) and show three well-separated absorption bands in the spectra at λ_{max} ≈925, ≈750 and ≈420 nm corresponding to the transitions $^3A_{2g}\rightarrow{}^3T_{2g}$, $^3A_{2g}\rightarrow{}^3T_{1g}(F)$ and $^3A_{2g}\rightarrow{}^3T_{1g}(P)$, respectively. Thus, the metal ion is in an octahedral environment.

TABLE III. Mass spectral data of HL^1, HL^2 and their Ni(II) and Cu(II) complexes

Ligands			Ni(II) complexes			Cu(II) complexes		
Fragment	*m*/*z*		Fragment	*m*/*z*		Fragment	*m*/*z*	
	HL^1	HL^2		$Ni(L^1)_2$	$Ni(L^2)_2$		$[Cu(L^1)(OAc)]$	$[Cu(L^2)(OAc)]$
P^+	223	273	P^+	503	603	P^+	346, 344	396, 394
$[P–N_2]^+$	195	245	$[P–Ar]^+$	419	469	$[P–OAc]^+$	287, 285	337, 335
$[P–CH_2=CH–$ $–CHO]^+$	167	217	$[P–C_6H_6O_2]^+$	393	493	$[P–Ar]^+$	262, 260	262, 260
$[P–Ar]^+$	139	139	$[P – 2Ar]^+$	335	335	$[P––C_6H_6O_2]^+$	236, 234	286, 284
$[P–ArN_2]^+$	111	111	$[P––2C_6H_6O_2]^+$	283	383	Ligand fragments	223, 168, 139	273, 245, 134
Ar^+	84	134	$[NiL]^+$	281	331	–	–	–
$CH_2=CH–CHO$	56	56	Ligand fragments	223, 195, 84, 56	273, 245, 139, 111, 56	–	–	–

CONCLUSIONS

Two heteroarylazo derivatives were prepared by the coupling of diazotized 2-aminothiazole and 2-aminobenzothiazole with cyclohexane-1,3-dione. Analytical, IR, ^{1}H-NMR, ^{13}C-NMR and mass spectral data revealed 1:1 products in which one of the carbonyl groups of the diketone is enolized and involved in intramolecular hydrogen bonding with one of the azo nitrogens. Analytical, physical and spectral data of the $[ML_2]$ complexes of Ni(II) and Zn(II) showed monobasic tridentate N_2O coordination involving one of the azo nitrogens, the ring nitrogen and the enolized carbonyl oxygen. The Cu(II) complexes conform to [CuL(OAc)] stoichiometry. The Zn(II) chelates are diamagnetic, while the Ni(II) and Cu(II) complexes showed normal paramagnetic moments.

ИЗВОД

ХЕТЕРОАРИЛАЗО ДЕРИВАТИ ЦИКЛОХЕКСАН-1,3-ДИОНА И ЊИХОВИ МЕТАЛНИ КОМПЛЕКСИ

MUHAMMED BASHEER UMMATHUR[1], DAMODARAN KAMALAKSHY BABU[2] и KRISHNANNAIR KRISHNANKUTTY[3]

[1]PG Department of Chemistry, KAHM Unity Women's College, Manjeri, Kerala-676122, India, [2]Department of Chemistry, Zamorin's Guruvayurappan College, Calicut, Kerala-673014, India и [3]Department of Chemistry, University of Calicut, Kerala-673635, India

У реакцији диазотизованог-2-аминотиазола и 2-аминобензотиазола са циклохексан-1,3-дионом добијени су нови тридентатни лиганди типа HL. Резултати елементалне микроанализе, IR, ^{1}H-NMR и ^{13}C-NMR спектроскопских испитивања, као и резултати добијени на основу масених спектара, указују да добијени лиганди постоје као азо--енолне таутомерне форме у којима су присутне интрамолекулске водоничне интеракције. На бази аналитичких и спектроскопских испитивања нађено је да су добијени лиганди тридентатно координовани у одговарајућим [CuL(OAc)] и [ML_2] комплексима [M = Ni(II) и Zn(II)]. Резултати магнетних испитивања су показали да је хелатни Zn(II) комплекс дијамагнетичан, док комплекси Cu(II) и Ni(II) показују очекиване парамагнетичне моменте.

(Примљено 27. децембра 2012, ревидирано 19. априла 2013)

REFERENCES

1. M. Gaber, I. A. Mansour, Y. S. Y. El-Sayed, *Spectrochim. Acta, A* **68** (2007) 305
2. S. H. Rahaman, R. Ghosh, S. K. Sarkar, B. K Ghosh, *Indian J. Chem., A* **44** (2005) 2474
3. W. Kaim, *Coord. Chem. Rev.* **230** (2002) 127
4. M. S. Masoud, G. B. Mohamed, Y. H. Abdul-Razek, A. E. Ali, F. N. Khairy, *Spectrosc. Lett.* **35** (2002) 377
5. B. Chand, U. S. Ray, G. Mostafa, T. H. Lu, C. Sinha, *Polyhedron* **23** (2004) 1669
6. A. S. Amin, *Anal. Lett.* **32** (1999) 1575
7. P. K. Santra, D. Das, T. K. Misra, R. Roy, C. Sinha, S. M. Peng, *Polyhedron* **18** (1999) 1909
8. M. M. Omar, *Ann. Chim.* **92** (2002) 601
9. I. C. Khoo, M. Y. Shih, A. Shishido, P. H. Chen, M. V. Wood, *Opt. Mater*. **18** (2001) 85
10. S. S. Kandil, *Transition Met. Chem.* **23** (1998) 461
11. I. M. A. Awad, *J. Chem. Biotechnol.* **53** (1992) 227
12. T. Yasui, N. Komatsu, K. Egami, H. Yamada A. Yuchi, *Anal. Sci.* **23** (2007) 1011
13. O. G. Khudina, Y. V. Burgart, N. V. Murashova, V. Saloutin, *Russ. J. Org. Chem.* **39** (2003) 1421
14. K. Krishnankutty, M. B. Ummathur, D. K. Babu, *J. Serb. Chem. Soc.* **75** (2010) 639
15. K. Krishnankutty, M. B. Ummathur, D. K. Babu, P. M. Philip, *J. Iran. Chem. Res.* **2** (2009) 111
16. M. B. Ummathur, *Pol. J. Chem.* **83** (2009) 1717
17. K. Krishnankutty, M. B. Ummathur, D. K. Babu, *Inorg. Chem. An Indian J.* **4** (2009) 83
18. K. Krishnankutty, P. Sayudevi, M. B. Ummathur, *J. Indian Chem. Soc.* **85** (2008) 48
19. K. Krishnankutty, P. Sayudevi, M. B. Ummathur, *J. Indian Chem. Soc.* **84** (2007) 337
20. R. C. Elderfield, *Heterocyclic compounds*, John Wiley, New York, 1950, Vol. 1, p. 555
21. L. J. Bellamy, *The Infrared Spectra of Complex Molecules*, Chapman and Hall, London, 1980

22. K. Krishnankutty, V. T. Rema, *Synth. React. Inorg. Met.-Org. Chem.* **25** (1995) 243
23. V. D. John, K. Krishnankutty, *Appl. Organomet. Chem.* **20** (2006) 477
24. N. Nakamoto, *Infrared Spectra and Raman Spectra of Inorganic and Coordination Compounds*, 5th ed., Wiley, New York, 1997
25. D. Kumar, P. K. Gupta, A. Syamal, *J. Chem. Sci.* **117** (2005) 247
26. S. J. Swamy, E. R. Reddy, D. N. Raju ,S. Jyothi, *Molecules* **11** (2006) 1000
27. B. Sarkar, M. G. B. Drew, M. Estrader, C. Diaz, A. Ghosh, *Polyhedron* **27** (2008) 2625
28. V. Ravinder, S. J. Swamy, S. Srihari, P. Lingaiah, *Polyhedron* **4** (1985) 1511
29. V. Ravinder, S. J. Swamy, S. Srihari, P. Lingaiah, *Transition Met. Chem.* **9** (1984) 103
30. K. Krishnankutty, P. Sayudevi, M. B. Ummathur, *J. Indian Chem. Soc.* **84** (2007) 518
31. K. Krishnankutty, D. K. Babu, *J. Indian Chem. Soc.* **73** (1996) 379
32. A. Lycka, J. Jirman, A. Cee, *Magn. Reson. Chem.* **28** (1990) 408
33. G. Mulongo, J. Mbabazi, B. Odongkara, H. Twinomuhwezi, G. B. Mpango, *Res. J. Chem. Sci.* **1** (2011) 102
34. a) Raman, V. Muthuraj, S. Ravichandran, A. Kulandaisamy, *Proc. Indian Acad. Sci. (Chem. Sci.)* **115** (2003) 161; b) S. Vineeta, G. Rekha, *J. Fluor. Chem.* **76** (1996) 149; c) D. C. Nonhebel, *Tetrahedron* **24** (1968) 1869
35. a) A. Farghaly, Z. A. Abdallah, *Arkivoc* (2008) 295; b) H. Budzikiewicz, C. Djerassi, D. H. Williams, *Mass spectrometry of Organic compounds*, Holden Day, San Francisco, CA, 1967
36. a) C. Zhimin, W. Yiqun, G. Donghong, G. Fuxi, *Dyes Pigm.* **76** (2008) 624; b) K. Kobayashi, K. Kurishara, K. Hirose, *Bull. Chem. Soc. Jpn.* **45** (1972) 3551
37. a) K. Ray, T. Weyhermüller, F. Neese, K. Wieghardt, *Inorg. Chem.* **44** (2005) 5345; b) K. C. Joshi, V. N. Pathak, *Coord. Chem. Rev.* **22** (1977) 37.

Journal of the Serbian Chemical Society
JSCS-info@shd.org.rs • www.shd.org.rs/JSCS
J. Serb. Chem. Soc. *79* (3) 313–324 (2014)
JSCS–4586
UDC 661.34+546.34:541.18.045:543.51
Original scientific paper

Study of the vaporization of LiI, LiI/C_{70}, LiI/LiF/C_{70} from a Knudsen cell located in the ionization chamber of a mass spectrometer

JASMINA ĐUSTEBEK#, MIOMIR VELJKOVIĆ# and SUZANA VELIČKOVIĆ*#

Vinča Institute of Nuclear Sciences, University of Belgrade, P. O. Box 522, 11001 Belgrade, Serbia

(Received 27 June 2012, revised 25 July 2013)

Abstract: The vaporization of LiI, LiI/C_{70} and LiI/LIF/C_{70} was studied using a Knudsen cell located in the ionization chamber of a magnetic sector mass spectrometer in the temperature range from 350 °C to 850 °C. The ion species, Li_nI^+ (n = 2, 3, 4 or 6) were identified from the mixture LiI/C_{70}, while the clusters Li_nI^+ and Li_nF^+ (n = 2, 3, 4, 5 or 6) were detected from a mixture LiI/LiF/C_{70}. The intensities of Li_nI^+ were higher than the emission of Li_nF^+ cluster when the ratio of LiI to LiF was 2:1. By contrast, the emission of Li_nF^+ is favored when the ratio of LiI to LiF was 1:2. These results show that the vaporization of a mixture LiI/LIF/C_{70} from a Knudsen cell located in the ionization chamber of a mass spectrometer represents an efficient and simple way to obtain and investigate clusters of the type Li_nX, X = F or I. In this work, it was also shown that the trends of the *In* (Intensity, arb. units) *versus* temperature for all Li_nI^+ clusters below and above the melting point of LiI were not same. This suggested that the manner of formation of these clusters could be different due to changes in temperature.

Keywords: “superalkali” species; Li_nI clusters; Li_nF clusters.

INTRODUCTION

A Knudsen cell with mass spectrometry (KCMS) has proven to be one of the most useful experimental techniques for investigation the equilibrium between condensed phases and complex vapor. The Knudsen effusion method involves placing a condensed sample in a Knudsen cell, with an orifice of well-defined geometry. The Knudsen cell is uniformly heated and held until equilibrium between the condensed and vapor phases is attained. The orifice dimensions must be kept less than one tenth of the mean free path of the vapor species. The vapor is continuously sampled by effusion through a small orifice in the cell. A mole-

* Corresponding author. E-mail: vsuzana@vinca.rs
# Serbian Chemical Society member.
doi: 10.2298/JSC130627083D

cular beam is formed in the KCMS and directed into a mass spectrometer for identification.[1]

The vaporization of alkali halides such as LiI and LiF by the KCMS method were investigated and discussed in terms of their vapor compositions in equilibrium with the condensed phases.[2–6] As a result, Li^+, LiX^+, Li_2X^+ and $Li_3X_2^+$ (X = F or I) ions were detected. The precursor of both Li^+ and LiX^+ was the monomer (LiX), whilst Li_2X^+ and $Li_3X_2^+$ were obtained from the dimer (Li_2X_2) and the trimer (Li_3X_3), respectively.

Since the salts of alkali metal are the strongest ion emitters, the KCMS method was also applied for investigations of their homogenous and heterogeneous clusters. Studies on metallic clusters are of considerable interest in research due to their potential application in catalytic processes, materials science, biology, and medicine.[6–10] Especially, lithium homogenous clusters have received great attention from physicists and chemists as prototypes for the investigation of the properties of metallic clusters. The existence of stable Li_2, Li_3, Li_4 and Li_5 clusters was proved experimentally and their thermodynamic properties were determined by KCMS.[11–13] The first "hypervalent" Li_3O cluster was also found by KCMS in the equilibrium vapor over Li_2O salt.[14] This method was employed to obtain other small size "hypervalent" lithium clusters, such as Li_6C, Li_4O, Li_3S, Li_4S, Li_4P, Li_2CN, Li_nH (n = 1, 2, 3 or 4) in the equilibrium vapor over the appropriate salts.15–20 Generally, "hypervalent" species possess nine or more valence electrons and these clusters are of particular importance because they violate stoichiometry based on the octet rule.[21] Due to their unusual stoichiometries, "hypervalent" clusters have large values of the first hyperpolarizabilities; therefore, they could be considered a new kind of non-linear optical species.[22] In addition, earlier investigation revealed that these clusters are important intermediates in metal cluster and metal surface reactions, which could affect the catalytic and electronic properties of a metal.[23] The most remarkable property of "hypervalent" clusters is their enormously low ionization energy (*IE*). Their ionization energies are lower than the *IE*s of the alkali metals and for this reason, they are called "superalkali".[24–29] Recently, it was theoretically also shown that "superalkali" clusters are of great significance in chemistry because they can mimic the characteristics of alkali metals and maintain their structural and electronic integrities when assembled with other species. By combining "superalkali" with another element or clusters, a new small "superatom" clusters can be formed. The "superatom" clusters represent potential building blocks for new cluster-assembled materials with unique structural, electronic, optical, magnetic and thermodynamic properties.[30–35] However, experimental results on "superalkali" clusters are scarce.

The present investigation is an extension of previous systematic studies of the way for obtaining "superalkali" clusters by the evaporation of lithium haloge-

nated salts using a thermal ionization source and a Knudsen cell in combination with a mass spectrometer.[36–43] In the earlier papers, it was shown that the experimental setup in which the Knudsen cell was located in the ionization chamber provides better conditions than the standard experimental setup of the KCMS for obtaining both the neutral and positively charged "superalkali" clusters of the type Li_nX, X = F or I (n = 2, 3, 4, 5 or 6).[40–43] However, the effects of the chemical composition of the samples which are placed in the Knudsen cell on the production of neutrals and positive ions of these clusters have not been investigated. The focus of this work was an investigation of the conditions for obtaining non-stoichiometric Li_nI and Li_nI_{n-1} clusters, from samples such as lithium iodide salt, a mixture lithium iodide/fullerene (C_{70}), a mixture of lithium iodide/lithium fluoride salt and a mixture lithium iodide/lithium fluoride/fullerene (C_{70}).

The relation between the intensity of the ions from the condensed phase and the temperature of the cell was also investigated.

EXPERIMENTAL

The standard experimental setup of the KCMS implies that the cell is placed outside the ionization chamber. In this work, the Knudsen cell was placed in the ionization chamber of a magnetic sector mass spectrometer (a 12-inch radius and 90° magnetic sector). The scheme for the ion source is presented in Fig. 1.

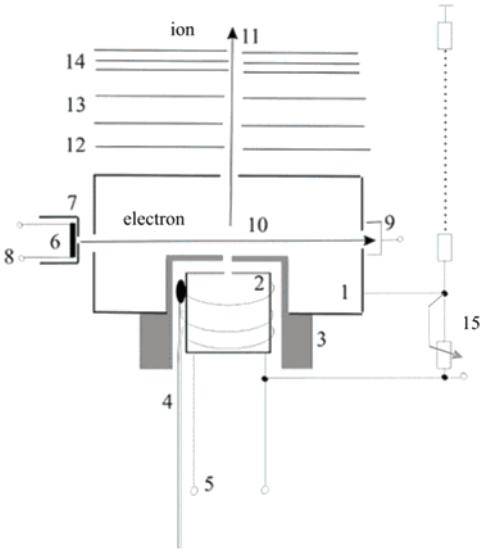

Fig. 1. Schematic diagram of the ion source: 1. ionization chamber; 2. Knudsen cell; 3. ceramic shields; 4. thermocouple; 5. heater for chamber; 6. incandescent rhenium cathode; 7. Vehnelt cylinder; 8. heater for cathode; 9. electron trap; 10. electron beam; 11. ion beam; 12. focusing electrode; 13. accelerating electrode; 14. deflectors electrode; 15. potential repeller.

The nickel Knudsen cell was heated with direct current through a tungsten wire. The height of the cell was 7 mm, the outside diameter was 6 mm and the orifice diameter was 0.1 mm. The heater was surrounded by a shield made of ceramic material. The temperature was

measured by a Pt–Pt/Rh thermo-couple attached to the cell. A cell temperature stability of ±10 K was achieved.

The experimental setup presented in Fig. 1 allows the detection of both the ionic and neutral components. Neutral species were detected in the conventional way in the electron impact ionization (EI) mode. Electrons were obtained from a rhenium cathode inside a Vehnelt cylinder and extracted by a plate at a positive potential of 15 V with respect to the cathode that was positioned at a distance 2 mm from the cathode. The clusters, electron and ion beams were mutually perpendicular. In this case, the Knudsen cell was held at the same voltage as the ionization chamber. The Knudsen cell was placed in the ionization chamber; the distance from the cell orifice to the electron beam of the ion source was about 2 mm.

In the case when the Knudsen cell was held at voltage of 30 V with respect to the ionization chamber, the experimental setup permitted the direct identification of positively charged ionic components generated in the cell, thermal ionization (TI) mode.

In this work, the Knudsen cell was used as a chemical reactor for the production of the iodine-doped lithium clusters. In all experiments, the samples weighing 0.089 g were placed into the Knudsen cell at atmospheric pressure. The samples were lithium iodide salt, a mixture lithium iodide/fullerene (C_{70}), a mixture lithium iodide/lithium fluoride salt and a mixture of lithium iodide/lithium fluoride/fullerene (C_{70}). In order to remove the adsorbed moisture, the cell with the substance was dehydrated directly in the mass spectrometer at 150 °C for several hours.

In earlier work, it has been shown that in the vapor over a salt of lithium fluoride the ions Li_2F^+ (*m*/*z* 33) and $Li_3F_2^+$ (*m*/*z* 59) clusters were obtained.[2] Also, the ions as Li_2I^+ (*m*/*z* 141) and $Li_3I_2^+$ (*m*/*z* 276) were identified to be generated from the vapor of LiI.[6] As can be observed, the peaks corresponding to the clusters of lithium fluoride were detected at lower mass than the mass of clusters of lithium iodide, for this reason, a salt LiF was used as an additional source of Li^+.

RESULTS AND DISCUSSION

In the present work, as the first step, the vaporization of lithium iodide salt by the Knudsen cell located in the ionization chamber of the magnetic sector mass spectrometer over the temperature range from 350 to 600 °C was investigated. The temperature dependence of the natural logarithm of the ion intensity at an ionizing electron energy of 40 eV for all detectable ions is shown in Fig. 2. Similar curves were obtained for other electron energies, such as 20 and 30 eV.

The following ion species were detected: I^+, I_2^+, Li^+, LiI^+, $Li_2I_2^+$, Li_2I^+, $Li_3I_2^+$ and $Li_4I_3^+$, which coincides well with previous results obtained using a standard KCMS.[6] The results obtained in the present study are compared in Table I with those obtained by other researchers.

In the present case, the relative intensities of I^+, I_2^+, Li^+, LiI^+, $Li_2I_2^+$, $Li_3I_2^+$ and $Li_4I_3^+$ to the Li_2I^+ were much larger than the literature values.[6] This indicates that the experimental setup in which the Knudsen cell is placed in the ionization chamber provides an efficient way to detect all of the above-mentioned ions.

In the second step, when a mixture LiI/C_{70} was evaporated from the Knudsen cell and electron bombardment ionization was performed, the ions I^+, I_2^+,

Li^+, LiI^+, $Li_2I_2^+$, Li_2I^+, $Li_3I_2^+$, $Li_4I_3^+$, Li_2I^+, Li_3I^+, Li_4I^+ and Li_6I^+ were observed. The natural logarithm of ion intensity as a function of temperature of the Knudsen cell for Li_2I^+, Li_3I^+, Li_4I^+, and Li_6I^+ are presented in Fig. 3. The ions I^+, I_2^+, Li^+, LiI^+, $Li_2I_2^+$, Li_2I^+, $Li_3I_2^+$, $Li_4I_3^+$ were detected at similar temperature ranges as in the case of LiI; for this reason, these ions are not shown in Fig. 3.

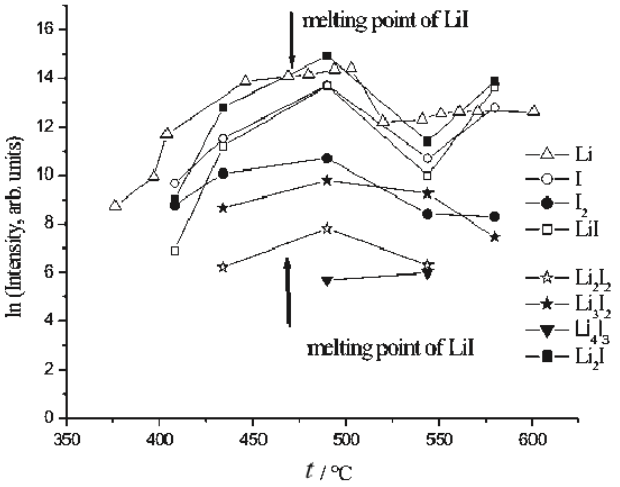

Fig. 2. The natural logarithm of the ion intensity as a function of the temperature of the Knudsen cell (*In* (Intensity, arb. units) *versus* temperature) for all detectable ions formed from the vapor over pure lithium iodide salt. These results were measured between 350 to 600 °C at 40 eV ionizing electron energy.

TABLE I. Comparison of results obtained in this work with those obtained previously[6]

Ion	Li^+	I^+	LiI^+	Li_2I^+	I_2^+	$Li_2I_2^+$	$Li_3I_2^+$	$Li_4I_3^+$	*E* / eV
Literature	16.41	6.99	42.8	100	0.95	0.72	1.67	0.19	30
This work	95.3	91.9	91.94	100	71.81	52.34	65.1	38.25	40

The threshold temperature for the start of the observation of ion signal was found to be about 355 °C for Li_nI^+ (n = 2, 3 and 4) clusters (Fig. 3). Initially the ion intensity increased with temperature, then decreased after a maximum at about 395 °C for Li_3I^+ and Li_4I^+ clusters. Above 455 °C, the emission of Li_3I^+ finally decreased to an undetectable level. The ion intensity of Li_4I^+ clusters decreased to a minimum at about 455 °C, then slightly increased, and then slightly varied with temperature (from 469 to 657 °C). By contrast, the intensity of Li_2I^+ increased to a maximum, had almost constant values in the temperature range from 467 to 593 °C and then decreased. The emission of this ion was not observed above 672 °C.

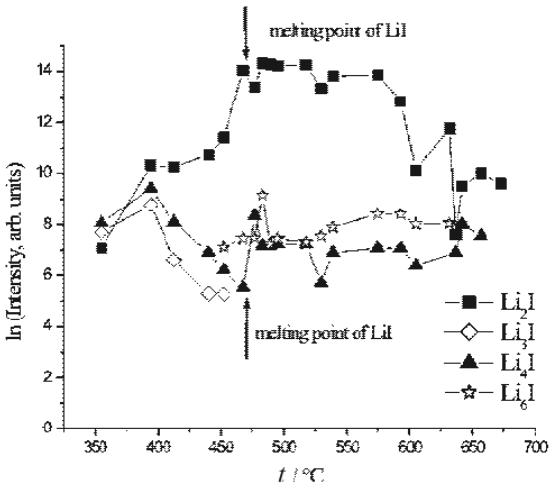

Fig. 3. The natural logarithm of the ion intensity as a function of the temperature of the Knudsen cell (*In* (Intensity, arb. units) *versus* temperature) for all detectable ions formed from the vapor over a mixture LiI/C_{70}. These results were measured from 350 to 600 °C at 40 eV ionizing electron energy.

The value of threshold temperature for observation of Li_6I^+ is lower than the temperature for the appearance of Li_nI^+ (n = 2, 3 and 4). The intensity *vs*. temperature for Li_6I^+ increases to a maximum at 485 °C, similar as with Li_2I^+. The intensity of the Li_6I^+ cluster after the maximum, somewhat decreases and has almost constant value in the temperature range from 490 to 635 °C. As it can be seen in Fig. 3, the order of the intensities was $Li_2I^+ >> Li_6I^+ > Li_4I^+$, while the Li_3I^+ cluster was not detected in the temperature range between 455 to 635 °C.

The earlier experimental study showed that Li_2I_2, Li_3I_3 and Li_4I_4 could be precursors of Li_2I^+, $Li_3I_2^+$ and $Li_4I_3^+$, respectively.[6] In the present work, it is difficult to assume exclusively precursors of Li_nI^+ (n = 2, 3, 4 and 6) clusters, based on the results presented in Fig. 3.

However, the presented results clearly show that the plot of the *In* (intensity, arb. units) *versus* temperature trends before and after the melting point of LiI (469 °C) do not correspond. At temperatures below the melting point of LiI, in a preliminary experiment, it was shown that the values of the ionization energies for Li_nI^+ (n = 2, 3 or 4) were much higher than their theoretical values. This fact implies that dimer, trimer, tetramer, $Li_3I_2^+$, and $Li_4I_3^+$ could be precursors of Li_2I^+, Li_3I^+ and Li_4I^+, respectively. Therefore, the appearance energies of Li_nI^+ could be measured at temperatures below 469 °C. On the other hand, in a previous work, it was shown that the ionization energies of Li_nI^+ (n = 2, 4 and 6) could be determined at temperatures higher than 550 °C.[41] These ionization

energies are in agreement with the *IE*s obtained by theoretical calculations, meaning that the precursors of Li_nI^+ clusters were not the same as mentioned above.

This observation suggests that the shape of the *In* (intensity, arb. units) *versus* temperature curves are different possibly due to the dissimilarity in formation mechanisms of these clusters in the Knudsen cell, such as the thermal decomposition of the evaporation species at low temperatures and the reaction of Li^+ with undecomposed LiI at high temperatures.

It should be mentioned that in previous studies, it was revealed that the clusters Li_nF^+ (n = 2, 3, 4, 5 and 6) and Li_nI^+ (n = 2, 4 and 6) were obtained in the vapor over a mixture of lithium fluoride and lithium iodide using the experimental setup presented in Fig. 1.[40,42] For this reason, in step III, the evaporation mixtures LiI/LiF/C_{70} from the Knudsen cell was studied. Both types of clusters, Li_nI^+ and Li_nF^+ (n = 2, 3, 4, 5 and 6), were obtained using a mixture LiI/LiF/C_{70}. If the ratio of LiI to LiF was 2:1, the signals of the Li_nI^+ clusters were higher than those of the Li_nF^+ clusters. By contrast, if the ratio of LiI to LiF was 1:2, signals of Li_nF^+ in the mass spectrum were higher than those of Li_nI^+. In this work, the Li_nF^+ were not studied.

At temperatures below the melting point of lithium iodide, I^+, I_2^+, Li^+, LiI^+, $Li_2I_2^+$, $Li_3I_2^+$ and $Li_4I_3^+$ were detected by the evaporation of a mixture LiI/LiF/ /C_{70}. In both cases, when a mixture LiI/LiF/C_{70} or a mixture LiIC_{70} was evaporated, the *In* (Intensity, arb. units) *versus* temperature for Li_nI^+ (n = 2, 3 and 4) had very similar trends. In addition, the intensities of all detectable ions obtained from a mixture LiI/LiF/C_{70} were lower than the intensities of ions formed from a mixture LiI/C_{70} before the melting point of LiI. This may be due to the simultaneous creation of Li_nI^+ and Li_nF^+ clusters from a mixture LiI/LiF/C_{70}, which did not occur during the evaporation of a mixture LiI/C_{70}. For this reason, the plots of the *In* (intensity, arb. units) *versus* temperature of the Li_nI^+ cluster presented in Fig. 4 were obtained at temperatures above 460 °C.

Figure 4, part A, illustrates the variation of the *In* (intensity, arb. units) *versus* temperature for the ion clusters of the type Li_nI^+ obtained by electron impact ionization. In Fig. 4, part B, the plots of the *In* (intensity, arb. units) *versus* temperature for Li_nI^+, obtained by thermal ionization in the Knudsen cell at temperatures above 835 °C, are shown. As can be seen in part B of Fig. 4, the Li_nI^+ (n = 2, 4, 5, and 6) clusters could be detected using the TI mode at temperatures higher than the melting point of LiF, while the Li_3I^+ ion was not detected by the thermal ionization.

From Fig. 4, part A, it can be seen that the intensity of Li_2I^+ and Li_4I^+ increased from 468 to 616 °C and have almost constant value in the temperature range 616 to 782 °C. The intensity of Li_2I^+ decreased above 782 °C, while a decrease in the intensity for Li_4I^+ was not detected. The intensity *versus* temperature curve for Li_3I^+ and Li_5I^+ had almost constant values in the temperature

range presented in Fig. 4. As can be seen, the order of the intensities was Li_2I^+ > > Li_6I^+ or Li_4I^+ > Li_5I^+ > Li_3I^+ at temperatures between 600 and 830 °C. This result showed that the intensities of Li_nI^+ increase when a salt LiF was added to a mixture LiI/C_{70}.

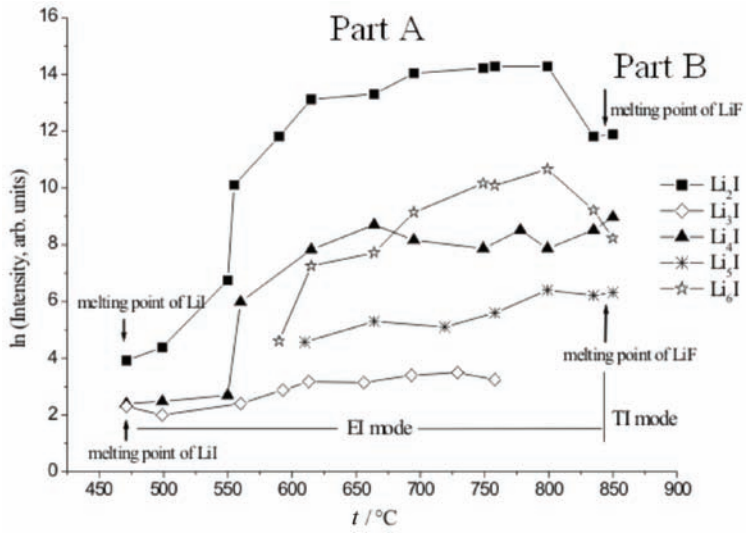

Fig. 4. Plots of *In* (Intensity, arb. units) *versus* temperature. The ions Li_nI (n = 2, 3, 4, 5 or 6) clusters were obtained in the electron impact mode (the temperature range of the Knudsen cell was 420 to 830 °C) and the positively charged clusters Li_nI^+ (n = 2, 4, 5 and 6) were generated in the Knudsen cell by thermal ionization (the temperature of the Knudsen cell was higher than 830 °C).

However, it should be noted that the Li_3I^+ and Li_5I^+ clusters were not detected from a mixture LiI/LiF.[40] In addition, the *In* (Intensity, arb. units) *versus* temperature trend for the mixture LiI/LiF did not correspond to the trend for the mixture LiI/LiF/C_{70}.[40] This implies that the presence of both C_{70} and LiF provides optimal conditions for obtaining ions Li_nI^+ n = 2, 3, 4, 5 and 6. Namely, in an earlier experiment, it has been shown that the solid-state reactions of fullerenes with various metal fluorides can be performed in a Knudsen cell. For example, the mass spectra recorded during the KCMS fluorination of C_{70} with MnF_3 contained $C_{70}F_{36}$, $C_{70}F_{38}$ and $C_{70}F_{40}$.[44] Furthermore, the reaction of fluorination of C_{70} is more efficient than the reaction of fullerene with lithium.[45] These facts suggest that the enhanced stability of Li_n^+ may be related to the presence of an additional Li source that remains in the Knudsen cell because the fluorine atom prefers a strong ionic bound with C_{70}. From another viewpoint, the fullerene C_{70} could form a graphite monolayer on the inner surface of the Knudsen cell at higher temperatures. Generally, the existence of a graphite monolayer decreases the thermal dissociation of the clusters.[46]

For clarity, the ions obtained by evaporation from pure LiI, a mixture LiI/C_{70}, and a mixture LiI/LiF/C_{70}, in the temperature range derived from the curves in Figs. 2 and 3, are summarized in Table II.

TABLE II. The ions obtained by the evaporation from pure LiI, from a mixture of LiI/C_{70} and from a mixture of LiI/LiF/C_{70}, and the temperature range of the Knudsen cell

Sample	Ions	Ions of the type Li_nI^+	Temperature range, °C
LiI	I^+, I_2^+, Li^+, LiI^+,	Li_2I^+	408–581
	$Li_2I_2^+$, $Li_3I_2^+$, $Li_4I_3^+$		
LiI/C_{70}		Li_2I^+,	355–673
	I^+, I_2^+, Li^+, LiI^+,	Li_3I^+,	355–453
	$Li_2I_2^+$, $Li_3I_2^+$, $Li_4I_3^+$	Li_4I^+,	355–658
		Li_6I^+	452–632
LiI/LiF/C_{70}	I^+, I_2^+, Li^+, LiI^+,	Li_2I^+,	355–837
	$Li_2I_2^+$, $Li_3I_2^+$, $Li_4I_3^+$	Li_3I^+,	355–758
		Li_4I^+,	355–835
		Li_5I^+,	609–837
		Li_6I^+	452–833

Comparing data in the Table II, a few general trends can be noted. First, the fullerene C_{70} provide a wider temperature range for the detection of Li_nI^+ clusters. Second, the addition of the salt LiF to a mixture LiI/C_{70} leads to an increase in the temperature range for the observation of these ions. This suggests that the formation of cluster ions is favored when the extra sources of lithium ions were present in the Knudsen cell.

CONCLUSIONS

In this work, the evaporation of LiI, LiI/C_{70} and LiI/LIF/C_{70} from a Knudsen cell located in the ionization chamber of a magnetic sector mass spectrometer was studied. The following ion species were detected: I^+, I_2^+, Li^+, LiI^+, $Li_2I_2^+$, $Li_3I_2^+$, $Li_4I_3^+$ and Li_nI^+ ($n > 2$). In all of three cases, the intensities of these ions *versus* temperature of the Knudsen cell were measured. The principal results were as follows:

1. The results indicate that the experimental setup where the Knudsen cell was placed in the ionization chamber provided abundances of all the detectable ions higher than did those obtained with a standard KCMS.

2. By evaporation of the mixture LiI/C_{70}, ions of Li_nI (n = 2, 3, 4 and 6) clusters were obtained, while evaporation of the mixture LiI/LiF/C_{70} gave positive ions of Li_nI (n = 2, 3, 4, 5 and 6). The presence of both C_{70} and LiF provides optimal conditions for obtaining Li_nI^+ (n = 2, 3, 4, 5 and 6).

3. In all three cases, the most intensive peaks in the spectra were Li_2I^+. The clusters with an even number of lithium atoms (Li_2I^+, Li_4I^+, Li_6I^+) were more stable than the clusters with an odd number of lithium atoms (Li_5I^+ and Li_3I^+).

4. Trends of the plot *In* (Intensity, arb. units) *versus* temperature for Li_nI^+ cluster before and after the melting point of LiI do not correspond. It suggests that way of formation of these clusters could be different due to changes in the temperature. At temperatures below the melting point of lithium iodide, the dissociative ionization of $(LiI)_2$, $(LiI)_3$, $(LiI)_4$, $Li_3I_2^+$, and $Li_4I_3^+$ could be responsible for the generation of Li_2I^+, Li_3I^+ and Li_4I^+, respectively. Unfortunately, based on all the detectable ions, the predominant emission mechanism could not be experimentally determined at temperature higher than the melting point of lithium iodide.

5. The clusters Li_nI and Li_nF were obtained by evaporation of the mixture LiI/LiF/C_{70}. The intensities of Li_nI clusters were higher than the emission of Li_nF cluster when the ratio of LiI to LiF was 2:1. In contrast, the emission of Li_nF clusters was enhanced, while the emission of Li_nI clusters was suppressed when the ratio of LiI to LiF was 1:2.

It could be concluded that a Knudsen cell located in the ionization chamber of a mass spectrometer provides an appropriate way to obtain and investigate clusters of the type Li_nX, X = F or I.

Acknowledgement. The authors acknowledge the Ministry of Education, Science and Technological Development of the Republic of Serbia for financial support (Contract No. 172019).

ИЗВОД

ИСПИТИВАЊЕ ОТПАРАВАЊА LiI, LiI/C_{70} И LiI/LiF/C_{70} ИЗ КНУДСЕНОВЕ ЋЕЛИЈЕ СМЕШТЕНЕ У ЈОНИЗАЦИОНУ КОМОРУ МАСЕНОГ СПЕКТРОМЕТРА

ЈАСМИНА ЂУСТЕБЕК, МИОМИР ВЕЉКОВИЋ и СУЗАНА ВЕЛИЧКОВИЋ

Институт за нуклеарне науке Винча, Универзитет у Београду, Поштански фах 522, 11001, Београд

Отпаравање LiI, LiI/C_{70} и LiI/LIF/C_{70} је испитивано помоћу Кнудсенове ћелије, која је смештена у јонизациону комору магнетног масеног спектрометра, у температурском опсегу од 350 до 850 °C. Li_nI^+ (n = 2, 3, 4 и 6) врсте су детектоване из смеше LiI/C_{70}, а кластери Li_nI^+ и Li_nF^+ (n = 2 до 6) су детектовани испаравањем смеше LiI/LiF/C_{70}. Интензитет Li_nI^+ био је већи од интензитета Li_nF^+ кластера када је однос LiI и LiF био 2:1. С друге стране, стварање Li_nF^+ кластера је фаворизовано када је однос LiI и LiF био 1:2. Резултати показују да отпаравање смеше LiI/LIF/C_{70} из Кнудсенове ћелије, која је смештена у јонизациону комору масеног спектрометра, представља ефикасан и једноставан начин за добијање и испитивање кластера типа Li_nX, X = F или I. У овом раду такође је показано да се зависност природног логаритма интензитета Li_nI^+ кластера од температуре разликује на температурама пре и после тачке топљења LiI. Ово указује на то да начин формирања наведених кластера може бити различит услед промене температуре.

(Примљено 27. јуна 2012, ревидирано 25 јула 2013)

REFERENCES

1. E. H. Copland, N. S. Jacobson, *Electrochem. Soc. Interface* **10** (2001) 28

2. M. Yamawaki, M. Hirai, M. Yasumoto, M. Kanno, *J. Nucl. Sci. Technol*. **19** (1982) 563
3. L. Friedman, *J. Chem. Phys.* **23** (1955) 477
4. L. N. Gorokhov, *Dokl. Akad. Nauk. SSSR* **142** (1962) 113
5. J. Berkowitz, H. A. Tasman, W. A. Chupka, *J. Chem. Phys.* **36** (1962) 2170
6. L. Bencez, A. Lesar, A. Popovic, *Rapid Commun. Mass Spectrom*. **12** (1998) 917
7. G. Mills, M. S. Gordon, H. Metiu, *Chem. Phys. Lett*. **359** (2002) 493
8. A. K. Santra, D. W. Goodman, *J. Phys.: Condens. Matter* **15** (2003) R31
9. R. R. Zope, T. Baruah, *Phys. Rev., A* **64** (2001) 053202
10. C. Majumder, A. K. Kandalam, P. Jena, *Phys. Rev., B* **74** (2006) 205437
11. L. Xiao, L. Wang, *Chem. Phys. Lett*. **392** (2004) 452
12. C. H. Wu, *J. Chem. Phys*. **65** (1976) 3181
13. C. H. Wu, *J. Am. Chem. Soc*. **19** (1980) 71
14. C. H. Wu, *J. Chem. Phys.* **91** (1989) 546
15. H. Kudo, C. H. Wu, H. R. Ihle, *J. Nucl. Mater*. **78** (1978) 380
16. H. Kudo, M. Hashimoto, K. Yokoyama, C. H. Wu, A. E. Dorigo, F. M. Bickelhaupt, P. v. R. Schleyer, *J. Phys. Chem*. **99** (1995) 6477
17. M. Hashimoto, K. Yokoyama, H. Kudo, C. H. Wu, P. v. R. Schleyer, *J. Phys. Chem*. **100** (1996) 15770
18. H. Kudo, M. Hashimoto, K. Yokoyama, C. H. Wu, P. v. R. Schleyer, *Thermochim. Acta* **299** (1997) 113
19. H. Kudo, K. Yokoyama, *Bull. Chem. Soc. Jpn.* **69** (1996) 1459
20. H. Kudo, M. Hashimoto, H. Tanaka, K. Yokoyama, *J. Mass Spectrom. Soc. Jpn.* **47** (1999) 2
21. S. E. Wheeler, K. W. Sattelmeyer, P. v. R. Schleyer, H. F. Schaefer, *J. Chem. Phys*. **120** (2004) 4683
22. P. v. R. Schleyer, P. O. Löwdin, B. Pullma, *New Horizons of Quantum Chemistry*, Reidel Publishers, Dordrecht, Netherlands, 1983, p. 95
23. Y. Li, D. Wu, *Chem. J. Chin. Univ*. **31** (2010) 1811
24. M. J. Polce, C. Westdemiotis, *Int. J. Mass Spectrom.* **182** (1999) 45
25. E. Rehm, A. I. Boldyrev, P. v. R. Schleyer, *Inorg. Chem*. **31** (1992) 4834
26. G. L. Gutsev, A. I. Boldyrev, *Chem. Phys. Lett.* **92** (1982) 262
27. G. L. Gutsev, A. I. Boldyrev, *Chem. Phys.* **56** (1981) 277
28. V. G. Zakrzewski, W. V. Niessen, A. I. Boldyrev, P. v. R. Schleyer, *Chem Phys. Lett.* **197** (1992) 195
29. X. B. Wang, C. F. Ding, L. S. Wang, A. I. Boldyrev, J. J. Simons, *Chem. Phys.* **110** (1999) 4763
30. A. N. Alexandrova, A. I. Boldyrev, Y. J. Fu, X. Yang, X. B. Wang, L. S. J. Wang, *Chem. Phys*. **121** (2004) 5709
31. P. J. S. N. Khanna, *Phys. Rev., B.* **55** (1995) 13705
32. Y. Li, D. Wu, Z. R. Li, *Inorg. Chem.* **47** (2008) 9773
33. S. N. Khanna, A. C. Reber, A. W. Castleman, *J. Am. Chem. Soc.* **129** (2007) 10189
34. J. Tong, Y. Li, D. Wu, Z. R. Li, X. R. Huang, *J. Phys. Chem., A* **115** (2011) 2041
35. S. A. Claridge, A. W. J. Castleman, S. N. Khanna, C. B. Murray, A. Sen, P. S. Weiss, *ACS Nano* **3** (2009) 244
36. S. R. Velickovic, V. R. Djordjevic, J. M. Cveticanin, J. B. Djustebek, M. V. Veljkovic, O. M. Neskovic, *Rapid Commun. Mass Spectrom*. **20** (2006) 3151
37. S. R. Velickovic, J. K. Vasil, J. N. Belosevic Cavor, V. R. Djordjevic, J. M. Cveticanin, J. B. Djustebek, M. V. Veljkovic, O. M. Neskovic, *Chem. Phys. Lett*. **448** (2007) 151

38. S. Veličković, V. Djordjević, J. Cvetićanin, J. Djustebek, M. Veljković, O. Nešković, *Vacuum* **83** (2009) 378
39. S. R. Veličković, J. B. Djustebek, F. M. Veljković, B. B. Radak, M. V. Veljković, *Rapid Commun. Mass Spectrom.* **26** (2012) 443
40. J. Djustebek, S. Veličkovic, S. Jerosimić, M. Veljković, *J. Anal. At. Spectrom*. **26** (2011) 1641
41. S. R. Veličković, J. B. Đustebek, F. M. Veljković, M. V. Veljković, *J. Mass Spectrom.* **47** (2012) 627
42. J. Djustebek, S. Veličković, F. Veljković, M. Veljković, *Digest J. Nanomater. Biostruct*. **7** (2012) 1365
43. J. Djustebek, M. Milovanović, S. Jerosimić, M. Veljković, S. Veličković, *Chem. Phys. Lett.* **556** (2013) 380
44. O. Boltalina, A. Gorynkov, V. Markov, I. Ioffe, L. Sidorov, *Int. J. Mass Spectrom.* **228** (2003) 807
45. D. Zhang, J. Wu, J. Yan, *J. Mol. Struct.* **282** (1993) 187.
46. S. Hofmann, J. Robertson, C. Ducati, R. E. Dunin-Borkowski, *Nanotechnology* **15** (2004) 601.

Journal of the Serbian Chemical Society
JSCS-info@shd.org.rs • www.shd.org.rs/JSCS
J. Serb. Chem. Soc. *79* (3) 325–330 (2014) UDC 537.872:544.478–44+544.032.1:621.397.3
JSCS–4587 *Extended abstract*

EXTENDED ABSTRACT

Impact of the spatial distribution of morphological patterns on the efficiency of electrocatalytic gas evolving reactions•

ALEKSANDAR R. ŽERAĐANIN*

Department of Interface Chemistry and Surface Engineering, Max-Planck-Institut für Eisenforschung, Max-Planck-Straße 1, 40237 Düsseldorf, Germany

(Received 1 October 2013)

Abstract: The efficiency of electrocatalytic gas evolving reactions (hydrogen, chlorine and oxygen evolution) is a key challenge for important industrial processes, such as chlor-alkali electrolysis or water electrolysis. The central issue for the aforementioned electrocatalytic processes is their huge power consumption. Experimental results accumulated in the past, as well as some predictive models ("volcano" plots) indicate that altering the nature of the electrode material cannot significantly increase the activity of the mentioned reactions. Consequently, it is necessary to find a qualitatively different strategy for improving the energy efficiency of electrocatalytic gas evolving reactions. A usually disregarded fact is that gas evolution is an oscillatory phenomenon. Given the oscillatory behavior, a key parameter of macrokinetics of gas electrode is the frequency of gas-bubble detachment. Bearing in mind that gas evolution greatly depends on the surface morphology, a methodology is proposed that establishes a rational link between the morphological pattern of an electrode with its activity and stability. Characterization was performed using advanced analytical tools. The frequency of gas-bubble detachment was obtained in the configuration of scanning electrochemical microscopy (SECM), while the corrosion stability was analyzed using a miniaturized scanning flow electrochemical cell connected to a mass spectrometer (SFC–ICPMS).

Keywords: energy efficiency; electrocatalysis; morphology; SECM; activity; stability.

Due to their technical importance, electrocatalytic gas-evolving reactions (hydrogen, chlorine and oxygen evolution) have been the subject of investigation for decades.[1–3] From well-established large scale industrial processes, such as chlor-alkali technology towards water electrolysis and electrochemical CO_2

* Correspondence on E-mail: zeradjanin@mpie.de
doi: 10.2298/JSC131002106Z
• The lecture given at meeting of Electrochemical Section of the Serbian Chemical Society, held on 5 May, 2013.

reduction, the efficiency of electrocatalytic gas evolving reactions (GER) has been a major challenge due to the large amount of electricity necessary to conduct electrode reactions at a desirable rate.[4] Energy efficiency in one electrochemical reactor is usually monitored by the voltage corresponding to the predefined turnover of product controlled by the imposed current intensity. An essential task is to minimize the overvoltage, which represents the difference between the actual voltage and the voltage in the state of equilibrium (reversible voltage).

The energy efficiency during one electrocatalytic process strongly depends on the design of the electrochemical interface. The functionality of an electrochemical interface is largely influenced by the nature of the material of the chosen electrode that belongs to the scope of electrocatalysis.[2] Electrocatalysis essentially deals with the impact of the electrode material on the rate of an electrode reaction. The predictive bases on which electrocatalysis rests are empirical or theoretical models known as "volcano" plots, in which the kinetics of the electrode reaction is expressed as a function of some catalytic descriptor, which is in fact some physicochemical property of the material (binding energy of intermediates, number of outer electrons, *etc*.).[5] The apex of "volcano" responds to the maximal kinetics, which is essentially determined by the optimal value of a catalytic descriptor (Sabatier Principle). For example, a noticeable fact is that RuO_2 is at the apex of the "volcano" plot for the oxygen evolution reaction (OER) and the chlorine evolution reaction (CER).[6,7] If a material whose activity responds to the maximum of the "volcano" plot is identified, the question that would naturally arise is: how to improve further the efficiency of the given reaction?

A high intrinsic activity of the chosen electrocatalyst, reflected by the high turnover per active site, however, goes hand in hand with a certain self-inhibiting effect. Namely, the phenomenon of supersaturation with the product is actually a prerequisite for the gas formation.[8,9] The formed gas-bubbles cover a fraction of the active surface area and induce additional overpotential. It is important to mention that the gas bubble effect was detected to be the major source of overpotential in a case of chlor-alkali technology.[2] Consequently, this issue requires serious investigations, which could be beneficial for all gas-evolving reactions, even for those that are not driven by the electrode potential. At the same time, electrode materials, especially those used as catalysts for anodic electrocatalytic reactions, are subjected to intensive corrosion.[10] The electrode materials used to catalyze the mentioned electrode reactions usually originate from the family of noble metal oxides. Considering that the price of noble metals is subject to unpredictable fluctuations (for example, the price of Ru jumped in 2007/2008 by 1000 %[11]), it is of major importance to find strategies to 1) stabilize electrocatalytic materials, 2) reduce the loading with noble metals and/or 3) replace noble metals with cheaper and more abundant materials.

A promising approach to address the above-mentioned issues is a rational design of the surface morphology. Namely, morphology has strong impact on the gas evolution (for example, it influences the contact angle at the triple phase boundary) and influences the utilization of the active surface area by determining the accessibility of active sites.[12] Additionally, expecting that high local over-potentials and current densities could enhance degradation of electrocatalysts,[13] it is essential to investigate to what extent the stability of electrocatalysts is influenced by the morphological pattern. State of the art anodes for the electro-catalytic gas evolution are DSA (dimensionally stable anodes)-type electrodes. Usually, "valve" metal-like titanium is coated with a mixed transition metal oxide. Catalytically, the active component is a noble metal-based oxide (for example ruthenium oxide), the long-term stability of which is assured by mixing with a "valve" metal-based oxide (for example titanium oxide). An important pre-condition for mixed oxide formation is that the parameters of the crystal lattice match (according to the Hume Rothery Rules).[14] A typical morphological pattern of DSAs, the so-called "mud-crack" structure, contains two interesting features, namely "islands" and "channels", which could be potentially beneficial. The edges of the islands can allow high local activities, while the channels can contribute to mass transport by allowing certain internal hydraulic regimes *via* microconvection.

Two studies provide particularly interesting insights into the behavior of DSAs. Trasatti and co-workers derived a method to distinguish easily accessible "outer" surface area from the hardly accessible "inner" surface area (originating in nanopores, *etc*.).[15] In the mentioned work, the authors stated that only the outer surface is functional and accessible for the reaction. Simultaneously, Evdokimov reported that at very high current densities (up to 4 A cm^{-2}), the inner surface area starts to participate in the reaction.[16,17] The results of Evdokimov could be understood in terms of an increase of the interfacial overpressure, which allows solvent penetration towards the nanopores (according to the Young–Laplace Equation for capillary forces).[18] While Evdokimov was increasing the imposed intensity of the process (rate of reaction) at the analyzed electrode, the question was whether the opposite was possible. Namely, whether it is possible for the pre-defined intensity of the process to gradually change the morphology and cause activation of the inner surface area or at least increase its utility. To achieve better utility of surface area, it is important to bear in mind that gas evolution is an oscillatory phenomenon.[19] Thermal oscillations of the gas-bubbles cause periodic displacement of the surrounding liquid, which in return influences the root of the surrounding gas-bubbles and ultimately cause their detachment. The smaller the gas-bubbles are, the more frequently they oscillate and finally detach. Consequently, given the oscillatory behavior, a key parameter of the macrokinetics of a gas-evolving electrode is the frequency of gas-bubble detachment. In

this sense, the goal was to find a way to generate gas-bubbles with small radius at electrode/electrolyte interface. Knowing that gas bubble evolution consists of three processes: 1) nucleation, 2) growth and coalescence and 3) detachment, it seems rational to design electrodes with adequate thickness of the catalyst layer and size of the "channels" so the gas bubbles can nucleate inside the "channels" that would limit their growth. In this respect, the thickness of the coating and size of the "channels" should be similar to the critical radius of gas-bubble nucleation.[20] To achieve the targeted pattern, the synthesis was based on controlling the tensile stress in the catalyst layer. The tensile stress delivered to the coating could be controlled by adequate thermal treatment (calcination temperature, rate of heating/cooling…) and by creating mismatch in the coefficients of thermal expansion between support and catalyst layer. In this sense, the "breakage" of the catalyst layer is under certain measures of control as is the size of the "channels". Besides the design of the morphological pattern, it was important to ensure that the desirable surface features are uniformly distributed over the surface.[21] While DSA coatings were usually synthesized using the thermal decomposition procedure, important progress was made through the introduction of sol–gel route, as shown by Nikolić and co-workers.[22] The sol–gel procedure allowed coatings to be obtain with significantly reduced surface inhomogeneities in the morphology and/or composition. Reducing surface inhomogeneities is already recognized as an important aspect of electrode design and as one of the potential strategies for further improvement of DSA performance.[23] Although, the impact of the spatial distribution of activity on electrode performance is still not adequately understood, it has been proven to be of major importance for efficient gas evolution.[21]

Besides the design of the features of the electrode surface, of major importance is simultaneously to have a realistic insight into the catalytic performance of a particular material, which further strongly depends on the employment of adequate analytical tools and procedures. Particularly important was to characterize and adequately interpret gas-bubble evolution. The frequency of gas bubble detachment at various potentials was monitored using scanning electrochemical microscopy (SECM).[24] This is the first work in which an SECM setup was adopted for the characterization of GER by recording potential dependent frequency spectra. From the recorded spectra, the point of transition from pseudo-periodical to periodical behavior could be detected, which was related with a drop in the efficiency. All the tested DSA coatings for which a characteristic frequency of the gas-bubble detachment could not be estimated exhibited relatively low activity. This could be related to the spatial distribution of the activity, which can also be visualized *in situ* using SECM.[21,25] Finally SECM in combination with cyclic voltammetry (CV) was used for the most challenging task, namely to develop a methodology that quantifies what fraction of the catalyst layer (what percentage of overall active sites) really participate in the reaction in dependence

on the applied potential. Finally, as a part of an analysis of catalyst stability, time resolved dissolution profiles were recorded using a recently developed setup based on the coupling of electrochemistry with mass spectrometry (SFC–ICPMS).[26,27] From the dissolution profiles, it was clear that the more active sample, due to the morphological pattern that promotes efficient gas evolution and assures a larger effective surface area, at the same time could be more stable, which is of major importance on a technical scale.

Acknowledgment. Bundesministerium für Bildung und Forschung (BMBF) for financial support within the framework of the Project ECCO2 (Kz: 033RC1101A).

И З В О Д

УТИЦАЈ ПОВРШИНСКЕ МОРФОЛОГИЈЕ НА ЕФИКАСНОСТ РЕАКЦИЈА СА ИЗДВАЈАЊЕМ ГАСА

АЛЕКСАНДАР Р. ЖЕРАЂАНИН

Department of Interface Chemistry and Surface Engineering, Max-Planck-Institut für Eisenforschung, Max-Planck-Straße 1, 40237 Düsseldorf, Germany

Ефикасност електрокаталитичких реакција са издвајањем гаса (издвајање водоника, хлора и кисеоника) је кључни изазов за важне индустријске процесе као што су хлор–алкална електролиза или електролиза воде. Централни изазов за наведене електрокаталитичке процесе је огромна потрошња електричне енергије. Експерименталне чињенице акумулиране током претходне четири деценије, као и неки важни експериментални и теоретски модели ("вулканске" криве) указују да мењање природе електродног материјала не може битно увећати активност поменутих реакција. Сходно томе, неопходно је пронаћи квалитативно другачији приступ за побољшање енергетске ефикасности електрокаталитичких реакција са издвајањем гаса. Чињеница која се обично занемарује јесте да је издвајање гаса осцилаторни феномен. С обзиром на осцилаторно понашање, кључни параметар макрокинетике гасних електрода јесте фреквенција издвајања мехурова гаса. Имајући у виду да издвајање гаса у великој мери зависи од површинске морфологије, предложена је методологија која успоставља рационалну везу између морфологије електроде и њене активности и стабилности. Карактеризација је извршена коришћењем модерних аналитичких метода. Фреквенција издвајања гаса је добијена у конфигурацији скенирајуће електрохемијске микроскопије (SECM) док је корозиона стабилност анализирана уз помоћ минијатуризованог проточног електрохемијског реактора повезаног са масеним спектрометром. (SFC–ICPMS).

(Примљено 1. октобра 2013)

REFERENCES

1. J. O'M. Bockris, *J. Electrochem. Soc.* **131** (1984) 290
2. S. Trasatti, *Electrochim. Acta* **45** (2000) 2377
3. J. Suntivich, K. J. May, H. A. Gasteiger, J. B. Goodenough, Y. Shao-Horn, *Science* **334** (2011) 1383
4. N. S. Lewis, D. G. Nocera, *Proc. Natl. Acad. Sci.* **103** (2006) 15729
5. A. R. Zeradjanin, N. Menzel, P. Strasser, W. Schuhmann, *ChemSusChem* **5** (2012) 1897
6. S. Trasatti, *Electrochim. Acta* **29** (1984) 1503

7. I. C. Man, H.-Y. Su, F. Calle-Vallejo, H. A. Hansen, J. I. Martínez, N. G. Inoglu, J. Kitchin, T. F. Jaramillo, J. K. Nørskov, J. Rossmeisl, *ChemCatChem* **3** (2011) 1159
8. H. Vogt, *J. Appl. Electrochem*. **23** (1993) 1323
9. N. P. Brandon, G. H. Kelsall, *J. Appl. Electrochem*. **15** (1985) 475
10. G. N. Martelli, R. Ornelas, G. Faita, *Electrochim. Acta* **39** (1994) 1551
11. J. Pérez-Ramírez, C. Mondelli, T. Schmidt, O. F.-K. Schlüter, A. Wolf, L. Mleczko, T. Dreier, *Energy Environ. Sci*. **4** (2011) 4786
12. S. Ardizzone, *J. Electrochem. Soc*. **129** (1982) 1689
13. B. V. Tilak, V. I. Birss, J. Wang, C.-P. Chen, S. K. Rangarajan, *J. Electrochem. Soc.* **148** (2001) D112
14. R. D. Shannon, *Solid State Commun.* **6** (1968) 139
15. S. Ardizzone, G. Fregonara, S. Trasatti, *Electrochim. Acta* **35** (1990) 263
16. S. V. Evdokimov, *Russ. J. Electrochem.* **36** (2000) 236
17. S. V. Evdokimov, *Russ. J. Electrochem.* **36** (2000) 489
18. H. Wendt, *Electrochim. Acta* **39** (1994) 1749
19. I. G. Malenkov, *J. Eng. Phys.* **20** (1971) 704
20. A. R. Zeradjanin, F. La Mantia, J. Masa, W. Schuhmann, *Electrochim. Acta* **82** (2012) 408
21. R. Chen, V. Trieu, A. R. Zeradjanin, H. Natter, D. Teschner, J. Kintrup, A. Bulan, W. Schuhmann, R. Hempelmann, *Phys. Chem. Chem. Phys*. **14** (2012) 7392
22. V. V. Panić, A. Dekanski, S. K. Milonjić, R. T. Atanasoski, B. Ž. Nikolić, *Colloids Surfaces, A* **157** (1999) 269
23. H. Over, *Electrochim. Acta* **93** (2013) 314
24. A. R. Zeradjanin, E. Ventosa, A. S. Bondarenko, W. Schuhmann, *ChemSusChem* **5** (2012) 1905
25. A. R. Zeradjanin, T. Schilling, S. Seisel, M. Bron, W. Schuhmann, *Anal. Chem*. **83** (2011) 7645
26. A. A. Topalov, I. Katsounaros, M. Auinger, S. Cherevko, J. C. Meier, S. O. Klemm, K. J. J. Mayrhofer, *Angew. Chem. Int. Ed*. **51** (2012) 12613
27. S. Cherevko, A. A. Topalov, A. R. Zeradjanin, I. Katsounaros, K. J. J. Mayrhofer, *RSC Adv*. **3** (2013) 16516.

Journal of the Serbian Chemical Society
JSCS-info@shd.org.rs • www.shd.org.rs/JSCS
J. Serb. Chem. Soc. 79 (3) 331–340 (2014) UDC 678.023.3+541.44'131:543.42–74:543.2
JSCS–4588 *Original scientific paper*

The application of NIR spectroscopy with chemometric analysis for monitoring a powder blending process

LJILJANA B. MARIĆ[1], BRANISLAV D. JOVIĆ[2#], SLOBODAN D. PETROVIĆ[3#], ALEKSANDAR M. NIKOLIĆ[2] and IRENA J. HOMŠEK[1*]

[1]Galenika ad, Batajnički drum bb, 11080 Belgrade, Serbia, [2]Faculty of Sciences, University of Novi Sad, 21000 Novi Sad, Serbia and [3]Faculty of Technology and Metallurgy, University of Belgrade, 11000 Belgrade, Serbia

(Received 1 April, revised 14 July 2013)

Abstract: This paper reports the use of near infrared (NIR) spectroscopy as a process analytical technology (PAT) tool for monitoring the metformin (*N*,*N*-dimethylimidodicarbonimidic diamide) hydrochloride and poly(vinyl pyrrolidone) (PVP) mixing process, which is the first stage in tablet production. Blend homogeneity was tested using the non-invasive NIR spectroscopy method and the partial least squares (PLS) regression model was applied for the analysis of the obtained spectra. Simultaneously, the critical parameter (metformin hydrochloride content) was monitored by a classical analytical technique, the validated HPLC method, commonly used for this purpose. Based on the high sensitivity of the model developed in this study, as well as the established correlation among the results obtained by different methods, it could be concluded that the proposed rapid and non-invasive technique could be an effective tool for the monitoring of one of the critical manufacturing steps in the production solid dosage forms.

Keywords: PAT; NIR spectroscopy; PLS; metformin hydrochloride; blend uniformity analysis.

INTRODUCTION

Process analytical technology (PAT) is defined by the United States Food and Drug Administration (FDA) in the document *Guidance for Industry: PAT – A Framework for Innovative Pharmaceutical Manufacturing and Quality Assurance* as "a system for designing, analyzing, and controlling manufacturing through timely measurements (*i.e.*, during processing) of critical quality and performance attributes of raw and in-process materials and processes with the goal of ensuring final product quality".[1]

* Corresponding author. E-mail: irena.homsek@gmail.com
# Serbian Chemical Society member.
doi: 10.2298/JSC010413080M

Near infrared (NIR) spectroscopy has gained wide acceptance in the agricultural, food and petrochemical industries as a powerful, non-destructive analytical technique. It is an important component of a PAT toolbox, and is the key for enabling Real-Time Release of pharmaceutical tablets. The main advantages of NIR spectroscopy are its rapidity and reliability for on-line and in-line analyses of different products and materials.[2]

Recently, NIR spectroscopy has found increasing use in pharmaceutical analysis for the identification and quality testing of raw materials,[3,4] the monitoring of blending,[5] granulation,[6] moisture content,[5] active substance content,[7–9] roller compaction,[10] drying operations[11] and many other applications.[12]

The preparation of a uniform blend prior to tableting or encapsulation is one of the most important steps in the production of solid dosage forms. Among the various techniques that are applied for this purpose, one-pot processing is a term that includes any technology that combines different unit operations of a pharmaceutical production process into one machine. It is the production of pharmaceutical granules using a wet granulation process in which dry mixing, liquid addition, wet granulation, drying and sizing of the granules are all performed in the same processing vessel.[13] The concept of a single pot processor is to ensure continuous processing. Usually, the determination of homogeneity of a powder blend requires stopping the production process, taking samples and its analysis by some of the most commonly used analytical methods (UV/Vis, HPLC, *etc*.), which are time-consuming. As most of pharmaceutical excipients and active pharmaceutical ingredients (APIs) absorb IR radiation, NIR spectroscopy may be used for drug content determination in order to define the mixing time end-point. In contrast to the conventional methods, NIR spectroscopy in combination with chemometric analysis is an easy, fast and non-destructive analytical technique for quantification of active ingredients in solid samples.

The assay methods for metformin (*N*,*N*-dimethylimidodicarbonimidic diamide) hydrochloride in a powder blend were either HPLC,[14–16] gas chromatography,[17,18] NMR spectrometry,[19] and UV-spectroscopy[20] In contrast to these conventional methods that depend, predominantly, on sample dissolution in a suitable solvent, NIR spectroscopy combined with chemometrical programs have high potential to measure major active ingredients in solid samples.[21–24]

The aim of this study was to develop a reliable NIR spectroscopic method for monitoring the mixing phase, the first critical step within the manufacturing process of immediate release tablets containing metformin hydrochloride as the active substance. The main goal of this work was to introduce this non-destructive method for the routine monitoring of the tablet production process based on the established correlations with the classic analytical technique commonly used for this purpose.

EXPERIMENTAL

Materials

The following substances were used for the preparation of the blend mixture: metformin hydrochloride (Harman Finochem LTD, India) and poly(vinyl pyrrolidone) (PVP, Kollidon® 25, BASF, Germany).

Methods

NIR spectroscopy. The NIR diffuse reflectance spectra were obtained using a Thermo--Nicolet Antaris instrument with an integrating sphere module and an InGaAs detector. The spectra were recorded in the range from 10000 to 4000 cm^{-1} with an 8-cm^{-1} resolution, 16 scans and a one-minute collection time of.

In order to develop a calibration model for the uniformity of blend prediction, a series of calibration samples was prepared (Table I). Each mixture was measured three times and 48 calibration spectra were recorded. NIR spectra of pure metformin hydrochloride and PVP were also measured.

TABLE I. The composition of mixtures used for the development of a calibration model

Metformin hydrochloride content, mass %	PVP content, mass %
70.00	30.00
75.00	25.00
85.00	15.00
87.00	13.00
88.00	12.00
89.00	11.00
90.00	10.00
91.00	9.00
92.00	8.00
93.00	7.00
94.00	6.00
95.00	5.00
96.00	4.00
97.00	3.00
98.00	2.00
99.00	1.00
100.00	0.00

The effectiveness of the calibration model was evaluated by three independent validation blends (Table II).

TABLE II. The composition of the mixtures used for validation

Sample no.	Metformin hydrochloride content, mass %	PVP content, mass %
1	85.00	15.00
2	90.00	10.00
3	95.00	5.00

The reference (HPLC) method. The content of metformin hydrochloride in the samples was determined by a validated HPLC method, using a liquid chromatograph HP 1100 with a

UV/Vis detector (Agilent 1100 HPLC, USA). Separation was achieved on the Kinetex column (100 mm×4.6 mm, 2.6 μm). The following parameters were used for the analysis: injection volume 20 μl, flow rate 1.5 ml min^{-1}, detection wavelength 200 nm, with a mobile phase containing 0.09 % (*w*/*V*) sodium hexanesulfonate, 5 vol. % acetonitrile and 95 vol. % dilute phosphoric acid (0.1 mass %). HPLC-grade water was used as the solvent. The precision and accuracy of the method were determined. The relative standard deviation (*RSD*) of the results for the six simultaneously prepared samples was 0.23 %, the mean value for the recovery of nine prepared samples was 99.79 % and standard deviation (*SD*) was 1.73 %.

Data analysis

Quantitative calibration models were built with partial least squares (PLS) regression using the least squares algorithm. The goal of PLS regression is to establish a linear relationship between the two matrices, spectral data (*X*) and reference values (*Y*). Both *X* and *Y* were modeled in order to determine the variables in the *X* matrix that would best describe the *Y* matrix.[25] The objectives were to model the *X*- and *Y*-matrix first, and then to predict *Y* from *X* according to the equations:

$$X = 1\overline{x}' 2 + TP' + E \quad (1)$$

$$Y = 1\overline{y}' + UC' + F = 1\overline{y}' + TC' + G \quad (2)$$

where $1\overline{x}'$ and $1\overline{y}'$ represent the variable averages and originate from the preprocessing step. The information related to the observations was assumed in the scores-matrices *T* and *U*. The information related to the variables is stored in the *X*-loading matrix *P*′ and the *Y*-loadings matrix *C*′. The variation in the data was neglected in the modeling from the *E* and *F* residual matrices.

The PLS regression method was applied by using the TQ Analyst software package (Thermo Nicolet, USA). The quality of the models was assessed in terms of the root mean square error of the calibration (Eq. (3), *RMSEC*):

$$RMSEC = \sqrt{\sum_{i=1}^{N} \frac{\left(\hat{Y}_i - Y_{i,iz}\right)^2}{N}} \quad (3)$$

where $Y_{i,iz}$ is the measured parameter, $\hat{Y}_i$ is the predicted parameter and N is the number of samples for the data set under consideration.

During the calibration step, full cross validation (leave-one-out) was applied to the calibration data set and the root mean square error of the cross validation (*RMSECV*) was obtained for the calibration model (Eq. (4)):

$$RMSECV = \sqrt{\sum_{i=1}^{N} \frac{\left(\hat{Y}_{i,\mathrm{val}} - Y_{\mathrm{val}}\right)^2}{N}} \quad (4)$$

In order to determine the number of principal components, the *PRESS* function was used:

$$PRESS = \sum_{i=1}^{N} \left(\hat{Y}_i - Y_{i,\mathrm{iz}}\right)^2 \quad (5)$$

Root mean square error of prediction (*RMSEP*) can be used for an estimation of the prediction accuracy of the statistical model and can predict *Y* for a new *X*:

$$RMSEP = \sqrt{\sum_{i=1}^{N} \frac{\left(\hat{Y}_{i,\mathrm{val}} - Y_{\mathrm{val}}\right)^2}{N}} \quad (6)$$

where $Y_{i,\mathrm{iz}}$ is the measured parameter, $\hat{Y}_i$ is the predicted parameter, and N is the number of samples for the validation data set.

This parameter defines the contribution of each new introduced principal component to the definition of the dimensions of the statistical model.

Preparation of the blend mixture in production

The blend mixture was prepared by the initial feeding and mixing of metformin hydrochloride and PVP (in the mass ratio 90:10) in a vacuum processor (Roto Cube 600, IMA, Italy) at a mixer speed of 100 rpm and a chopper speed of 700 rpm. The samples were taken from the top, middle and bottom (6×2 g) of the mixer after 5, 10 and 15 min of mixing in order to determine the endpoint when the blend homogeneity was achieved.

RESULTS AND DISCUSSION

Representative NIR spectra of pure metformin hydrochloride, PVP and their blends are shown in Fig. 1.

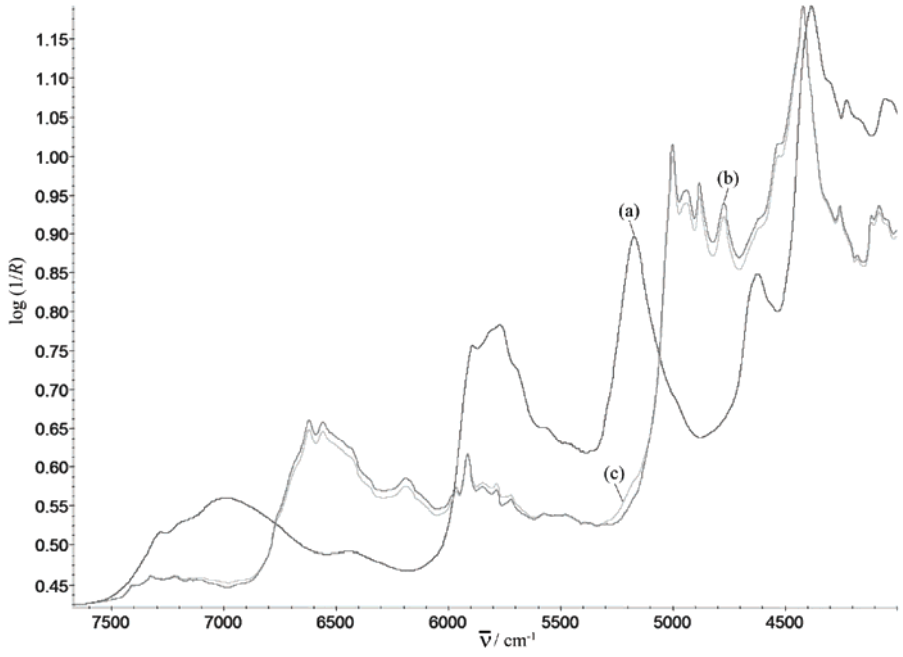

Fig. 1. NIR spectra of: a) PVP, b) metformin hydrochloride and c) mixture of metformin hydrochloride and PVP (mass ratio 90:10).

The NIR spectra of the investigated powder blends indicated that the absorption bands the amino and imido groups of metformin hydrochloride, with peak maxima around 4761, 5924, 6570 and 9600 cm^{-1} (overtones), were associated

with C–H, O–H and C–O combination bands and overtones of PVP, with peak maxima at around 5880 and 4545 cm^{-1}, which are in accordance with the results of Habib and Kamel[26] and Rantanen *et al.*[5]

The spectral range and the number of PLS factors are the two most crucial parameters in the PLS regression process.[27,28] Based on the absorption features observed in the NIR spectra, the two spectral ranges chosen to establish the calibration model were: 5980–5650 cm^{-1} and 5200–4935 cm^{-1}.

The peak maxima in the first region are related to metformin hydrochloride imido groups. The absorbance peak of PVP that appears in the second region enables the creation of the characteristic model for determining the amount of the polymer present in the mixture. The spectra of seventeen calibration samples containing different ratios of the studied components are shown in Fig. 2. Based on the obtained results, it could be seen that the peaks were shifted due to the variations in the composition of the calibration mixture.

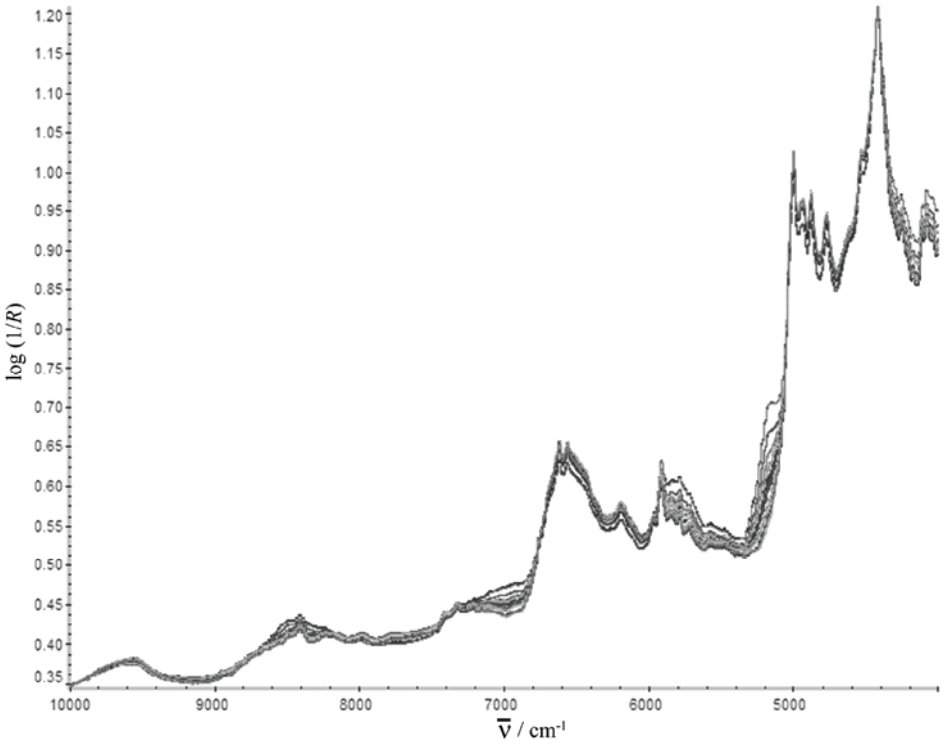

Fig. 2. NIR spectra of the calibration samples.

The calibration and cross-validation regression parameters and the numbers of the principal components in the PLS method, without data pre-treatment, are given in Table III.

TABLE III. PLS calibration models used for the determination of blend uniformity; MTH = = metformin hydrochloride

Parameter	Calibration data set
Number of samples	54
Number of mixtures	16
MTH content in the validation blends (minimal), mass %	69.54
MTH content in the validation blends (maximal), mass %	99.89
Model type	Full spectrum PLS regression
Spectral range, cm^{-1}	5980–5650 and 5200–4935
Number of latent variables	4
Coefficient of correlation	0.9981
RMSEC	0.4810
Coefficient of correlation for cross-validation	0.9956
RMSECV	0.7370

The coefficient of correlation was higher than 0.995, indicating that the established model, with four PLS components, was linear. The lower coefficient of correlation for cross-validation could be attributed to the estimated limit values (mixture of 30 and 70 mass % of PVP and metformin hydrochloride, respectively). The value of this mixture was estimated from the model that was formed over the other sample calibration spectra. In this case, the probability that the linearity of the model was lower is increased, resulting in the consequential increase of the difference between the estimated and actual values, which ultimately results in a slightly lower correlation coefficient.

The results predicted by the NIR method and then checked by the HPLC method for the validation blends are given in Table IV.

TABLE IV. Accuracy and precision of the developed model; number of samples: 6

Parameter	Validation mixture					
	1		2		3	
	Predicted	Measured	Predicted	Measured	Predicted	Measured
Metformin	86.43	84.98	90.05	90.05	95.55	94.97
hydrochloride	86.21	85.12	89.76	89.76	95.23	95.43
content, mass %	85.21	84.96	89.64	89.64	96.02	95.03
	84.22	84.98	90.75	90.75	94.79	94.91
	84.12	85.10	90.53	90.53	94.61	95.28
	84.39	84.94	89.89	89.89	95.11	95.36
Average value, %	85.10	85.01	90.10	90.10	95.22	95.16
SD	1.02	0.08	0.44	0.44	0.51	0.22
RSD	1.20	0.09	0.49	0.49	0.54	0.23
RMSEP	0.930		0.698		0.560	

For the validation mixtures, the calculated recovery values were within the range from 97 to 103 %, *i.e.*, the value was 100.15 % for all the tested samples. The *RSD* and *RMSEP* values of the calibration model were 2 and 1 % lower,

respectively (Table IV). A paired *t*-test statistical comparison at the 95 % confidence level indicated no differences between the results obtained with the two methods. The accuracy and precision of the calibration model were proven based on the obtained results.

The estimated calibration NIR model and HPLC method were used to measure the amount of metformin hydrochloride in the mixture produced in the vacuum processor (production batch). Comparative data obtained by NIR and HPLC analysis are given in Table V.

TABLE V. Comparative results obtained by NIR and HPLC

Mixing time, min	Sampling points in the vacuum processor	Content of metformin hydrochloride in the powder blend mixture, mass %		Difference between the two methods, %
		NIR	HPLC	
5	Top	102.14	99.42	2.72
	Middle	102.19	100.97	1.22
	Bottom	100.27	99.99	0.28
10	Top	101.50	102.13	–0.63
	Middle	101.01	101.93	–0.92
	Bottom	99.31	99.34	–0.03
15	Top	101.01	100.37	0.64
	Middle	100.17	100.38	–0.21
	Bottom	100.56	100.82	–0.27

Based on the obtained data, it could be seen that a homogenous mixture, with a drug content within the range from 95 to 105 % of the theoretical value, was obtained after five minutes of mixing. The difference between the two tested methods for the first set of samples was slightly higher than those for the other two (the samples taken after 10 and 15 min of mixing). This could be attributed to higher sensitivity of the NIR method due to the amount of sample that was exposed to the radiation during spectra collection, which was tens of times higher compared to the amount of sample that was dissolved for the HPLC analysis (*ca*. 30 mg). After the second and the third sampling, the differences between the two methods were lower, which is further confirmation that the calibration model created for a metformin hydrochloride concentration range between 70 and 100 mass % will give reliable results in the analysis of metformin hydrochloride – PVP mixtures.

With regard to defining the final time point of mixing, it could be concluded that homogeneity was achieved after five minutes, which was expected since blending was conducted in a vacuum processor at high mixer and chopper rotation speeds, which enabled homogeneous distributions of the active ingredient to be obtained.

CONCLUSIONS

An NIR spectroscopic method with chemometric analysis was created using the PLS regression model in order to determine the homogeneity of powder mixtures. The calculated results agreed well with those obtained by the HPLC reference analytical method. As a rapid and non-invasive technique, the NIR method reduces sampling errors and provides the possibility of end-point determination, leading to a potentially significant improvement over the conventional analytical methods. Additional work on the implementation of the NIR method in the other phases of tablet production of metformin hydrochloride (granulation, compression) should be realized in order to assure its application for monitoring the entire manufacturing process.

Acknowledgments. This work was financially supported by the Ministry of Education, Science and Technological Development of the Republic of Serbia (Projects No. 172013 and TR 34007).

И З В О Д

ПРИМЕНА NIR СПЕКТРОСКОПИЈЕ ЗА ПРАЋЕЊЕ ПРОЦЕСА МЕШАЊА ПРАШКОВА

ЉИЉАНА Б. МАРИЋ[1], БРАНИСЛАВ Д. ЈОВИЋ[2], СЛОБОДАН Д. ПЕТРОВИЋ[3], АЛЕКСАНДАР М. НИКОЛИЋ[2] и ИРЕНА Ј. ХОМШЕК[1]

[1]Галеника ад, Батајнички друм бб, 11080 Београд, [2]Природно–математички факултет, Универзитет у Новом Саду, 21000 Нови Сад и [3]Технолошко–металуршки факултет, Универзитет у Београду, 11000 Београд

У раду је приказана примена NIR спектроскопије као средства за праћење процеса мешања метформин-хидрохлорида и поливинилпиролидона (PVP) који представља прву фазу у производњи таблета. Хомогеност мешавине тестирана је применом неинвазивне NIR спектроскопије, а за анализу добијених резултата коришћен је регресиони модел најмањих квадрата (PLS). Истовремено је критичан параметар (садржај метформин-хидрохлорида) праћен класичном аналитичком техником која се уобичајено користи у ове сврхе. На основу високе селективности модела развијеног у овој студији, као и успостављеној корелацији између резултата добијених различитим методама, може се закључити да предложена брза и неинвазивна техника може бити ефикасан алат за праћење једне од најкритичнијих производних фаза у изради чврстих дозираних облика.

(Примљено 1. априла, ревидирано 14. јула 2013)

REFERENCES

1. FDA, *PAT Guidance for Industry – A Framework for Innovative Pharmaceutical Development, Manufacturing and Quality Assurance*, Rockville, MD, 2004
2. J. Workman, L. Weyer, *Practical Guide to Interpretive Near-Infrared Spectroscopy*, CRS Press, Taylor & Francis Group, Boca Raton, FL, 2008, p. 108
3. G. Reich, *Adv. Drug Deliv. Rev.* **57** (2005) 1109
4. N. K. Shah, P. J. Gemperline, *Anal. Chem.* **62** (1990) 465
5. J. Rantanen, O. Antikainen, J.-P. Mannemiaa, J. Yliiuusi, *Pharm. Dev. Technol*. **5** (2000) 209

6. J. Rantanen, E. Räsänen, O. Antikainen, J. P. Mannermaa, J. Yliruusi, *Chemom. Intell. Lab. Syst*. **56** (2001) 51
7. I. Tomuta, R. Iovanov, A. L. Vonica, S. E. Leucuta, *Sci. Pharm*. **79** (2011) 885
8. P. Chalusa, Y. Roggo, S. Walters, M. Ulmschneider, *Talanta* **66** (2005) 1294
9. S. S. Sekulić, J. Wakeman, P. Doherty, P. A. Hailey, *J. Pharm. Biomed. Anal*. **17** (1998) 1285
10. V. J. Bijlani, M. Delado-Lopez, C. M. Adeyeye, J. K. Drennen, *NIR News* **13** (2002) 8
11. K. R. Morris, J. G. Stowell, S. R. Byra, A. W. Placette, T. D. Davis, G. E. Peck, *Drug Dev. Ind. Pharm.* **26** (2000) 985
12. E. W. Ciurczak, K. James, I. Drennen, *Pharmaceutical and Medical Applications of Near-Infrared Spectroscopy*, Marcel Dekker, New York, 2002, p. 38
13. G. Van Vaerenbergh, *Pharm. Technol. Eur*. **23** (2011) 7
14. M. Kar, P. K. Choudhury, *Indian J. Pharm. Sci.* **71** (2009) 318
15. V. Porta, S. G. Schramm, E. K. Kano, E. E. Koono, Y. P. Armando, K. Fukuda, C. H. dos Reis Serra, *J. Pharm. Biomed. Anal.* **46** (2008) 143
16. R. Huupponen, P. Ojala-Karlsson, J. Rouru, M. Koulu, *J. Chromatogr*. **583** (1992) 270
17. R. Q. Gabr, R. S. Padwal, D. R. Brocks, *J. Pharm. Pharmaceut. Sci.* **13** (2010) 486
18. R. T. Sane, V. J. Banavalikar, V. R. Bhate, V. G. Nayak, *Indian Drugs* **26** (1989) 647
19. S. Z. El-Khateeb, H. N. Assaad, M. G. El-Bardicy, A. S. Ahmad, *Anal. Chim. Acta* **208** (1988) 321
20. M. G. El-Bardicy, S. Z. El-Khateeb, A. K. S. Ahmad, H. N. Assaad, *Spectrosc. Lett*. **22** (1989) 1173
21. C. Ufret, K. Morris, *Drug Dev. Ind. Pharm*. **27** (2001) 719
22. M. Otsuka, F. Kato, Y. Matsuda, *Analyst* **126** (2001) 1578
23. N. Smola, U. Urleb, *Anal. Chim. Acta* **410** (2000) 203
24. K. M. Morisseau, C. T. Rhodes, *Drug Dev. Ind. Pharm*. **21** (1995) 1071
25. M. J. Adams, *Chemometrics in Analytical Spectroscopy*, Royal Society of Chemistry, Cambridge, 1995, p. 30
26. I. Habib, M. S. Kamel, *Talanta* **60** (2003) 185
27. G. X. Zhou, P. A. Hines, K. C. White, M. W. Borer, *Anal. Chem*. **70** (1998) 390
28. K. H. Beebe, B. R. Kowalski, *Anal. Chem*. **59** (1987) 1007A.

Journal of the Serbian Chemical Society
JSCS-info@shd.org.rs • www.shd.org.rs/JSCS
J. Serb. Chem. Soc. *79* (3) 341–344 (2014) UDC 66.021.2.063.8+532.13+547.1:53.072
JSCS–4589 *Note*

NOTE

Liquid mixture viscosities correlation with rational models

ANĐELA B. KNEŽEVIĆ-STEVANOVIĆ[1], GORAN M. BABIĆ[2], MIRJANA Lj. KIJEVČANIN[2#], SLOBODAN P. ŠERBANOVIĆ[2#] and DUŠAN K. GROZDANIĆ[2*]

[1]*Metro Vancouver, 4330 Kingsway, Burnaby, British Columbia, V5H 4G8, Canada and* [2]*Chemical Engineering Department, Faculty of Technology and Metallurgy, University of Belgrade, Karnegijeva 4, 11000 Belgrade, Serbia*

(Received 10 June, revised 27 August 2013)

Abstract: In this paper, twenty two selected rational correlation models for the viscosities of liquid mixtures of organic compounds were tested on 219 binary sets of experimental data taken from the literature. The binary sets contained 3675 experimental data points for 70 different compounds. The Dimitrov–Kamenski X, Dimitrov–Kamenski XII, and Dimitrov–Kamenski XIII models demonstrated the best correlative characteristics for binary mixtures with an overall absolute average deviation of less than 2 %.

Keywords: binary mixture; liquid mixture viscosity; rational correlation models.

INTRODUCTION

The study of the thermodynamic properties of liquid mixtures contributes to an understanding of the behaviour of various liquids and functional groups. This information is very useful in the design of industrial processes, and in the development of the liquid state theories and predictive methods. Knowledge of the viscosities of liquid mixtures is required for the solution of many engineering problems, including heat and mass transfer, and fluid flow.

A number of correlation models have been developed for the viscosities of liquid mixtures. Some of these models are linear or can be linearized per parameters, and others are non-linear. In a previous article, the former were tested on experimental viscosities of liquid mixtures of alkanes, haloalkanes, alcohols, aromatics, amines, ketones, *etc*.[1] Rational models are non-linear per parameters, but these models have the number one as the first term in denominator polynomial, which enables the use of the linear least squares method in correlation. For many

* Corresponding author. E-mail: dule@tmf.bg.ac.rs
# Serbian Chemical Society member.
doi: 10.2298/JSC130610114K

experimental data sets,[1] models with a rational form resulted in an average error of about 1 %. However, in some instances, the denominator had a very small value resulting in very large percent and average percent errors, making models with a rational form unreliable. This difficulty may be overcome if nonlinear least squares methods Gauss,[2] Levenberg,[3] Marquardt,[4] Law–Bailey,[5] *etc*. are used. In addition, the Hooke–Jeeves,[6] Fletcher–Powell,[7] Nelder–Mead,[8] *etc*. optimization methods can also be used. Selection of the first assumptions for the parameters is critical for successful use of these methods. On the other hand, rational models have many minimums in the parametric area. These problems may be avoided if a global optimizing method, such as the Monte Carlo method, is used. In this article, the linear congruental pseudo-random number generator was used.[9]

The objective function used in the correlation was:

$$OF = \left[\sum_{i=1}^{n} \left(\eta_{\mathrm{lm},i,\mathrm{exp}} - \eta_{\mathrm{lm},i,\mathrm{cal}} \right)^2 / \left(n - np \right) \right]^{1/2} \rightarrow \min \qquad (1)$$

where η_{lm} is the viscosity of a liquid mixture, n is the number of experimental data points per set and np is the number of parameters.

The performance of selected rational models[1] was tested on 219 binary sets of literature experimental data with 3675 experimental data points for 70 different compounds. The selected binary liquid mixtures were presented in a previous article.[1] A deviation from the experimental values is expressed as the absolute average deviation, p_{av}, for each data set point:

$$p_{\mathrm{av}} = (100 / n) \sum_{i=1}^{n} \left| (\eta_{\mathrm{lm},i,\mathrm{exp}} - \eta_{\mathrm{lm},i,\mathrm{cal}}) / \eta_{\mathrm{lm},i,\mathrm{exp}} \right| \qquad (2)$$

The overall absolute average deviation, P_{av}, for each model is defined as:

$$P_{\mathrm{av}} = \sum_{i=1}^{N} n_i \, p_{\mathrm{av},i} / \sum_{i=1}^{N} n_i \qquad (3)$$

where N is the number of data sets.

RESULTS AND DISCUSSION

Results are presented in Table I, where N_{all} is the total number of data points in the correlation. Only sets of experimental data with $n \geq N_{\mathrm{m}} + 2$ were used in the correlation, where N_{m} is number of model parameters. Sets with experimental data at different temperatures and pressures were correlated with only one set of parameters. The results for linear models reported in a previous article[1] are also presented in Table I. The number of experimental data used in the correlations depended on the number of model parameters and on the existence of experi-

mental data for density. The results presented in Table I indicate that the Dimitrov–Kamenski X, the Dimitrov–Kamenski XII and the Dimitrov–Kamenski XIII, with overall absolute average deviations of 1.74, 1.32 and 1.18 %, respectively, have the best correlation ability of all the considered rational models. These results are slightly better than the results obtained for the linear models (Heric I, Heric–Brewer II and Krishnan–Laddha, with overall absolute average deviations of 1.73 %, 1.23 and 1.76 %, respectively).

TABLE I. Results of viscosity correlation

Entry no.	Correlation model	N_m	P_{av} / %	N_{all}
1	Dolezalek–Schulze	1	6.83	3675
2	Grunberg–Nissan	1	3.37	3675
3	Tamura–Kurata	1	5.14	3360
4	McAllister 3	2	5.29	3264
5	McAllister 4	3	6.07	3249
6	Katti–Chaudri	1	2.45	3264
7	Heric I	2	1.73	3264
8	Heric–Brewer I	3	8.21	3660
9	Heric–Brewer II	3	1.23	3249
10	Krishnan–Laddha	2	1.76	3264
11	McAllister–Soliman–Marschall	2	5.31	3264
12	Mehrotra	1	2.98	3675
13	Baylaucq–Daugé–Boned	3	4.30	486
14	Dimitrov–Kamenski I	2	7.80	3675
15	Dimitrov–Kamenski II	4	6.01	2212
16	Dimitrov–Kamenski III	4	7.69	3576
17	Dimitrov–Kamenski IV	2	2.60	3675
18	Dimitrov–Kamenski V	4	2.58	2212
19	Dimitrov–Kamenski VI	2	2.80	3675
20	Dimitrov–Kamenski VII	6	4.41	2212
21	Dimitrov–Kamenski VIII	3	2.19	3660
22	Dimitrov–Kamenski IX	4	2.05	2212
23	Dimitrov–Kamenski X	2	1.74	3675
24	Dimitrov–Kamenski XI	3	1.88	2212
25	Dimitrov–Kamenski XII	3	1.32	3660
26	Dimitrov–Kamenski XIII	5	1.18	2212
27	Focke–Du Plessis I	4	7.82	3576
28	Focke–Du Plessis II	5	7.86	3401
29	Focke–Du Plessis III	6	6.73	3375
30	Focke–Du Plessis IV	4	7.98	3576
31	Focke–Du Plessis V	5	7.47	3401
32	Focke–Du Plessis VI	6	7.42	3393
33	Focke–Du Plessis VII	5	8.01	3401
34	Focke–Du Plessis VIII	6	8.63	3393
35	Focke–Du Plessis IX	7	7.50	3357

CONCLUSIONS

Selected rational correlation models were tested on 219 binary mixtures with 3675 experimental data points. The Dimitrov–Kamenski X, the Dimitrov––Kamenski XII and the Dimitrov–Kamenski XIII models have the best correlative characteristics for binary mixtures with overall absolute average deviations of less then 2 %.

Acknowledgements. This work was supported by a grant from the Research Fund of the Republic of Serbia (Project No. 172063) and the Faculty of Technology and Metallurgy, University of Belgrade.

И З В О Д

КОРЕЛИСАЊЕ ВИСКОЗИТЕТА ТЕЧНИХ СМЕША ПОМОЋУ РАЦИОНАЛНИХ МОДЕЛА

АНЂЕЛА Б. КНЕЖЕВИЋ-СТЕВАНОВИЋ[1], ГОРАН М. БАБИЋ[2], МИРЈАНА Љ. КИЈЕВЧАНИН[2], СЛОБОДАН П. ШЕРБАНОВИЋ[2] и ДУШАН К. ГРОЗДАНИЋ[2]

[1]*Metro Vancouver, 4330 Kingsway, Burnaby, British Columbia, V5H 4G8, Canada и* [2]*Технолошко–металуршки факултет, Универзитет у Београду, Карнегијева 4, 11000 Београд*

У овом раду тестирана су 22 одабрана рационална модела за корелисање вискозитета течних смеша на литературним експерименталним подацима за 219 бинарних смеша са 3675 експерименталних података за 70 различитих супстанци. Dimitrov–Kamenski X, Dimitrov–Kamenski XII и Dimitrov–Kamenski XIII модели показали су најбоље корелациона својства са укупном средњом процентуалном грешком мањом од 2 %.

(Примљено 10. јуна, ревидирано 27. августа 2013)

REFERENCES

1. A. B. Knežević-Stevanović, G. M. Babić, M. Lj. Kijevčanin, S. P. Šerbanović, D. K. Grozdanić, *J. Serb. Chem. Soc*. **77** (2012) 1083
2. D. K. Grozdanić, *Numerical methods*, Akademska misao, Belgrade, 2008 (in Serbian)
3. K. Levenberg, *Quart. Appl. Math.* **2** (1944) 164
4. D. W. Marquardt, *J. Soc. Ind. Appl. Math*. **11** (1963) 431
5. V. J. Law, R. V. Bailey, *Chem. Eng. Sci.* **18** (1963) 189
6. R. Hooke, T. A. Jeeves, *J. Assoc. Comp. Mach.* **8** (1961) 212
7. R. Fletcher, M. J. D. Powell, *Computer J.* **6** (1963) 1963
8. J. A. Nelder, R. Mead, *Computer J.* **7** (1964) 308
9. D. K. Grozdanić, A. B. Knežević-Stevanović, B. D. Đorđević, A. Ž. Tasić, S. P. Šerbanović, *J. Serb. Chem. Soc.* **61** (1996) 513.

Journal of the Serbian Chemical Society
JSCS-info@shd.org.rs • www.shd.org.rs/JSCS
J. Serb. Chem. Soc. 79 (3) 345–359 (2014)
JSCS–4590
UDC 546.42'226+546.42'264+547.288.1:
661.566.097.3:544.4
Original scientific paper

Kinetics of conversion of celestite to strontium carbonate in solutions containing carbonate, bicarbonate and ammonium ions, and dissolved ammonia

MERT ZORAGA and CEM KAHRUMAN*

Istanbul University, Engineering Faculty, Metallurgical and Materials Engineering Department, 34320, Avcilar, Istanbul, Turkey

(Received 7 March, revised 21 May 2013)

Abstract: Celestite concentrate ($SrSO_4$) was converted to $SrCO_3$ in solutions containing CO_3^{2-}, HCO_3^- and NH_4^+ and dissolved ammonia. The effects of stirring speed, CO_3^{2-} concentration; temperature and particle size of $SrSO_4$ on the reaction rate were investigated. It was found that the conversion of $SrSO_4$ was increased by increasing the temperature and decreasing the particle size, while the reaction rate was decreased with increasing the CO_3^{2-} concentration. However, the stirring speed had no effect on the reaction rate. The conversion reaction was under chemical reaction control and the shrinking core model was suitable to explain the reaction kinetics. The apparent activation energy for the conversion reaction was found to be 41.9 kJ mol^{-1}. The amounts of the elements in the reaction solution were determined quantitatively by inductively coupled plasma-optical emission spectrometry. The characterization of the solid reactant and product was made using the scanning electron microscopy-energy dispersive spectrometry and X-ray powder diffraction analytical techniques.

Keywords: celestite; strontium sulfate; strontium carbonate; conversion; kinetics.

INTRODUCTION

Celestite mineral is the main source of Sr metal and other Sr compounds. These are commonly used in a wide range of industrial applications, such as the production of ferrite magnets, pigments, special glasses, zinc refining and pyrotechnics, *etc*. The most important chemical compound of Sr is $SrCO_3$.

Typically, two methods are commonly used for the conversion of $SrSO_4$ to $SrCO_3$. In the first method (black ash method), $SrSO_4$ is reduced with coal in a furnace at temperatures between 1273 and 1473 K to produce soluble sulfide, which is then leached with water and the strontium-containing solution is reacted

* Corresponding author. E-mail: cemcemce@istanbul.edu.tr
doi: 10.2298/JSC130307066Z

with either CO_2 or Na_2CO_3 to precipitate $SrCO_3$.[1–3] However, this conventional process has high energy consumption and produces undesirable pollutants.[4,5] In the second method (direct conversion method), the conversion is maintained through the use of Na_2CO_3 or other carbonate sources.[2,3,6]

The conversion of $SrSO_4$ to $SrCO_3$ in alkali carbonate solution was studied by Kobe and Deiglmeir and it was found that 98.8 % conversion was obtained at 368 K after 2 h.[2] De Buda applied a two-staged purification process to obtain $SrCO_3$. Initially, HCl solution was used to extract impurities. Then, $(NH_4)_2CO_3$ solution was used to obtain $SrCO_3$.[7]

Kocakusak *et al.* used a $(NH_4)_2CO_3$ solution to convert $SrSO_4$ to $SrCO_3$. $SrCO_3$ was separated by filtration.[8] The filtrate consisted of $(NH_4)_2CO_3$ and $(NH_4)_2SO_4$. The $(NH_4)_2CO_3$ present in the solution was decomposed to NH_3 and CO_2 by heating the solution up to 353–373 K. The remaining solution was mixed with $Ca(OH)_2$ to precipitate $CaSO_4$. An ammoniacal solution was obtained by separating $CaSO_4$ by filtration. NH_3 and CO_2 obtained in the previous step was passed through this ammoniacal solution to obtain $(NH_4)_2CO_3$. This process has a significant economical importance in the industrial application of $(NH_4)_2CO_3$ solution as a reactant.

Erdemoglu and Canbazoglu[1] and Owusu and Litz[3] studied the leaching of SrS in water. Erdemoglu *et al.* investigated the leaching of celestite mineral in sodium Na_2S solution to obtain a Sr compound at constant temperature and determined the rate of conversion, which mainly depended on the Na_2S concentration. They concluded that the leaching of $SrSO_4$ in Na_2S solution was possible but slow.[9]

Aydogan *et al.* explained the dissolution kinetics of $SrSO_4$ in HCl solution containing $BaCl_2$ to produce $SrCl_2$. They claimed that the dissolution reaction of $SrSO_4$ was under chemical reaction control.[10]

Iwai and Toguri studied the conversion of $SrSO_4$ in Na_2CO_3 solution both from thermodynamic and kinetic points of view.[5] Castillejos *et al.* studied the conversion of $SrSO_4$ in Na_2CO_3 aqueous solution.[6] Erdemoglu *et al.*, Obut *et al.* and Setoudeh *et al.* investigated the direct mechano-chemical conversion of $SrSO_4$ to $SrCO_3$ using a ball mill.[11–13] Suarez-Orduna *et al.* and Ni *et al.* studied the conversion of $SrSO_4$ to $SrCO_3$ under hydrothermal conditions in Na_2CO_3 and hexamethylenetetramine solutions, respectively.[14,15] Bingöl *et al.* applied the neural model for the conversion of $SrSO_4$ in Na_2CO_3 solution and an extended delta–bar–delta algorithm.[16] In other studies by Bingöl *et al.*[17,18], the conversion of celestite with $(NH_4)_2CO_3$ to strontium carbonate were investigated using dry and wet mechano-chemical treatment in a planetary mill

The next step in the production of strontium metal are the calcinations of $SrCO_3$. These are typically performed by aluminothermic reduction followed by strontium evolution under vacuum.[19]

In this study, solutions containing CO_3^{2-}, HCO_3^- and NH_4^+ and dissolved NH_3 were used to determine the effects of stirring speed, particle size of $SrSO_4$, CO_3^{2-} concentration and temperature on the conversion of high-grade celestite mineral to $SrCO_3$. A kinetic model equation was derived, which showed the relationship between the fractional conversion of $SrSO_4$ (X) with time (t) and particle size (R).

EXPERIMENTAL

Celestite concentrate

The celestite concentrate used in this study was provided by Barit Maden Turk A.S., Turkey. The quantitative chemical composition of the celestite concentrate, determined by X-ray fluorescence spectroscopy (XRF) analysis, is given in Table I. The mineral consisted of 96.79 mass % $SrSO_4$. The celestite concentrate was subjected to particle size distribution using the standard test sieves by the wet sieve equipment Octagon 200.

TABLE I. Composition of celestite concentrate

Compound	$SrSO_4$	$CaSO_4$	$BaSO_4$	SiO_2	Fe_2O_3
Content, mass %	96.79	2.04	0.57	0.46	0.14

Preparation of the solution containing CO_3^{2-}, HCO_3^-, NH_4^+ and dissolved NH_3

The commercially available $(NH_4)_2CO_3$ was in the form of a mixture of ammonium carbamate ($H_4NOCONH_2$) and ammonium bicarbonate ($H_4NOCOOH$) in a mole ratio of 1:1 (Merck, 1.59504.1000) (AC). Different amounts of this substance were dissolved in distilled water to obtain solutions that contained CO_3^{2-}, HCO_3^{-1}, NH_4^+ and dissolved NH_3, which were used in the conversion reactions.

Volumetric analysis

The concentrations of CO_3^{2-}, HCO_3^- and of NH_3 dissolved in the solutions were determined quantitatively by volumetric analyses by titrating with a definite volume of solution of HCl titrisol solution (Merck), using first phenolphthalein and then methyl orange as the indicator.

Experimental procedure

The experiments were performed using the set-up illustrated in Fig. 1-S of the Supplementary material to this paper. A detailed explanation of the employed set-up was described by Kalpakli *et al.*[20] For the determination of the amounts of the elements dissolved in the solution, a definite volume of solution was taken from the reactor at definite time intervals during the reaction. The same amount of fresh AC solution was added to the reactor after each sampling. In this way, the concentrations of CO_3^{2-}, HCO_3^{-1}, NH_4^+ and dissolved NH_3 and the total volume of the reaction mixture were kept constant during the experiments. The quantitative analysis of the elements in the solution was realized using inductively coupled plasma-optical emission spectrometry (ICP-OES, Spectro Ciros Vision).

Materials characterization

For the characterization of the solid reactant (celestite concentrate, $SrSO_4$) and solid product ($SrCO_3$) obtained at the end of each experiment, X-ray powder diffraction analysis (XRD, Rigaku D/Max-2200/PC, CuK_α (1.54056 Å) and scanning electron microscopy–energy

dispersive spectroscopy (SEM–EDS, Jeol JSM 5600- i-XRF 500i) analytical techniques were used.

RESULTS AND DISCUSSION

The dissolution of AC in pure water

During the dissolution of AC in pure water, dissolution (Reaction (1)) and hydrolysis (Reaction (2)) reactions occur simultaneously:

$$H_4NOCOOH(s) \rightarrow HCO_3^-(aq) + NH_4^+(aq) \quad (1)$$

$$H_4NOCONH_2(s) \rightarrow CO_3^{2-}(aq) + 2\ NH_4^+(aq) \quad (2)$$

The HCO_3^- and NH_4^+ that were formed according to Reactions (1) and (2) are hydrolyzed rapidly as shown in Reactions (3) and (4). For simplicity, H_3O^+ is written as H^+:

$$NH_4^+(aq) \rightleftarrows NH_3(l) + H^+(aq) \quad (3)$$

$$HCO_3^-(aq) \rightleftarrows CO_3^{2-}(aq) + H^+(aq) \quad (4)$$

The H^+ that are formed in Reaction (3) are consumed by CO_3^{2-} in the reverse Reaction (4), and thus the equilibrium reaction (Reaction (5)) is effective:

$$CO_3^{2-}(aq) + NH_4^+(aq) \rightleftarrows NH_3(l) + HCO_3^-(aq) \quad (5)$$

The dependency of the acid dissociation constants (K_3 and K_4) of Reactions (3) and (4) with temperature are given by Eqs. (6) and (7).[21,22] In these equations, T is the absolute temperature and pK is defined as –log K.

$$pK_3 = 0.090387 + 2729.33/T \quad (6)$$

$$pK_4 = -6.4980 + 2902.39/T + 0.02379 \quad (7)$$

The equilibrium constant of Reaction (5), K_5, was calculated using Eqs. (6) and (7) for each solution temperature applied in the experiments. The calculated values of K_5 are given in Table II. These values were used to calculate CO_3^{2-}, HCO_3^- and NH_4^+ concentrations and the molecularly dissolved NH_3 concentrations for different amounts of AC and temperature (Table III). Table III shows that at constant temperature, as the AC quantity increased, the ion concentrations in the solution increased. When the AC quantity was kept constant, the CO_3^{2-} and NH_4^+ concentrations decreased, while the molecularly dissolved NH_3 and HCO_3^- concentration increased with increasing temperature. The heat of equilibrium reaction (Reaction (5)) was calculated to be positive (endothermic reaction) by using Gibbs–Helmholtz Equation and Eqs. (6) and (7).[23] The enthalpy change of Reaction (5) were found to be 35.8, 38.5, 41.3 and 44.2 kJ mol^{-1} for 293, 303, 323 and 323 K, respectively. Since Reaction (5) was calculated to be endothermic, the reaction proceeded towards the right hand side. Thus, the CO_3^{2-} and NH_4^+ concentrations decreased with increasing temperature of the solution.

TABLE II. Equilibrium constants for Reaction (5) at different temperatures

T / K	293	303	313	323
K_5	9.391	15.529	25.751	42.813

TABLE III. Concentrations of CO_3^{2-}, HCO_3^-, NH_4^+ and NH_3 dissolved in AC aqueous solutions

T / K	AC concentration, mol dm^{-3}				
	0.5	0.75	1.00	1.25	1.50
	Concentration of CO_3^2, mol m^{-3}				
293	44	65	89	111	133
303	29	43	57	72	86
313	18	27	36	45	55
323	11	17	22	28	33
	Concentration of HCO_3^-, mol m^{-3}				
293	956	1435	1911	2389	2867
303	971	1457	1943	2428	2914
313	982	1473	1964	2455	2946
323	989	1483	1978	2472	2967
	Concentration of dissolved NH_3, mol m^{-3}				
293	456	685	911	1139	1367
303	471	707	943	1178	1414
313	482	723	964	1205	1446
323	489	733	978	1222	1467
	Concentration of NH_4^+, mol m^{-3}				
293	1044	1565	2089	2611	3133
303	1029	1543	2057	2572	3086
313	1018	1527	2036	2545	3055
323	1011	1517	2022	2528	3033

H^+ and OH^-exist in the solution together with CO_3^{2-}, HCO_3^-, NH_4^+ and molecularly dissolved NH_3. Consequently, these determine the pH of the solution. It is important to note that H^+ and OH^- concentrations were quite low with respect to the concentrations of the other ion.

The concentration values given in Table III are in good agreement with the results of volumetric analyses. The consumption of HCl titrisol solution for the change in the color of the phenolphthalein indicator was determined to be half that consumed for a change of the color of the Methyl Orange indicator. During the titration with HCl titrisol solution using the phenolphthalein indicator, CO_3^{2-} and NH_3 present in the solution are transformed to HCO_3^- and to NH_4^+, respectively. In the following step, after the addition of the methyl orange indicator, the HCO_3^- formed in the first step and the HCO_3^- already present in the solution were titrated to from H_2CO_3, which leaves the solution as CO_2 gas.

The pH values of the solutions were measured to be 8.9 at room temperature (298 K) in all the solutions obtained by dissolving different amounts of AC. The

mole ratios of HCO_3^- to $CO_3^{2-}$and NH_4^+ to NH_3 in each solution were constant for each temperature. The pH value of the solution was also calculated according to Eqs. (6) and (7) to be 8.9 again. The same calculated and measured pH values of the solution suggest that the activity coefficients of each reactant and product, which are dependent to the ionic strength of the solution, did not change the value of K_5.

The equilibrium between ammonium carbonate, ammonium bicarbonate and ammonium carbamate was investigated with Raman spectroscopy by Wen and Broker.[24] They claimed that carbamate ions (H_2NCOO^-) existed in the solution together with CO_3^{2-}, HCO_3^-, NH_3 and NH_4^+. Qin *et al*. observed that H_2NCOO^- is present in the aqueous solutions of NH_3 containing ammonium carbonate/ /ammonium bicarbonate.[25] Therefore, in this study, the prepared AC solution was held for a long period in a closed flask for the complete hydrolysis of H_2NCOO^-. The measured pH was found to be the same as the calculated one, which indicates that complete hydrolysis was achieved.

The conversion of $SrSO_4$ to $SrCO_3$

The driving force for the conversion reaction if $SrSO_4$ to $SrCO_3$ is the low solubility of $SrCO_3$ compared to $SrSO_4$ in aqueous solutions. The solubility products of $SrSO_4$ and $SrCO_3$ are 2.8×10^{-7} and 9.4×10^{-10}, respectively.[11] Thus, the solubilities of $SrSO_4$ and $SrCO_3$ in pure water were calculated to be 0.529 and 3.07×10^{-2} mol m^{-3}, respectively.

The conversion of $SrSO_4$ to $SrCO_3$ in the solutions containing CO_3^{2-}, HCO_3^-, NH_4^+ and dissolved NH_3 occurs according to:

$$SrSO_4 + CO_3^{2-} \rightarrow SrCO_3 + SO_4^{2-} \quad (8)$$

The concentration of CO_3^{2-} in the solution did not change significantly during the conversion due to the use of small amounts of celestite (0.016 mol) with respect to large concentrations of NH_3 and HCO_3^- present in the used solution. This is due to fact that during the consumption of CO_3^{2-} according to Reaction (8), CO_3^{2-} are simultaneously rapidly formed according to reverse Reaction (5). Therefore, the concentration of CO_3^{2-} did not change during the conversion reaction, which is of importance in terms of the kinetic evaluation.

The effect of stirring speed

A celestite concentrate of 0.016 mol (53–75 μm particle size, 1×10^{-3} m^3 solution, 1.5 mol of AC and 323 K) was used at 3.33, 4.17 and 5 rps to investigate the effect of stirring speed on the conversion reaction of $SrSO_4$.

The fractional conversion of $SrSO_4$ (X) at any reaction time (t) was calculated according to:

$$X = \frac{W_0 - W_t}{W_0} \tag{9}$$

where W_0 is the mass of $SrSO_4$ fed to the solution and W_t is the mass of unreacted $SrSO_4$ at any reaction time, *t*.

The *X*–*t* diagrams obtained for 3.33, 4.17 and 5 rps are illustrated in Fig. 2, from which it can be seen that increasing the stirring speed from 3.33 to 5 rps had no significant effect on the reaction rate. This case proved that the use of 5 rps. can eliminate the resistance of the liquid film surrounding the particles. Therefore, in the experiments in which the effects of the other parameters on the conversion were investigated, the stirring speed was kept constant at 5 rps.

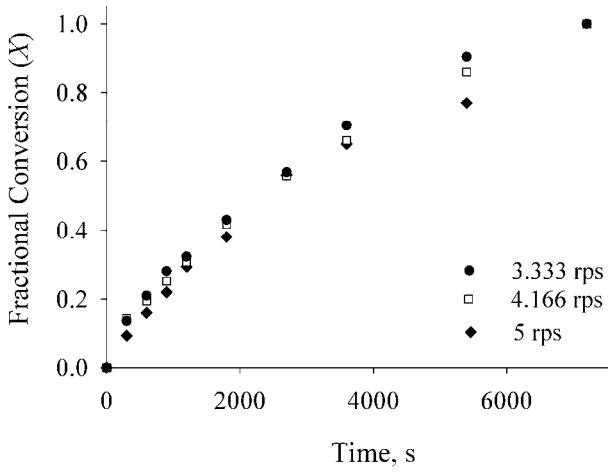

Fig. 2. The effect of stirring speed on the fractional conversion of $SrSO_4$ (temperature: 323 K, CO_3^{2-} concentration: 33 mol m^{-3} and particle size: 53––75 μm).

The effects of temperature and CO_3^{2-} ion concentration

The experiments were not performed at temperatures above 323 K, since the AC solution decomposed at 331 K. Celestite concentrate (0.016 mol) with particle sizes of 53–75μm, a 1×10^{-3} m^3 solution of AC that was obtained by dissolving 0.5, 0.75, 1, 1.25 or 1.5 mol of AC were investigated at 293, 303, 313 of 323 K to study the effects of temperature and CO_3^{2-} concentration on the conversion reaction of $SrSO_4$. The concentrations of CO_3^{2-}, HCO_3^-, NH_4^+ and molecularly dissolved NH_3 used in the experiments are given in Table III. It can be clearly seen that with increasing AC, all of the concentrations (CO_3^{2-}, HCO_3^-, NH_4^+ and molecularly dissolved NH_3) increased. On the other hand, with increasing temperature, the CO_3^{2-} and NH_4^+ concentrations decreased while the concentrations of HCO_3^- and molecularly dissolved NH_3 increased. The typical *X vs. t* diagrams at different temperatures and CO_3^{2-} concentrations are shown in Fig. 3 (other investigated cases are shown in Fig. 2-S of the Supplementary material), from which it could be seen that for each constant temperature, the frac-

tional conversion decreased with increasing concentration of CO_3^{2-}, which indicates that the conversion rate is inversely proportional to the CO_3^{2-} concentration. Although the CO_3^{2-} concentration is lower, X increased with increasing temperature, which is in accordance with the Arrhenius Equation, as expected.

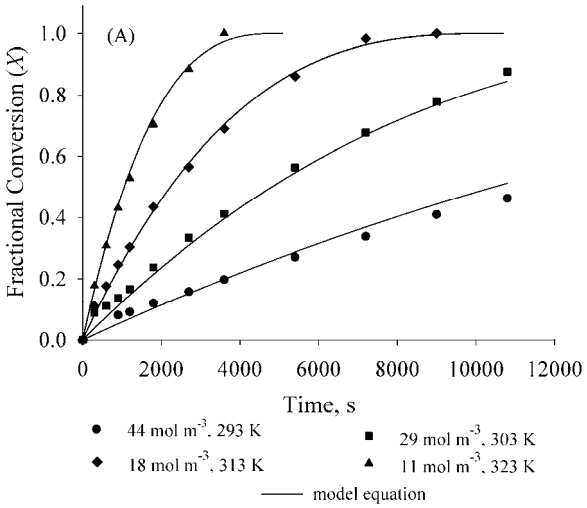

Fig. 3. The effects of temperature and CO_3^{2-} concentration on the fractional conversion of $SrSO_4$ (particle size: 53–75 μm, stirring speed: 5 rps).

The effect of particle size

For the determination of the effect of particle size on the conversion of $SrSO_4$, 90–125, 53–75 and 38–45 μm sized particles were used. The experimental conditions were 0.016 mol celestite concentrate, 1×10^{-3} m^3 solution that was obtained by dissolving 1 mol AC, 323 K and 5 rps. The X *vs.* t diagrams are shown in Fig. 4. It was observed that the fractional conversion of $SrSO_4$ increased with decreasing particle size.

Materials characterization

The XRD and SEM–EDS analytical techniques were applied to characterize the celestite concentrate and the solid product obtained during the conversion reaction using 0.016 mol of celestite concentrate with a particle size of 53–75 μm, 1×10^{-3} m^3 solution, 0.5 mol of AC, 323 K and 5 rps. The XRD patterns and SEM–EDS images of the celestite concentrate and solid product are presented in Figs. 5 and 6, respectively, from which it can be seen that the celestite concentrate contained mainly $SrSO_4$ and the reaction product $SrCO_3$.

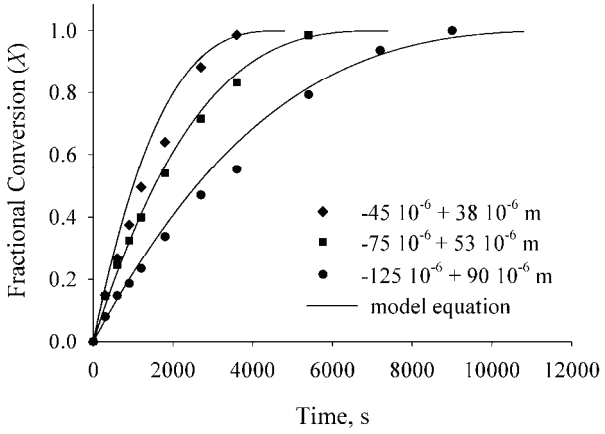

Fig. 4. The effect of particle size on the fractional conversion of $SrSO_4$ (temperature: 323 K, CO_3^{2-} concentration: 22 mol m^{-3}, stirring speed: 5 r.p.s.)

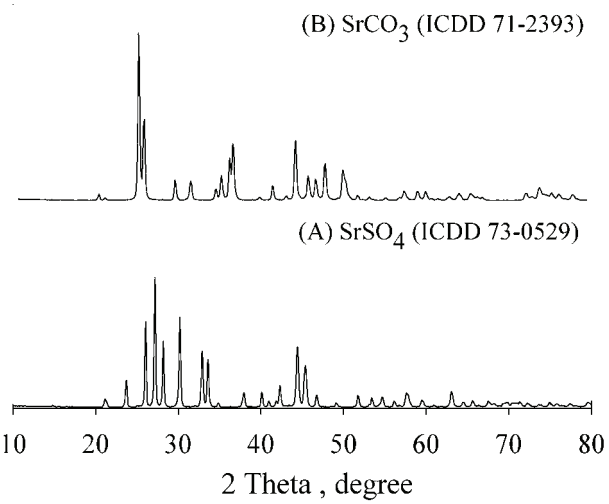

Fig. 5. XRD diagrams, A – celestite concentrate ($SrSO_4$) and B – reaction product ($SrCO_3$).

Kinetic evaluation of conversion reaction

The molar volumes of $SrSO_4$ and $SrCO_3$ are 46.38×10^{-6} and 39.47×10^{-6} m^3 mol^{-1}, respectively. The lower molar volume of $SrCO_3$ is an indication that the product layer that surrounds the reactant had to be porous. In order for the reaction to proceed, CO_3^{2-} have to diffuse through the pores of the $SrCO_3$ layer towards the surface of $SrSO_4$ and the SO_4^{2-} that are formed during the conversion reaction have to diffuse through the same porous layer in the opposite direction towards the solution. When the resistance of the pores of the product layer is high, the reaction becomes diffusion controlled. If the sizes of the pores of the product layer are large enough, the reaction will be chemically controlled.

According to the "shrinking core model",[26] in the case of the establishment of a constant temperature (isothermal condition) and a constant CO_3^{2-} concen-

tration on the surface of the dense spherical particles of $SrSO_4$, if the reaction is under chemical reaction control, the change of X with t is given by:

$$1-(1-X)^{1/3}=\frac{bkc^m}{\rho r}t=\lambda t \quad (10)$$

where b denotes the stoichiometric coefficient, k the reaction rate constant, c the CO_3^{2-} concentration, m the reaction order for CO_3^{2-}, ρ the density of the $SrSO_4$ particles and r the average radius of the particles. When $1-(1-X)^{1/3}$ *vs.* t diagrams are plotted, the slope of these straight lines gives λ. It can be seen in Fig. 7 (some additional examples are given in Fig. 3-S of the Supplementary material) that the relationship between $1-(1-X)^{1/3}$ and t was linear. This finding shows that the topochemical reaction was under chemical control.

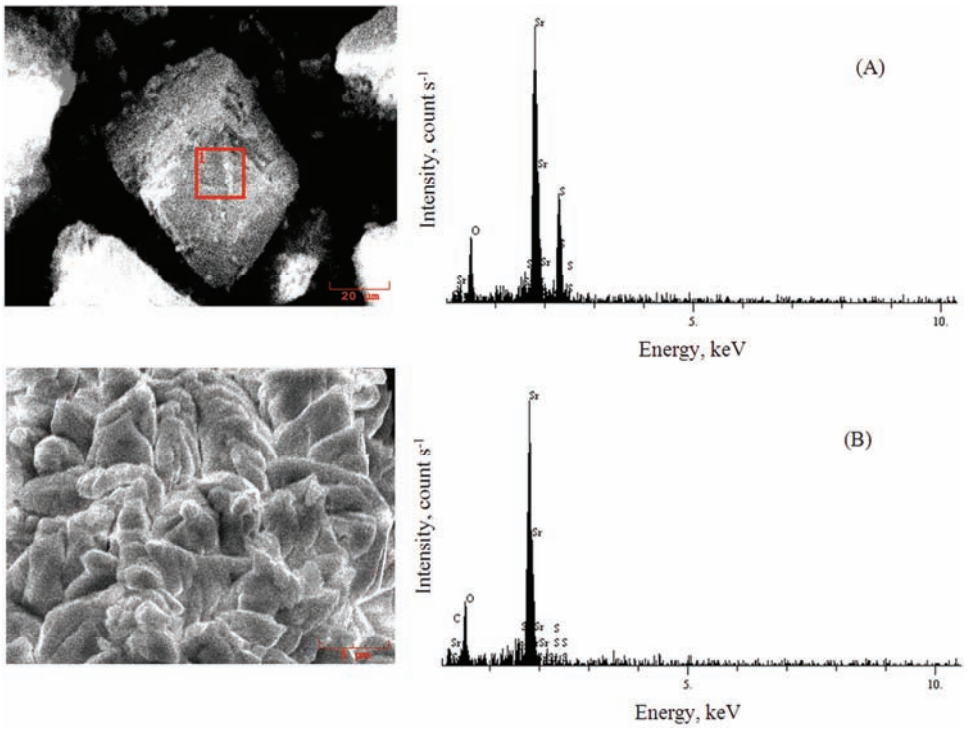

Fig. 6. SEM images and EDS analyses, A – celestite concentrate and B – reaction product.

Considering Eq. (10), at constant temperature and various CO_3^{2-} concentrations, Eq. (11) is valid:

$$\lambda=\alpha c^m \quad (11)$$

where α is given by $bk/\rho R$. The natural logarithm of Eq. (11) gives Eq. (12):

$$\ln \lambda = \ln \alpha + m \ln c \tag{12}$$

According to Eq. (12), the slope of ln λ *vs.* ln c will give m. The intersection at the ordinate axis gives ln α when ln $c \rightarrow 0$. The term α in Eq. (12) includes k. For various CO_3^{2-} concentrations at constant temperatures, ln λ *vs.* ln c diagrams are plotted in Fig. 8, from which it can be seen that parallel straight lines with slopes of –1/2 were obtained, which is the value of m. The k values were calculated from the α values by considering that $r = 64\times10^{-6}m$, $\rho = 21600$ mol m^{-3} and $b = 1$. The change of k with the absolute temperature can be determined by the Arrhenius Equation (Eq. (13)):

$$\ln k = \ln A_0 - \frac{E_a}{RT} \tag{13}$$

where A_0 is the pre-exponential factor, E_a the apparent activation energy and R the gas constant.

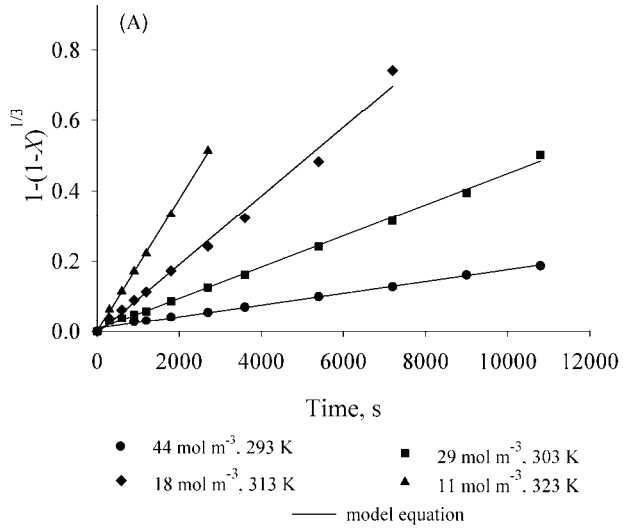

Fig. 7. $1–(1–X)^{1/3}$ *vs.* time diagrams for different concentrations of CO_3^{2-} and temperatures.

The relationship between ln k and $1/T$ is shown in Fig. 9. The slope of this line gives $– E_a/R$ and intercept at the ordinate axis for $1/T = 0$ gives ln A_0. From these values, E_a was calculated as 41.9 kJ mol^{-1} and A_0 as 171.2 (mol m^{-3})$^{3/2}$ m s^{-1}.

Equation (14) was obtained by replacing the ρ and b values with the calculated values of A_0, E_a and m in Eq. (10):

$$X = 1 - \left[1 - \frac{171.2 e^{-5046.22/T}}{21600r} c^{-1/2} t\right]^3 \tag{14}$$

Equation (14) shows the change of X with respect to R and t.

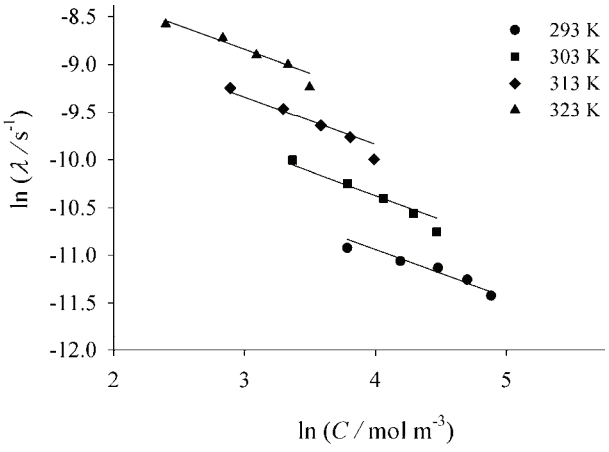

Fig. 8. ln λ *vs.* ln c diagrams.

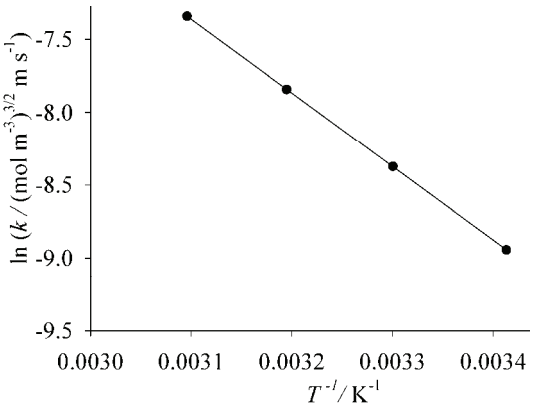

Fig. 9. Arrhenius plot (ln k *vs.* T^{-1} diagram).

All of the continuous lines given in Fig. 3 represent X *vs.* t, which were calculated and drawn according to Eq. (14). As can be seen in Fig. 3, there is a good agreement between the experimentally obtained values and the diagrams drawn using Eq. (14). Moreover, the X *vs.* t diagrams drawn using Eq. (14) for the different investigated particle sizes are shown as continuous lines in Fig. 4. Again, there is a good agreement between the experimental values and the diagrams plotted according to Eq. (14) using different r values.

Iwai and Toguri studied the conversion of celestite in Na_2CO_3 solution and concluded that during the initial stage of the reaction, the conversion rate was controlled by the dissolution rate of $SrSO_4$ and, therefore, the reaction rate was independent of the concentration of CO_3^{2-} (zero order).[5] They indicated that as the reaction proceeds, a $SrCO_3$ layer will be densely deposited on the celestite surface. As a result, the rate-determining step changed to the diffusion rate of

SO_4^{2-} through the pores of $SrCO_3$. They concluded that the decrease in the conversion with increasing CO_3^{2-} concentration was a result of the change in the morphology of the $SrCO_3$. They obtained apparent activation energies of 71.5 and 64.1 kJ mol^{-1} for the surface reaction and the diffusion step, respectively.

Castillejos *et al.* investigated the effects of stirring speed, particle size, Na_2CO_3 and Na_2SO_4 concentrations, temperature, solution pH and solid/liquid ratio on the conversion reaction of $SrSO_4$ to $SrCO_3$ in solutions containing Na_2CO_3.[6] They concluded that the reaction is topochemical, and the rate-determining step is the diffusion rate of CO_3^{2-} through the pores of the product layer. They found that the reaction rate increased with increasing temperature and decreasing particle size. They calculated an apparent activation energy for the diffusion rate of 70.0 kJ mol^{-1}.

The activation energy reported by Iwai *et al.* of 64.1 kJ mol^{-1} is in agreement with that reported by Castillejos *et al.* (70.0 mol^{-1}).[5,6] It is unlikely that reactions under diffusion rate control would have a high value of the activation energy. Thus, Castillejos *et al.* concluded that the high value of the activation energy for the reaction under diffusion rate control is indicative of the production of a compact layer with very tortuous pores. Therefore, the effective diffusivities calculated in their work fell in the range between 1.2×10^{-13} and 6.7×10^{-12} m^2 s^{-1}.[6]

The findings of Bingol *et al.* were similar to those of Iwai and Toguri and Castillejos *et al.* [5,6,16] They claimed that the conversion reaction was nearly completed at 333 K within 4 h and a neural model was used for computing the conversion kinetics.

In the above-mentioned studies, the pH of the solution was high (11–12). However, in the present study, the reaction proceeded at lower pH (8.22–9.04) and CO_3^{2-} concentrations 11–133 mol m^{-3} because of the rapid equilibrium reaction (Reaction (5)) with respect to conversion reaction (Reaction (8)). In this study, it was determined that the reaction rate was under chemical reaction rate control and the activation energy for the reaction was calculated to be 41.9 kJ mol^{-1}. The reaction rate was found to be inversely proportional to the CO_3^{2-} concentration. It was found that the kinetic model equation (Eq. (14)) derived in this study was in good agreement with all the experimentally obtained fractional conversion values at different reaction times.

CONCLUSIONS

The complete dissolution of ammonium bicarbonate and hydrolysis of ammonium carbamate present in AC gave a aqueous solution that contained CO_3^{2-}, HCO_3^-, NH_4^+ and dissolved NH_3.

During the conversion of $SrSO_4$, porous $SrCO_3$ formed on the surfaces of the $SrSO_4$ particles, enabling the total conversion of $SrSO_4$.

A stirring speed of 5 rps was sufficient to eliminate the resistance of the liquid film that surrounds the surfaces of the $SrSO_4$ particles.

The conversion rate increased with increasing temperature and decreasing particle size, whereas it decreased with increasing CO_3^{2-} concentration.

The heterogeneous reaction kinetics of solid $SrSO_4$ particles with CO_3^{2-} in aqueous solution was explained with the "shrinking core model". The topochemical reaction was under chemical reaction control. The reaction order for CO_3^{2-}, the activation energy and the pre-exponential factor were calculated to be –1/2, 41.9 kJ mol^{-1} and 171.23 (mol m^{-3})$^{3/2}$ m s^{-1}, respectively. The derived kinetic model equation was in good agreement with all the experimental conversion values obtained at different reaction times.

SUPPLEMENTARY MATERIAL

Experimental set up, X and $1–(1–X)^{1/3}$ *vs.* time diagrams are available electronically from http://www.shd.org.rs/JSCS/, or from the corresponding author on request.

Acknowledgement. The authors gratefully acknowledge the financial support of the Scientific Research Projects Coordination Unit of Istanbul University (Project No. 2332).

ИЗВОД

КИНЕТИКА КОНВЕРЗИЈЕ ЦЕЛЕСТИТА У СТРОНЦИЈУМ-КАРБОНАТ У РАСТВОРИМА КАРБОНАТНИХ, БИКАРБОНАТНИХ, АМОНИЈУМ ЈОНА И АМОНИЈАКА

MERT ZORAGA и CEM KAHRUMAN

Istanbul University, Engineering Faculty, Metallurgical and Materials Engineering Department, 34320, Avcilar, Istanbul, Turkey

Концентрат целестита ($SrSO_4$) конвертован је у $SrCO_3$ у растворима који су садржали CO_3^{2-}, HCO_3^-, NH_4^+ и растворени амонијак. Испитивани су ефекти брзине мешања, концентрације CO_3^{2-}, температуре и величине честица $SrSO_4$ на брзину реакције. Утврђено је да брзина конверзије $SrSO_4$ расте са температуром и смањивањем величине честица, а опада са повећањем концентрације CO_3^{2-}. Конверзију контролише хемијска реакција, а за објашњење кинетике реакције показао се погодним „*shrinking core model*“. Одређена је вредност енергије активације реакције конверзије од 41,9 kJ mol^{-1}. Састав реакционог раствора одређиван је куплованом методом плазма – оптичка емисиона спектроскопија. Чврсти реактанати и производи окарактерисани су скенирајућом електронском микроскопијом са енергетском дисперзионом спектроскопијом (SEM–EDS) и техником ренгенске дифракције праха (XRD).

(Примљено 7. марта, ревидирано 21. маја 2013)

REFERENCES

1. M. Erdemoglu, M. Canbazoglu, *Hydrometallurgy* **49** (1998) 135
2. K. A. Kobe, N. J. Deiglmeier, *Ind. Eng. Chem.* **35** (1943) 323
3. G. Owusu, J. E. Litz, *Hydrometallurgy* **57** (2000) 23
4. H. Dogan, M. Koral, S. Kocakusak, *Hydrometallurgy* **71** (2004) 379
5. M. Iwai, J. M. Toguri, *Hydrometallurgy* **22** (1989) 87

6. A. H. Castillejos-Escobar, F. P. De La Cruz-Del Bosque, A. Uribe-Salas, *Hydrometallurgy* **40** (1996) 207
7. F. De Buda, U.S. Patent 4,666,688 (1987)
8. S. Kocakusak, R. Tolun, H. Dogan, K. Akcay, H. J. Koroglu, H. Yuzer, M. Koral, F. Isbilir, O. T. Savascı, T. Ayok, Patent No: TR2001/0326521.5 (2003)
9. M. Erdemoglu, M. Sarıkaya, M. Canbazoglu, *J. Dispers. Sci. Technol.* **27** (2006) 439
10. S. Aydogan, M. Erdemoglu, A. Aras, G. Ucar, A. Ozkan, *Hydrometallurgy* **84** (2006) 239
11. M. Erdemoglu, S. Aydogan, M. Canbazoglu, *Hydrometallurgy* **86** (2007) 1
12. A. Obut, P. Balaz, I. Girgin, *Miner. Eng.* **19** (2006) 1185
13. N. Setoudeh, N. J. Welham, S. M. Azami, *J. Alloy. Compd.* **492** (2010) 389
14. R. Suarez-Orduna, J. C. Rendon-Angeles, K. Yanagisawa, *Int. J. Miner. Process.* **83** (2007) 12
15. S. Ni, X. Yang, T. Li, *Mater. Lett.* **65** (2011) 766
16. D. Bingol, S. Aydogan, S. S. Gultekin, *Chem. Eng. J.* **165** (2010) 617
17. D. Bingöl, S. Aydogan, S. K. Bozbas, *J. Ind. Eng. Chem*. **18** (2012) 834
18. D. Bingöl, S. Aydogan, S. K. Bozbas, *Metall. Trans., B* **43** (2012) 1214
19. F. Habashi, *Handbook of Extractive Metallurgy (Vol.4 Ferroalloys Metals, Alkali Metals, Alkaline Earth Metals)*, Wiley–VCH, Weinheim, 1997, p. 2333
20. A. O. Kalpakli, S. Ilhan, C. Kahruman, I. Yusufoglu, *Hydrometallurgy* **121**–**124** (2012) 7
21. W. J. Cai, Y. Wang, *Oceanography* **43** (1998) 657
22. S. Clegg, M. Whitfield, *Geochim. Cosmochim. Acta* **59** (1995) 122403
23. D. R. Gaskell,. *Introduction to the Thermodynamics of Materials*, 4th ed., Taylor & Francis, New York, 2003, p. 102
24. N. Wen, M. H. Brooker, *J. Phys. Chem.* **99** (1995) 359
25. F. Qin, S. Wang, I. Kim, H. F. Svendsen, C. Chen, *Int. J. Greenh. Gas Con.* **5** (2011) 405
26. O. Levenspiel, *Chemical Reaction Engineering*. 3rd ed., Wiley, New York, 1999, p. 575.

Journal of the Serbian Chemical Society
JSCS@tmf.bg.ac.rs • www.shd.org.rs/JSCS
J. Serb. Chem. Soc. 79 (3) S41–S43 (2014) *Supplementary material*

SUPPLEMENTARY MATERIAL TO

Kinetics of conversion of celestite to strontium carbonate in solutions containing carbonate, bicarbonate and ammonium ions, and dissolved ammonia

MERT ZORAGA and CEM KAHRUMAN*

Istanbul University, Engineering Faculty, Metallurgical and Materials Engineering Department, 34320, Avcilar, Istanbul, Turkey

J. Serb. Chem. Soc. 79 (3) (2014) 345–359

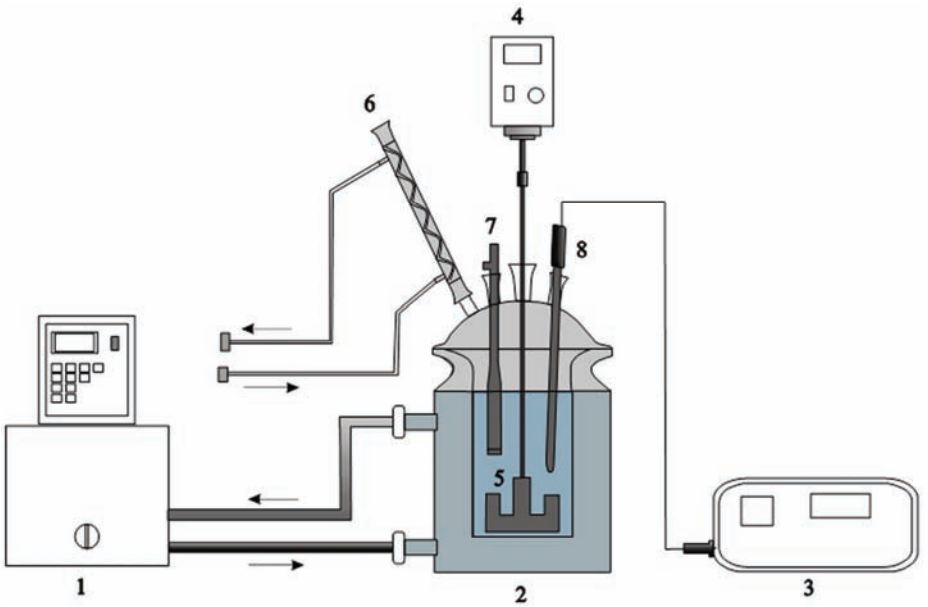

Fig. 1. Experimental set up (1 – thermostat, 2 – glass reactor, 3 – PT 100 probe, 4 – mechanical stirrer, 5 – poly(tetrafluoroethylene) (PTFE)-coated propeller, 6 – condenser, 7 – sampler and 8 – temperature sensor).

* Corresponding author. E-mail: cemcemce@istanbul.edu.tr

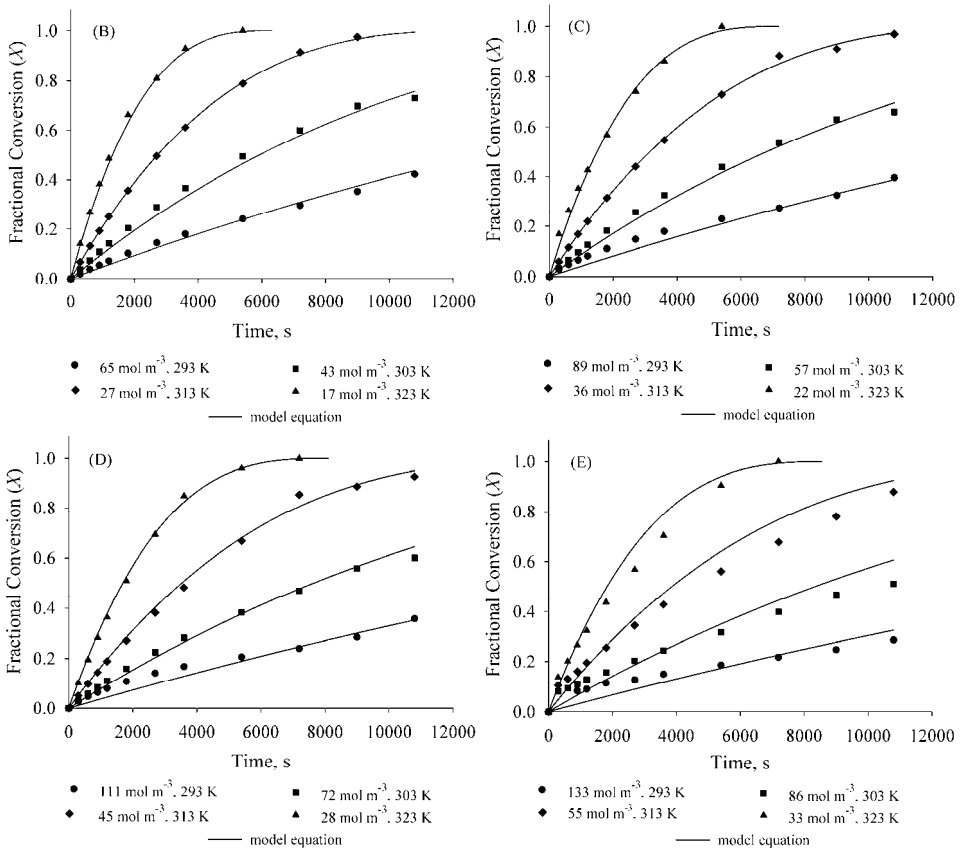

Fig. 2-S. The effects of temperature and CO_3^{2-} concentration on the fractional conversion of $SrSO_4$ (particle size: 53–75 μm, stirring speed: 5 rps).

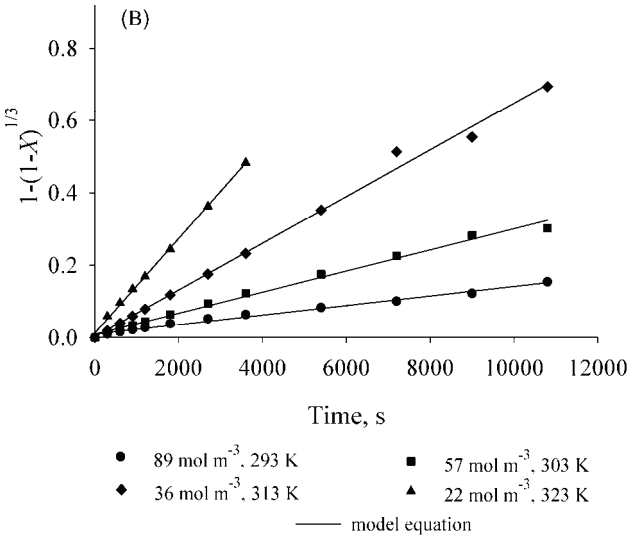

Fig. 3-S. $1–(1–X)^{1/3}$ *vs*. time diagrams for different concentrations of CO_3^{2-} and temperatures.

Journal of the Serbian Chemical Society
JSCS-info@shd.org.rs • www.shd.org.rs/JSCS
J. Serb. Chem. Soc. *79* (3) 361–377 (2014) UDC 628.3+535.6–26:544.4:66.011:66.099.72
JSCS–4591 *Original scientific paper*

Kinetics and optimization of the decoloration of dyeing wastewater by a schorl-catalyzed Fenton-like reaction

HUAN-YAN XU*, WEI-CHAO LIU, SHU-YAN QI, YAN LI, YUAN ZHAO and JI-WEI LI

School of Material Science and Engineering, Harbin University of Science and Technology, Harbin, 150040, P. R. China

(Received 25 February, revised 17 June 2013)

Abstract: The kinetics and optimization of the decoloration of an active commercial dye, argazol blue BFBR (ABB), by a heterogeneous Fenton-like reaction catalyzed by natural schorl were investigated in this study. The kinetic investigations revealed that the first-order kinetic model was more favorable to describe the decoloration of ABB under different reaction conditions than the second-order and Behnajady–Modirshahla–Ghanbery models. The relationship between the reaction rate constant k and reaction temperature T followed the Arrhenius Equation, with an apparent activation energy E_a of 51.31 kJ·mol^{-1}. The central composite design under the response surface methodology was employed for the experimental design and optimization of the ABB decoloration process. The significance of a second order polynomial model for predicting the optimal values of ABB decoloration was evaluated by the analysis of variance and 3D response surface plots for the interactions between the two variables were constructed. Then, the optimum conditions were determined.

Keywords: schorl; heterogeneous catalysis; argazol blue BFBR; response surface methodology; first-order kinetics.

INTRODUCTION

Different dyes can be found in effluents from various industries, such as the food processing, cosmetics, paper and pulp, dye manufacture, printing and textile industries.[1] Effluent containing reactive dyes from textile dyeing and finishing industries is a significant source of environmental pollution. Reactive dyes are extensively used to color cellulose and rayon textiles due to their bright colors, excellent colorfastness and easy dyeing operations. About 45 % of the annual production (700,000 tons) of commercially available dyestuffs belongs to the reactive dye class. Up to 50 % of a reactive dye can be hydrolyzed and left unusable in the dye bath. Reactive dyes are resistant to decomposition due to their aromatic molecular structures, and thus can remain in the environment for a

* Corresponding author. E-mail: xhy7587@aliyun.com
doi: 10.2298/JSC130225075X

long time.[2] With the increasing concern about environment protection, removal of dyes from wastewater has become a significant issue.[3] The discharge of dye wastewater into the environment induces both toxicological and esthetical problems as it can impede light, damage water resources and make food-chain organisms toxic.[4] Various treatment methods, such as sedimentation, chemical coagulation, electrochemical methodology, and biological treatment, have been extensively investigated. However, most of the above methods suffer from one or more limitations and none of them were successful in the complete removal of color from wastewater.[5] As one important kind of reactive dyes, the Argazol® BF series have a vinyl sulfone and a monochlorotriazine group, and show low sensitivity to variations in the following dyeing parameters, liquor ratio, dyeing temperature, salt, alkali, dyeing time, *etc*. Thus, Argazol® BF reactive dyes have been widely used for piece dyeing, package yarn dyeing, hank yarn dyeing, jigger dyeing and continuous dyeing. To the best of our knowledge, scarce reports have been published on the treatment of wastewater containing Argazol® BF reactive dyes.

In the last decades, advanced oxidation processes (AOPs) appeared to be an effective method for the degradation of refractory organic contaminants in waters and soils.[6–9] AOPs involves the *in situ* generation of hydroxyl radical ($^{\bullet}OH$), achieving the complete conversion of the target pollutant species to CO_2, H_2O and mineral acids,[10] *i.e.*, mineralization. Among all AOPs, the Fenton reaction, employing hydrogen peroxide (H_2O_2) as oxidant and ferrous ion as catalyst, has been regarded as one of the most powerful and attractive ones available.[6] However, for classic Fenton reagent, there were a number of disadvantages such as narrow pH range and Fe ions as secondary pollutants.[11] In principle, these limitations could be overcome by using heterogeneous Fenton-type catalysts, instead of homogeneous iron ions.

It is well accepted that the most important issue in a heterogeneous Fenton process was the development of a heterogeneous catalyst with high catalytic activity and long-term stability at a reasonable cost.[12] Low-cost mineral materials with special crystal structures or properties were the best alternatives as heterogeneous Fenton catalysts, behaving as the iron supporter or promoter. This process is called a mineral-catalyzed Fenton-like system. Natural iron-bearing minerals could be employed as iron sources to promote the generation of $^{\bullet}OH$ from H_2O_2. The main advantages of the application of iron minerals in Fenton chemistry are as follows: a) periods of catalyst life could be extended without the need for regeneration or replacement; b) the catalyst could be removed from the treated water by sedimentation or filtration; c) the pH of the treated media could be in the range 5–9; d) the reaction was almost insensitive to the concentration of inorganic carbonate.[13] However, in some cases, the degradation rates of organic substrates in these Fenton-like systems seemed to be slow. To accelerate the

degradation rate, ultrasonic or UV irradiation was often applied to assist Fenton-like systems.[14,15] Otherwise, an electrostatic field could also enhance the mineral-catalyzed Fenton-like system.[16,17] Schorl is one kind of minerals of the tourmaline group, which are complex borosilicate minerals belonging to the trigonal space group R3m.[18] The general formula of tourmaline can be written as $XY_3Z_6[T_6O_{18}][BO_3]V_3W$, where X = Ca, Na, K; Y = Li, Mg, Fe^{2+}, Mn^{2+}, Al, Cr^{3+}, V^{3+}, Fe^{3+}, (Ti^{4+}); Z = Mg, Al, Fe^{3+}, V^{3+}, Cr^{3+}; T = Si, Al; B=B; V = OH, O; W = OH, F, O.[19] The basic structural units are hexagonal rings of Si_6O_{18} that form the basal plane and are connected with Na, Li and Al octahedra and distorted BO_3 groups in planar coordination along [0001] with a three-fold symmetry structure.[20] Depending on the occupancy of the Y and X sites, tourmalines are classified as end members, dravite (Y = Mg), schorl (Y = Fe^{2+}), tsilaisite (Y = Mn), olenite (Y = Al) and elbaite (Y = Li, Al).[21] Due to the special crystal structure of a tourmaline, spontaneous "electrostatic poles" exist on its surface.[22] Thus, schorl is not only a natural iron-bearing mineral, but also has unique characteristics of pyroelectricity and piezoelectricity.

Encouraged by this, a Fenton-like reaction catalyzed by natural schorl was investigated for the degradation of various organic substrates.[23–25] These results revealed the schorl-catalyzed Fenton-like reaction could be effective for the decoloration of dyeing wastewater and the electrostatic field on the surface of schorl crystal could enhance the decoloration process. Nevertheless, the kinetics and optimization of this reaction process were not studied further, which could be beneficial to the engineering aspects of the process. Hence, the present study focused on the optimization of the decoloration of a commercial dye, argazol blue BFBR (ABB), by the schorl-catalyzed Fenton-like reaction using the response surface methodology (RSM). Meanwhile, the kinetic process is discussed in details, involving the comparison of three kinetic models.

EXPERIMENTAL

Materials

Powdered particles of schorl, in the size range of < 64 μm, were purchased from Wuhua-Tianbao Mining Resources Co. Ltd., Inner Mongolia, China. The particles of the natural sample were directly used in the experimental studies without any treatment. The schorl samples were characterized by X-ray diffraction (XRD) analysis, Fourier transform infrared spectroscopy (FTIR) and scanning electron microscopy (SEM) with X-ray energy dispersive spectroscopy (EDS). Detailed information, including equipment, conditions, procedures and respective characterization data, were described elsewhere.[25] All chemical reagents used in this study were of analytical grade. Solutions were prepared in deionized water.

Decoloration methods

A stock solution containing ABB (2000 $mg \cdot L^{-1}$) was prepared and subsequently diluted to the required concentrations for the experimental work. The pH was adjusted by addition of sodium hydroxide (NaOH) and nitric acid (HNO_3) to the ABB solutions. The concentration of hydrogen peroxide (H_2O_2) was 30 %. Then, the schorl sample was added into 100 mL of solu-

tion of the required concentration of ABB in a conical flask. After sealing, the conical flasks were placed in a constant-temperature water-bath at different temperatures for different contact times. At regular time intervals, 2 mL of the reaction solution was collected from the reactor for measurements of the ABB concentration, using a 721-type UV–Vis spectrophotometer at a wavelength of 608 nm. The residual ratio, c_t/c_0, was used to express the decoloration efficiency of ABB, where c_0 is the initial concentration of the ABB wastewater and c_t the concentration at contact time t. In order to check the reproducibility of the results, random tests were performed for different experimental conditions.

Kinetic models

The kinetics of Fenton process can be quite complex owing to the large number of steps realized simultaneously during the process. Three kinetic models, the first-order, the second-order and Behnajady–Modirshahla–Ghanbery (BMG), were employed to test the fitting of experimental data obtained from the decoloration processes. The linear forms of these models are given in Eqs. (1)–(3), respectively:[26]

$$\ln\frac{c_0}{c_t} = k_1 t \tag{1}$$

$$\frac{1}{c_t} - \frac{1}{c_0} = k_2 t \tag{2}$$

$$\frac{t}{1-(c_t/c_0)} = m + bt \tag{3}$$

where k_2 is the second-order rate constant, and m and b are the two constants of the BMG model relating to oxidation capacities and reaction kinetics. The reaction rate constants for the heterogeneous Fenton decoloration of ABB were gained using linear regression of the three models. The order of the reaction was determined by the quantity of linear fit *via* the coefficient of determination (R^2).[27]

Experimental design, analysis and optimization

Central composite design (CCD) under the response surface methodology (RSM) was employed for the experimental design and optimization of ABB decoloration process. Base on previous experience of dyeing wastewater treatment in industrial applications, four factors, in this work, were selected as independent variables. They are the H_2O_2 concentration (mM), the schorl dosage ($g \cdot L^{-1}$), the solution pH and the reaction time (min), assigned with the following notations X_1, X_2, X_3 and X_4, respectively. The decoloration ratio of ABB (Y, %) was chosen as the output variable (response). Since the typical temperature of wastewater drained from dyeing and finishing mills is usually around 50 °C,[28] the temperature of the ABB simulated wastewater was maintained at 50 °C for all the designed experiments. The experimental design, mathematical modeling and optimization were performed with Design Expert 8.0.5.0 software (Stat-Ease, Inc.). For the statistical calculations, the variable X_i was coded as x_i according to the following equation:[29]

$$x_i = \frac{X_i - X_0}{\delta X} \tag{4}$$

where x_i is the code value, X_i is the uncoded value, X_0 is the value of X_i at the center point and δX presents the step change. The experimental ranges and the levels of the independent variables for ABB decoloration are listed in Table I. Preliminary experiments were imple-

mented to determine the ranges of the independent variables. A second-order regression model was employed to analyze and fit the responses to the independent variables (Eq. (5)):[30,31]

$$Y = \beta_0 + \sum_{i=1}^{k} \beta_i X_i + \sum_{i=1}^{k} \beta_{ii} X_i^2 + \sum_i \sum_j \beta_{ij} X_i X_j \quad (5)$$

where Y is response (ABB decoloration ratio); X_i and X_j input variables that influence the response (Y); β_0 an intercept constant; β_i the first-order regression coefficient; β_{ii} the second--order regression coefficient representing the quadratic effect of factor i; and β_{ij} the coefficient of interaction between factors i and j. Analysis of variance (ANOVA) was conducted to determine the significance of the model and the regression coefficient. Otherwise, it should be mentioned that all experiments were performed in duplicate and the average of the decoloration ratio was taken as the response. The standard deviation (*SD*) was less than 3 %.[32]

TABLE I. Variables and their codes and real experimental values used in the CCD

Variable	Coded level				
	–2	–1	0	1	2
X_1 / mM	0	9.69	19.38	29.07	38.76
X_2 / g·L^{-1}	0	2.5	5	7.5	10
X_3	2	4	6	8	10
X_4 / min	0	5	10	15	20

RESULTS AND DISCUSSION

Decoloration of ABB

A series of experimental results demonstrated that the ABB decoloration efficiency increased by, respectively, increasing the H_2O_2 concentration, the schorl dosage, temperature and by decreasing the pH. Figure 1 clearly indicates that the ABB decoloration efficiency increases with increasing H_2O_2 concentration. When the added H_2O_2 concentration was 9.69 mM, , about half of the

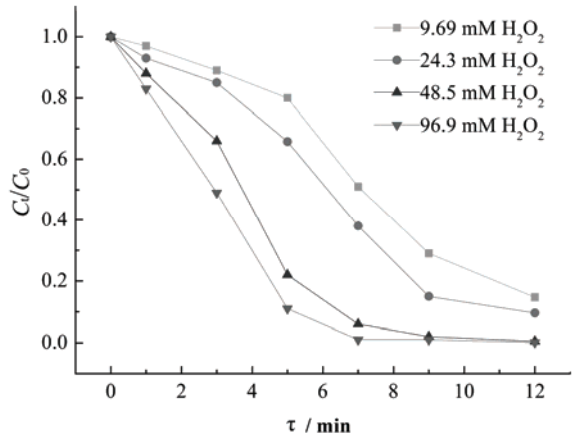

Fig. 1. The effect of H_2O_2 concentration on ABB decoloration by the schorl-catalyzed Fenton-like reaction at pH 6, T = 328 K, $[ABB]_0$ = 200 mg·L^{-1} and $[schorl]_0$ = 10 g·L^{-1}.

ABB dye had been decolored after 7 min of reaction; whereas it was completely decolored within the same reaction time when the concentration of added H_2O_2 was 96.9 mM. The increase in the H_2O_2 concentration resulted in an increase in the reaction activity, as expected, due to an increase of $^{\bullet}OH$.[33] It should be noted that the ABB decoloration efficiency increased most significantly when H_2O_2 concentration was increased from 24.3 to 48.5 mM. For a higher addition of H_2O_2, the decoloration efficiency increased slowly because of the scavenging of $^{\bullet}OH$ by the excess H_2O_2.[34]

The effect of schorl dosage on the decoloration efficiency of ABB was also investigated in this work. The results presented in Fig. 2 show that the activity of this heterogeneous Fenton system for ABB decoloration increases with increasing schorl dosage. This behavior could be attributed to the fact that with increasing amount of schorl catalyst, more active Fe sites are available on the catalyst surface for accelerating the decomposition of H_2O_2 (heterogeneous catalysis), and more Fe ion are leached into the solution, leading to an increase in the number of $^{\bullet}OH$ radicals (homogeneous catalysis).[25] Similar results were observed in Fenton-like reactions catalyzed by other Fe-bearing minerals.[35,36]

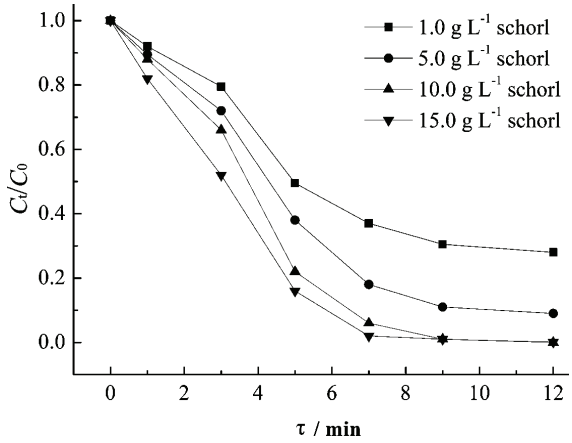

Fig. 2. The effect of the schorl dosage on ABB decoloration by schorl-catalyzed Fenton-like reaction at pH 6, T = 328 K, $[ABB]_0$ = 200 mg·L^{-1} and $[H_2O_2]_0$ = 48.5 mM.

The typical temperature of the textile effluents was usually around 50 °C.[28] Therefore, a temperature range of 25–65 °C (corresponding to 298–338 K) was studied with the goal of investigating the effect of this parameter on ABB decoloration. The results are shown in Fig. 3, from which it could be observed that the decoloration efficiency increased with increasing reaction temperature. A possible reason for this phenomenon might be that higher temperatures could provide more energy for the reactant molecules to overcome the reaction activation energy; hence, resulting in faster dye decoloration.[37] Another interpreta-

tion might be that increasing the reaction temperature accelerated the rate of •OH formation in the heterogeneous Fenton-like system.[33]

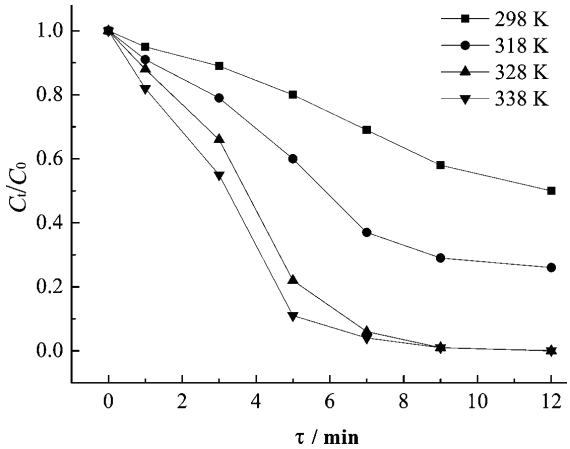

Fig. 3. The effect of reaction temperature on ABB decoloration by the schorl-catalyzed Fenton-like reaction at pH 6, $[ABB]_0$ = 200 mg·L^{-1}, $[H_2O_2]_0$ = 48.5 mM and $[schorl]_0$ = 10 g·L^{-1}.

Figure 4 suggests that, under the adopted experimental conditions, the reactivity of the system is dependent on the pH of the dye solution, exhibiting different decoloration behavior at acidic and alkaline pH values. At acidic pH values (2 and 4), more Fe ions were dissolved from the schorl catalyst into the solution, which then catalyzed the generation of more •OH from H_2O_2, resulting in a faster decoloration of dye by homogeneous catalysis of the process. At neutral and

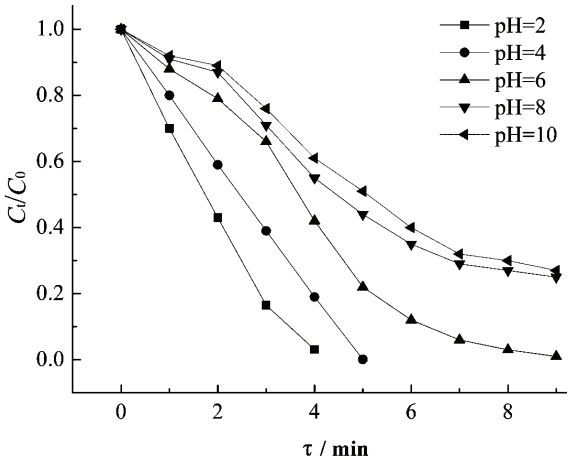

Fig. 4. The effect of solution pH on ABB decoloration by the schorl-catalyzed Fenton-like reaction at T =328 K, $[ABB]_0$ = 200 mg·L^{-1}, $[H_2O_2]_0$ = 48.5 mM and $[schorl]_0$ = 10 g·L^{-1}.

alkaline pH (6, 8 and 10), because there were fewer Fe ions leaching into the solution, it was proposed that H_2O_2 decomposition was catalyzed by active Fe sites on the surface of the schorl catalyst, *i.e.*, heterogeneous catalysis governed this process.[25]

According to the discussions above, it could be concluded that as the possible reaction mechanism of ABB decoloration, besides minor adsorption, the Fenton-like reaction was responsible for the whole decoloration process, including heterogeneous and homogeneous catalysis. Under acidic pH conditions, the homogeneous catalytic reaction played an important role in ABB decoloration and the generation of $^{\bullet}OH$ could be described as follows, where ≡Fe(II) and ≡Fe(III) represent the Fe(II) and Fe(III) species on the schorl surface, respectively:

$$\equiv \mathrm{Fe(II)} \xrightarrow{\mathrm{H^+}} \mathrm{Fe^{2+}_{(aq)}} \quad (6)$$

$$\equiv \mathrm{Fe(III)} \xrightarrow{\mathrm{H^+}} \mathrm{Fe^{3+}_{(aq)}} \quad (7)$$

$$\mathrm{Fe^{2+}_{(aq)} + H_2O_2 \rightarrow\ Fe^{3+}_{(aq)} + {}^{\bullet}OH + OH^-} \quad (8)$$

$$\mathrm{Fe^{3+}_{(aq)} + H_2O_2 \rightarrow\ Fe^{2+}_{(aq)} + {}^{\bullet}OOH + H^+} \quad (9)$$

At alkaline pH conditions, the heterogeneous catalytic reaction played an important role in ABB decoloration and the generation of •OH could be described as follows:

$$\equiv \mathrm{Fe(II) + H_2O_2 \rightarrow\ \equiv Fe(III) + {}^{\bullet}OH + OH^-} \quad (10)$$

$$\equiv \mathrm{Fe(III) + H_2O_2 \rightarrow\ \equiv Fe(II) + {}^{\bullet}OOH + H^+} \quad (11)$$

Kinetic studies

The parameters of kinetic models for the decoloration of ABB by the schorl--catalyzed Fenton-like system under different reaction conditions were calculated by application of linear regression analysis to ln (c_0/c_t) *vs*. *t* data for the first-order model, [($1/c_t$)–($1/c_0$)] *vs*. *t* data for the second-order model and $t/[1-(c_t/c_0)]$ *vs*. *t* data for the BMG model. The obtained parameters are given in Table II, from which it could be seen that the fittings of the second-order and the BMG models to the experimental data were not good as evidenced by the low determination coefficients. However, the values of determination coefficients for the first-order model were mostly higher than those of the second-order and the BMG models. Therefore, the first-order kinetic model is the best one to describe the decoloration of ABB under different reaction conditions by the schorl-catalyzed Fenton-like process. It has been reported that the fitting of the experimental kinetic data for the decoloration of dyes by a heterogeneous Fenton-like reaction catalyzed by other Fe-containing minerals was good with the first-order model,

TABLE II. Kinetic parameters of three models and their determination coefficient (R^2) for ABB decoloration under different reaction conditions

$[ABB]_0$ mg·L^{-1}	$[H_2O_2]_0$ mM	$[schorl]_0$ g·L^{-1}	T K	pH	First-order		Second-order		Behnajady–Modirshahla–Ghanbery		
					k_1 / min^{-1}	R^2	k_2 / M^{-1}·min^{-1}	R^2	m / min	b	R^2
200	9.69	10	328	6	0.17896	0.91072	0.00252	0.76646	33.14958	–1.95302	0.79215
200	24.3	10	328	6	0.22854	0.92092	0.00438	0.81464	16.85968	–0.46215	0.13555
200	48.5	10	328	6	0.50218	0.97941	0.0808	0.62077	6.8709	0.29817	0.79136
200	96.9	10	328	6	0.62983	0.95648	0.38206	0.51113	4.0723	0.57088	0.7856
200	48.5	1	328	6	0.11927	0.90732	0.00126	0.95065	11.38154	0.25604	0.02569
200	48.5	5	328	6	0.23489	0.9386	0.00507	0.93071	8.48622	0.24922	0.12377
200	48.5	15	328	6	0.63549	0.97201	0.37971	0.48902	4.13205	0.57328	0.83566
200	48.5	10	298	6	0.06188	0.98094	0.00045	0.96262	23.32937	0.00826	0.2498
200	48.5	10	318	6	0.14822	0.93247	0.00141	0.93927	11.26378	0.27885	0.1532
200	48.5	10	338	6	0.62514	0.97894	0.37824	0.47713	4.232	0.56332	0.79455
200	48.5	10	328	2	1.03091	0.90636	0.04811	0.58126	1.77142	0.74711	0.93748
200	48.5	10	328	4	0.47267	0.94205	1.00053	0.33765	3.53286	0.50986	0.77193
200	48.5	10	328	8	0.19456	0.98036	0.00203	0.97207	11.60779	–0.17252	0.0815
200	48.5	10	328	10	0.17932	0.97706	0.0018	0.95966	14.10038	–0.42688	0.096

for instance, the decoloration of the azo dye Orange G catalyzed by goethite[38] and acid Orange II by natural vanadium–titanium magnetite.[39]

From Table II, it could also be seen that, for the first-order model, the reaction rate constant k increased with increasing H_2O_2 concentration, schorl dosage and reaction temperature, but decreased with increasing solution pH. Among them, the relationship between the rate constant k and reaction temperature T should be mentioned and discussed because of its complexity in all chemical reactions. The rate constant k increases when the reaction temperature increases, which suggested that the mobility of the reactants from the bulk medium to the heterogeneous surface and the converted products from the surface to the bulk medium were more favored by the applied thermal energy.[27] The relationship between k and T could be described by five different equations. In this study, it follows the Arrhenius equation, due to the linear relationship between ln k and $10^3/T$, as illustrated in Fig. 5. The apparent activation energy of ABB decoloration could be calculated by comparing the obtained fitting equation with Arrhenius Equation, shown as follows:[27]

$$\text{Fitting equation: } \ln k = \frac{6170.99}{T} + 17.8337 \tag{12}$$

$$\text{Arrhenius Equation: } \ln k = \frac{E_a}{RT} + \ln A \tag{13}$$

where E_a is the Arrhenius activation energy for the reaction process, indicating the minimum energy that the reactants must have for the reaction to proceed, A is the Arrhenius factor and R is the gas constant (8.314 J·mol^{-1}·K^{-1}). Thus, the apparent activation energy E_a of the reaction in this work was determined to be 51.31 kJ·mol^{-1}. Generally, the activation energy of an ordinary thermal reactions is between roughly 60 and 250 kJ·mol^{-1}.[38] In the present study, the obtained activation energy value of 51.31 kJ·mol^{-1} was lower than that of an ordinary

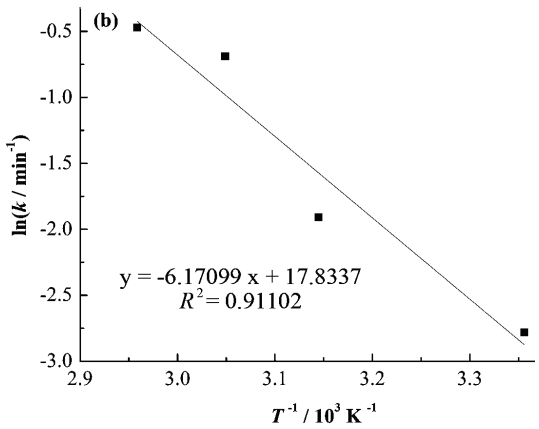

Fig. 5. The relationship between ln k and $10^3/T$.

thermal reaction, suggesting that this Fenton reaction process typically proceeds with a low energy barrier.[40]

Optimization by CDD under RSM

The effects of various experimental parameters (X_1, X_2, X_3 and X_4) in this reaction were investigated using CCD under RSM. Thirty experiments, with 4 factors and 5 levels for each factor were designed, which are listed in Table III. Among these 30 experiments, 6 experiments were repetition of the central point (run No. 1, 3, 17, 20, 21 and 24). All of the factors were in the centric point of their values in these experiments. The closeness of the responses of these 6 experiments could be a sign of the accuracy of the experiment process.[41] For predicting the optimal values of ABB decoloration within the experimental constrains, a second order polynomial model was fitted to the experimental results for the decoloration ratio of ABB. The obtained polynomial model is shown as follows:

$$\begin{aligned} Y = {} & 74.42 + 13.77X_1 + 4.45X_2 - 21.03X_3 + \\ & + 16.05X_4 + 0.40X_1X_2 - 4.81X_1X_3 - \\ & - 5.96X_1X_4 + 1.69X_2X_3 + 0.44X_2X_4 - \\ & - 3.00X_3X_4 - 6.00X_1^2 - 2.85X_2^2 - 2.93X_3^2 - 9.16X_4^2 \end{aligned} \quad (14)$$

TABLE III. Central composite design matrix together with the experimental and predicted values of the ABB decoloration ratios

Run	X_1 / mM	X_2 / g·L^{-1}	X_3	X_4 / min	Y / %	
					Experimental	Predicted
1	0.000	0.000	0.000	0.000	74.9	74.42
2	–1.000	–1.000	1.000	1.000	29.7	36.33
3	0.000	0.000	0.000	0.000	73.8	74.42
4	2.000	0.000	0.000	0.000	84.7	77.94
5	–1.000	1.000	–1.000	–1.000	24.8	32.83
6	0.000	2.000	0.000	0.000	79.7	71.91
7	–1.000	1.000	–1.000	1.000	91.3	83.73
8	–2.000	0.000	0.000	0.000	15.2	22.88
9	–1.000	1.000	1.000	1.000	43.5	48.68
10	1.000	1.000	–1.000	1.000	99.9	109.76
11	1.000	–1.000	1.000	1.000	49.6	41.51
12	0.000	0.000	0.000	–2.000	0.00	5.66
13	0.000	0.000	0.000	2.000	74.6	69.86
14	1.000	–1.000	–1.000	1.000	97.9	102.56
15	–1.000	–1.000	–1.000	1.000	85.3	78.13
16	0.000	–2.000	0.000	0.000	45.4	54.11
17	0.000	0.000	0.000	0.000	75.2	74.42
18	0.000	0.000	–2.000	0.000	99.8	104.76
19	0.000	0.000	2.000	0.000	24.7	20.66
20	0.000	0.000	0.000	0.000	73.8	74.42

TABLE III. Continued

Run	X_1 / mM	X_2 / g·L^{-1}	X_3	X_4 / min	Y / %	
					Experimental	Predicted
21	0.000	0.000	0.000	0.000	74.1	74.42
22	1.000	1.000	–1.000	–1.000	90.2	82.71
23	–1.000	1.000	1.000	–1.000	15.3	9.78
24	0.000	0.000	0.000	0.000	74.7	74.42
25	–1.000	–1.000	1.000	–1.000	9.10	–0.82
26	–1.000	–1.000	–1.000	–1.000	34.9	28.98
27	1.000	–1.000	1.000	–1.000	21.5	28.21
28	1.000	–1.000	–1.000	–1.000	82.5	77.26
29	1.000	1.000	1.000	1.000	50.4	55.46
30	1.000	1.000	1.000	–1.000	33.3	40.41

Statistical testing of this model was implemented by analysis of variance (ANOVA) and the results for the coded variable levels are given in Table IV. From the ANOVA analysis, it was shown that the calculated F value was 24.46, that is much larger than the critical value of 2.42 for $F_{0.05}$,[14,15] which implied that the derived quadratic polynomial model was significant.[42] The low probability value (p value < 0.0001) means that there was only a 0.01 % chance that such a model could occur due to noise.[32] The determination coefficient (R^2) quantitatively evaluated the correlation between the experimental data and the predicted responses.[29] The experimental results and the predicted ones obtained from the model (Eq. (8)) were compared and listed in Table III. It was found that

TABLE IV. ANOVA analysis for the obtained quadratic polynomial model

Source	Sum of squares	Degree of freedom	Mean square	F value	p-value (Prob>F)
Model	25921.02	14	1851.50	24.46	< 0.0001
X_1	4548.51	1	4548.51	60.09	< 0.0001
X_2	475.26	1	475.26	6.28	0.0242
X_3	10609.22	1	10609.22	140.15	< 0.0001
X_4	6182.46	1	6182.46	81.67	< 0.0001
X_1X_2	2.56	1	2.56	0.034	0.8566
X_1X_3	370.56	1	370.56	4.90	0.0429
X_1X_4	568.82	1	568.82	7.51	0.0152
X_2X_3	45.56	1	45.56	0.60	0.4499
X_2X_4	3.06	1	3.06	0.040	0.8433
X_3X_4	144.00	1	144.00	1.90	0.1880
X_1^2	988.11	1	988.11	13.05	0.0026
X_2^2	223.11	1	223.11	2.95	0.1066
X_3^2	235.00	1	235.00	3.10	0.0984
X_4^2	2303.71	1	2303.71	30.43	< 0.0001
Residual	1135.45	15	75.70	–	–
R^2			0.9580		
Adj. R^2			0.9189		
Pred. R^2			0.7586		

the predicted values matched the experimental ones reasonably well with R^2 = = 0.9580. Figure 6 (slope equals 1) suggests that the predicted decoloration ratio of ABB agrees well with the experimental values. Furthermore, the value of the adjusted determination coefficient (R^2) was also very high (0.9189), which indicated the high significance of the model.[27] In addition, values of Prob > F less than 0.0500 indicate that the model terms were significant and values greater than 0.1000 indicate that the model terms were not significant.[32] In this study, X_1, X_2, X_3, X_4, X_1X_3, X_1X_4, X_1^2, X_3^2 and X_4^2 were significant model terms. Thus, the statistical analysis of all experimental data showed that the H_2O_2 concentration, the schorl dosage, the solution pH and the reaction time had a significant effect on ABB decoloration in the schorl-catalyzed Fenton-like system.

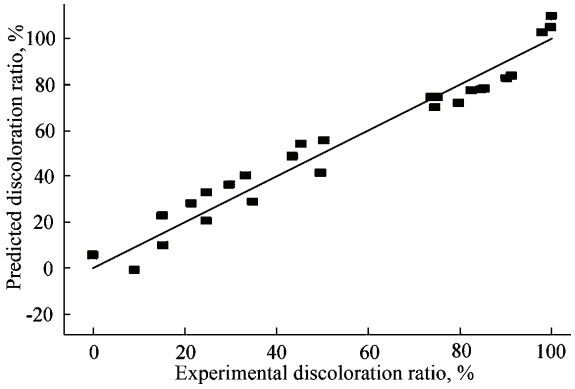

Fig. 6. Comparison of the predicted ABB decoloration ratios and the experimental values.

The 3D response surface plots for the interactions between two variables are presented in Fig. 7a–f with different interactions. As could be seen, the ABB decoloration ratio increased with increasing H_2O_2 concentration, schorl dosage and reaction time, but decreased with increasing solution pH, which is consistent with the one factorial experiment. The reasons have been interpreted in the section “Decoloration of ABB”. Nevertheless, the interactions between two independent variables were not significant, because the curvature of the three-dimensional surfaces was not pronounced.[31,43] The main goal of the optimization in this study was to determine the optimum values of the variables for the decoloration of ABB by the schorl-catalyzed Fenton-like reaction. Based on the model prediction, the optimum conditions for the decoloration of ABB by this process were determined to be 31.67 mM H_2O_2 concentration, 6.97 g·L^{-1} schorl dosage, solution pH 3.73 and 17.82 min reaction time, with the maximum ABB decoloration ratio of 99.94 %. The corresponding experimental value of ABB decoloration ratio under the optimum conditions was determined as 99.5 %, which was very close to the optimized one. It was confirmed that RSM was a powerful and satisfactory strategy to optimize the operational parameters of ABB decoloration by the heterogeneous Fenton-like reaction catalyzed by natural schorl.

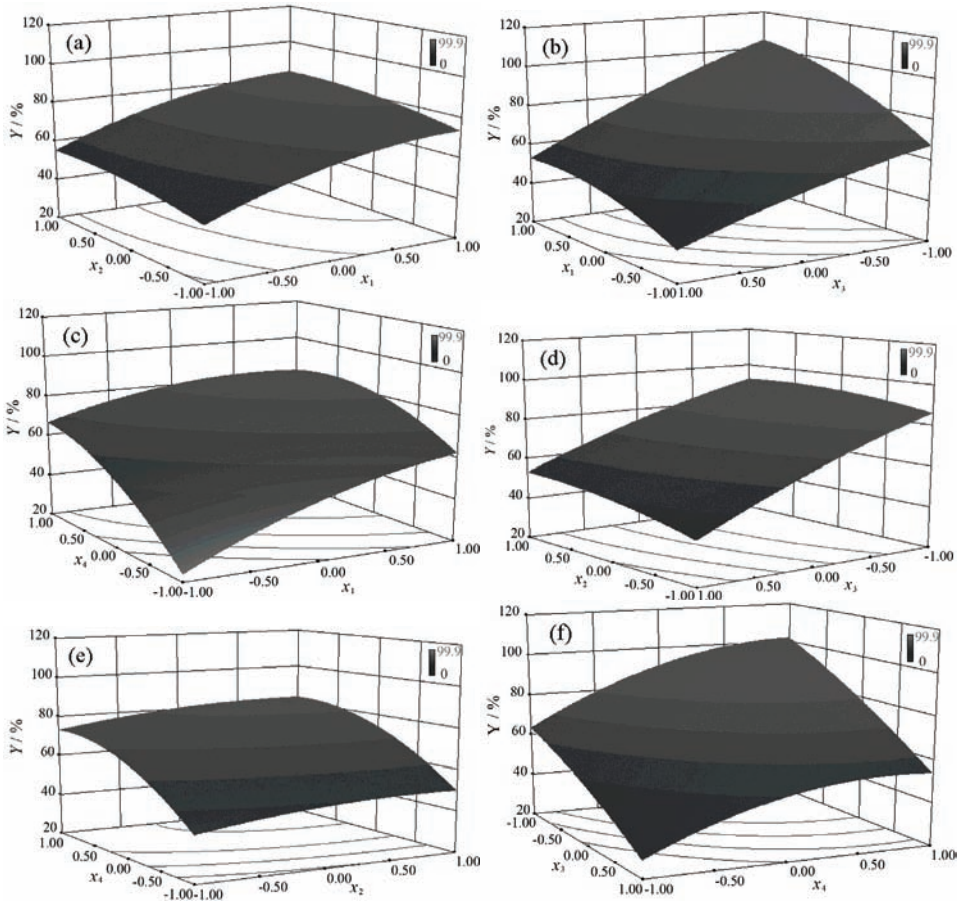

Fig. 7. The response surface plots for ABB decoloration with the interaction effect of: a) H_2O_2 concentration (X_1) and schorl dosage (X_2); b) H_2O_2 concentration (X_1) and solution pH (X_3); c) H_2O_2 concentration (X_1) and reaction time (X_4); d) schorl dosage (X_2) and solution pH (X_3); e) schorl dosage (X_2) and reaction time (X_4); f) solution pH (X_3) and reaction time (X_4).

CONCLUSIONS

The successful decoloration of dye ABB in water was achieved by the heterogeneous Fenton-like reaction using natural schorl as the catalyst. The efficiency of ABB decoloration increased with increasing H_2O_2 concentration, schorl dosage and reaction temperature, and decreasing solution pH. The first-order, second-order and BMG models were employed to investigate the kinetics of ABB decoloration. The values of determination coefficients for the first-order model were mostly higher than those of the second-order and BMG models. Therefore, first-order kinetic model was the best one to describe the decoloration of ABB under different reaction conditions. Further analysis indicated that the relationship between k and T followed the Arrhenius Equation, evidenced by the

linear relationship between ln k and $10^3/T$ and the apparent activation energy E_a of the reaction in this study was determined to be 51.31 kJ·mol^{-1}. CDD under RSM was used for the process optimization and 30 experiments, with 4 factors and 5 levels for each factor were designed. For predicting the optimal values of ABB decoloration within the experimental constrains, a second order polynomial model was fitted to the experimental results for the decoloration ratio of ABB. ANOVA analysis indicated the high significance of the model. 3D response surface plots for the interactions between two variables were constructed. Based on the model prediction, the optimum conditions for the decoloration of ABB by this process were determined to be 31.67 mM H_2O_2 concentration, 6.97 g·L^{-1} schorl dosage, solution pH 3.73 and 17.82 min reaction time, with the maximum ABB decoloration ratio of 99.94 %.

Acknowledgments. This work was supported by The National Natural Science Foundation of China (No. 51002040), The National College Students' Innovative Training Project (No. 201210214006) and The Science Foundation of the Heilongjiang Education Office (No. 12521071). Moreover, Prof. Huan-Yan Xu also expresses his appreciation for the financial support of the Program for New Century Excellent Talents in Heilongjiang Provincial Universities (No. 1253-NCET-010). Moreover, please add the following fund at the end of the part acknowledgements "Dr. Shu-Yan Qi shows her thank to Natural Science Youth Fund of Heilongjiang Province (No. QC2012C084).

ИЗВОД

КИНЕТИКА И ОПТИМИЗАЦИЈА ОБЕЗБОЈАВАЊА ОТПАДНЕ ВОДЕ ОД БОЈЕЊА ФЕНТОНСКОМ РЕАКЦИЈОМ КАТАЛИЗОВАНОМ ШОРЛОМ

HUAN-YAN XU, WEI-CHAO LIU, SHU-YAN QI, YAN LI, YUAN ZHAO и JI-WEI LI

School of Material Science and Engineering, Harbin University of Science and Technology, Harbin, 150040, P. R. China

Изучавана је кинетика и оптимизација обезбојавања активне комерцијалне боје argazol blue BFBR (ABB) хетерогеном Фентонском реакцијом катализованом природним шорлом. Изучавање кинетике открило је да је кинетички модел првог реда бољи за описивање обезбојавања ABB при различитим условима реакције, него модел другог реда и Behnajady–Modirshahla– Ghanbery модели. Однос између константе брзине реакције k и температуре T понашао се у складу са Аренијусовом релацијом, са привидном енергијом активације E_a од 51,31 kJ mol^{-1}. За дизајн експеримента и оптимизацију процеса обезбојавања ABB употребљен је дизајн са централним композитом по методологији површине одговора. Значај полиномијалног модела другог реда за предвиђање оптималних вредности за обезбојавање АББ оцењен је анализом варијансе и графицима 3D површина за интеракције између две променљиве. Затим су одређени оптимални услови.

(Примљено 25. фебруара 2012, ревидирано 17. јуна 2013)

REFERENCES

1. A. V. Patil, J. P. Jadhav, *Chemosphere* **92** (2013) 225
2. H. Xu, Y. Zhang, Q. Jiang, N. Reddy, Y. Yang, *J. Environ. Manage.* **125** (2013) 33

3. F. Zhang, Z. S. Zhao, R. Q. Tan, Y. Q. Guo, L. J. Cao, L. Chen, J. Li, W. Xu, Y. Yang, W. J. Song, *J. Colloid Interface Sci.* **386** (2012) 277
4. A. F. M. Alkarkhi, H. K. Lim, Y. Yusup, T. T. Teng, M. A. A. Bakar, K. S. Cheah. *J. Environ. Manage.* **122** (2013) 121
5. V. K. Gupta, R. Jain, T. A. Saleh, A. Nayak, S. Malathi, S. Agarwal. *Sep. Sci. Technol.* **46** (2011) 839
6. M. Bayat, M. Sohrabi, S. J. Royaee, *J. Ind. Eng. Chem.* **18** (2012) 957
7. S. Garcia-Segura, J. A. Garrido, R. M. Rodríguez, P. L. Cabot, F. Centellas, C. Arias, E. Brillas, *Water Res.* **46** (2012) 2067
8. M. Aleksić, H. Kušić, N. Koprivanac, D. Leszczynska, A. L. Božić, *Desalination* **257** (2010) 22
9. R. Prucek, M. Hermanek, R. Zbořil, *Appl. Catal., A* **366** (2009) 325
10. M. M. Abdel Daiem, J. Rivera-Utrilla, R. Ocampo-Pérez, J. D. Méndez-Díaz, M. Sánchez-Polo, *J. Environ. Manage.* **109** (2012) 164
11. G. Zhang, Y. Gao, Y. Zhang, Y. Guo, *Environ. Sci. Technol.* **14** (2010) 6384
12. M. Hartmann, S. Kullmann, H. Keller, *J. Mater. Chem.* **20** (2010) 9002
13. N. Dulova, M. Trapido, A. Dulov, *Environ. Technol.* **32** (2011) 439
14. Y. P. Zhao, J. Y. Hu, *Appl. Catal., B* **78** (2008) 250
15. M. Muruganandham, J. S. Yang, J. J. Wu, *Ind. Eng. Chem. Res.* **46** (2007) 691
16. W. P. Kwan, B. M. Voelker, *Environ. Sci. Technol.* **38** (2004) 3425
17. C. M. Sánchez-Sánchez, E. Expósito, J. Casado, V. Montiel, *Electrochem. Commun.* **9** (2007) 19
18. R. J. Barton, *Acta Crystallogr., B* **25** (1969) 1524
19. F. Yavuza, A. H. Gültekin, M. C. Karakaya, *Comput. Geosci.* **28** (2002) 1017
20. K. Krambrock, M. V. B. Pinheiro, S. M. Medeiros, K. J. Guedes, S. Schweizer, J.-M. Spaeth, *Nucl. Instrum. Methods, B* **191** (2002) 241
21. P. S. R. Prasad, S. D. Srinivasa, *Gondwana Res.* **8** (2005) 265
22. T. Nakamura, T. Kubo, *Ferroelectrics* **137** (1992) 13
23. H.-Y. Xu, M. Prasad, P. Wang, *Bull. Kor. Chem. Soc.* **31** (2010) 803
24. H. Xu, M. Prasad, S. Qi, Y. Li, *Sci. China Technol. Sci.* **53** (2010) 3014
25. H.-Y. Xu, M. Prasad, Y. Liu, *J. Hazard. Mater.* **165** (2009) 1186
26. S. Tunç, T. Gürkan, O. Duman, *Chem. Eng. J.* **181**–**182** (2012) 431
27. S. Karthikeyan, V. K. Gupta, R. Boopathy, A. Titus, G. Sekaran, *J. Mol. Liq.* **173** (2012) 153
28. İ. Gulkaya, G. A. Surucu, F. B. Dilek, *J. Hazard. Mater.* **136** (2006) 763
29. M. Fathinia, A. R. Khataee, M. Zarei, S. Aber, *J. Mol. Catal., A* **333** (2010) 73
30. A. R. Khataee, M. Safarpour, M. Zarei, S. Aber, *J. Mol. Catal., A* **363**–**364** (2012) 58
31. M. G. Lak, M. R. Sabour, A. Amiri, O. Rabbani, *Waste Manage.* **32** (2012) 1895
32. E. Rosales, M. A. Sanromán, M. Pazos, *Environ. Sci. Pollut. Res.* **19** (2012) 1738
33. R. Idel-aouad, M. Valiente, A. Yaacoubi, B. Tanouti, M. López-Mesas, *J. Hazard. Mater.* **186** (2011) 745
34. W. P. Kwan, B. M. Voelker, *Environ. Sci. Technol.* **37** (2003) 1150
35. H. Che, S. Bae, W. Lee, *J. Hazard. Mater.* **185** (2011) 1355
36. R. Andreozzi, V. Caprio, R. Marotta, *Water Res.* **36** (2002) 2761
37. J. Feng, X. Hu, P. L. Yue, *Environ. Sci. Technol.* **38** (2004) 269
38. H. Wu, X. Dou, D. Deng, Y. Guan, L. Zhang, G. He, *Environ. Technol.* **33** (2012) 1545
39. X. Liang, Y. Zhong, S. Zhu, J. Zhu, P. Yuan, H. He, J. Zhang, *J. Hazard. Mater.* **181** (2010) 112

40. M. Karatas, Y. A. Argun, M. E. Argun. *J. Ind. Eng. Chem.* **18** (2012) 1058
41. M. Azami, M. Bahram, S. Nouri, A. Naseri, *J. Serb. Chem. Soc*. **77** (2012) 235
42. S.-P. Sun, A. T. Lemley, *J. Mol. Catal., A* **349** (2011) 71
43. S. Mohajeri, H. A. Aziz, M. H. Isa, M. A. Zahed, M. N. Adlan, *J. Hazard. Mater*. **176** (2010) 749.

Journal of the Serbian Chemical Society
JSCS-info@shd.org.rs • www.shd.org.rs/JSCS
J. Serb. Chem. Soc. 79 (3) 379–387 (2014)
JSCS–4592
UDC 54.56'47'815'48:556.531:
66.067.9(497.11)(282.243.743)
Short communication

SHORT COMMUNICATION

Transport and storage of heavy metals in the Sava River Basin in Serbia

DUBRAVKA VUKOVIĆ[1], SRBOLJUB J. STANKOVIĆ[2]*, ŽIVORAD VUKOVIĆ[2] and KSENIJA JANKOVIĆ[3]

[1]*Institute of Veterinary Medicine, Vojvode Toze 24, 11000 Belgrade, Serbia,* [2]*Institute of Nuclear Sciences Vinča, University of Belgrade, P. O. Box 502, 11001 Belgrade, Serbia,* [3]*Institute for Testing Materials – IMS, Bulevar Vojvode Mišića 43, 11000 Belgrade, Serbia*

(Received 28 January, revised 21 August 2013)

Abstract: Selected heavy metals (Cu, Zn, Pb and Cd) in the water and sediment of the Sava River in Serbia were investigated from three locations in the vicinity of industrial and urban settlements (Šabac, Obrenovac and Belgrade) during the period spring 2007 to autumn 2011. The fluxes of heavy metals from the river water to the sediment due to sedimentation and heavy metal re-suspension fluxes arising from sediment re-suspension at high flows were determined, by application of a model for the assessment of the transport the pollutants through rivers. These fluxes were attributed mainly to natural processes.

Keywords: flux of heavy metal; river sediment; sediment re-suspension.

INTRODUCTION

Toxic heavy metals have been the subject of many studies, mostly in river systems, due to their toxicity, abundance and persistence in the environment, and subsequent accumulation in aquatic habitats.[1–5] Heavy metals of anthropogenic origin are generally introduced into river systems as inorganic complexes or hydrated ions, which are easily adsorbed on the surfaces of sediment particles through relatively weak physical or chemical bonds. Thus, heavy metals of anthropogenic origin are found predominantly in the labile extractable fraction of a sediment.[6]

Usually, trace metal levels in the sediment display marked seasonal and regional variations, which have been attributed to anthropogenic influences and natural processes.[7,8]

* Corresponding author. E-mail: srbas@vinca.rs
doi: 10.2298/JSC130128085V

The speciation of Cd, Cu, Zn and Pb in sediments showed higher bioavailability compared to the other studied metals, and consequently they posed a greater ecological risk.[9]

The Sava River has not been exposed to anthropogenic influence due to dam construction, which decreases sediment transport through sediment retention in the reservoirs. As an integral and dynamic part of the Sava River Basin, the river sediment originates from upstream weathering of minerals and soils, and is susceptible to transport downstream by the river water. The sediment particles were mostly silt and fine-grained sand composed of calcite, quartz, feldspars, ilite and kaolinite.

In the recent past, attention was paid to the water quality of the Sava River in respect to microbiological, chemical and radiochemical parameters.[10–12] In a previous paper,[13] the results of the distribution and accumulation of heavy metals in the water and sediments of the Sava River displayed seasonal fluctuations, which were attributed mainly to natural processes. The sediment studies were performed mainly because sediments are receptors in water bodies. However, re-suspension of sediments leads to a release of soluble heavy metals in the water body.[14] Hitherto, no relevant method has been suggested to assess and quantify the transport of heavy metals between sediments and the overlying water.[15]

The objective of this study was to quantify the transport and storage of heavy metals in the Sava River Basin in Serbia by determination of the fluxes of heavy metals from the river water to the sediment and their re-suspension fluxes under favourable hydraulic conditions.

EXPERIMENTAL

Three sampling sites were chosen along a 100-km stretch of the Sava River upstream from its confluence with the Danube River. For the experiment, water and sediment samples were taken from three sampling locations along the Sava River (Fig. 1). Location No. 1 is near an industrial area of the town of Šabac. Location No. 2 is downstream of the coal-fired power plant “Nikola Tesla”, where the Kolubara River flows into the Sava River. Location No.3 is at the confluence of the Sava and the Danube, in the wider metropolitan area of Belgrade. A total of 60 water and sediment samples were collected between 2007 and 2011 at six-month intervals to cover both the dry (autumn, at low flow, $q \leq 500$ m^3 s^{-1}) and wet (spring, at high flow, $q \geq 1200$ m^3 s^{-1}) seasons. Ten litre-size water samples were collected from a depth of 50 cm. Sediment samples were collected at the depth of 10 cm from the top of sediment surface. All samples were dried at 105 °C until constant mass was attained. The caked sediment was then finely ground to grains below 1.0 mm in diameter. Samples of the sediment (2.5 g) were dissolved in 25 cm^3 of 1/1 HNO_3.

The concentrations of heavy metals were determined by flame atomic absorption spectrometry in an air/acetylene flow, using a Perkin Elmer AA200 spectrometer.[16] The cadmium concentration was determined by the graphite furnace atomic absorption spectrometry, using a Perkin Elmer AA600 with a transversely-heated graphite atomizer (THGA) using a Zeeman Effect background correction system. The analytical injection (20 µl) and the atomization were undertaken in five steps, controlled by the appropriate software and auto-sampler.

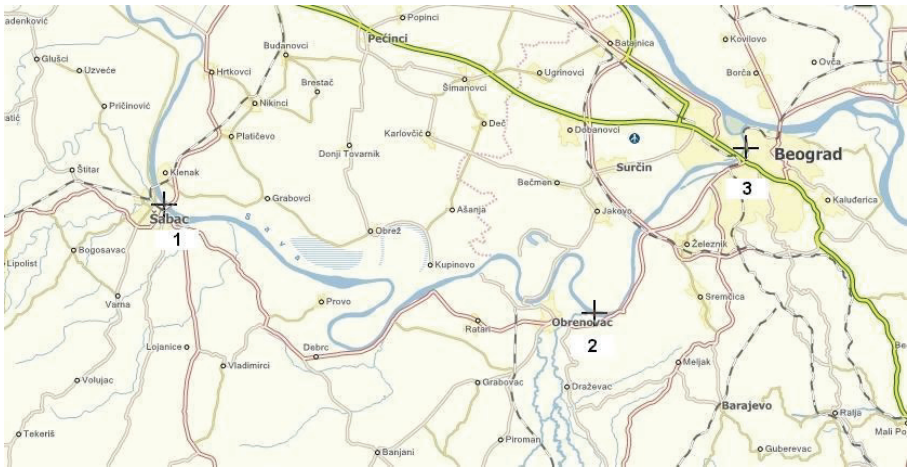

Fig. 1. Location of sampling stations on the Sava River: Šabac – location No. 1, Obrenovac – location No. 2 and Belgrade – location No. 3.

For both techniques, adequate hollow cathode lamps (HCL) were used for irradiation. Mixed reference standard solutions were prepared for the analysis using Merck certified atomic absorption stock standards (1000 μg ml^{-1}) and Milli-Q purified water. No modifiers were added. The quality control (QC) program included reagent blanks, duplicate samples and certified reference materials. The detection limits (DL) for Cu and Zn were 1, for Pb 0.11 and for Cd 0.09 μg dm^{-3}. Measurement errors were less than 5 %.

RESULTS AND DISCUSSION

The minimum, maximum and mean, with standard deviation, concentrations of the heavy metals in the sediments and river water of the studied sites at three locations are presented in Table I for the autumn and spring seasons, respectably. The level of heavy metals in the autumn was higher in comparison to the level in spring. The heavy metal concentrations in the water samples were lower than the maximum permitted concentrations for the protection of aquatic life.[17]

TABLE I. The minimum, maximum and mean concentration of heavy metal in the sediments of the studied sites, for 5 years, from spring 2007 to autumn 2011; total number of sediment samples: 60

Heavy metal (season)	Sediment concentration, mg kg^{-1}		
	Min.	Mean±*SD*	Max.
Zn (spring)	34.5	51.9±18.6	64.8
Zn (autumn)	47.2	62.5±19.7	88.6
Cu (spring)	25.1	41.3±16.2	56.0
Cu (autumn)	28.2	47.5±16.2	72.3
Pb (spring)	13.9	18.1±3.8	22.6
Pb (autumn)	14.7	27.6±12.8	48.2
Cd (spring)	2.8	4.1±2.3	6.9
Cd (autumn)	3.9	4.9±2.7	8.6

A common approach to characterize the partition of an element between the particulate and the dissolved phase is the use of an empirical equilibrium – such as an expression connects dissolved and particulate concentrations *via* the partition coefficient (K_d). Although K_d is not a true thermodynamic mass action constant, it represents a straightforward and easy approach to describe partitioning between dissolved and particulate phases.[19]

The distribution of heavy metals between different phases gives the opportunity to estimate the fluxes of heavy metals from water to sediment due to sedimentation and heavy metals fluxes from the sediment to water due to sediment re-suspension and direct exchange of heavy metals from the sediment to water. The flux of heavy metal migrating to sediment due to sedimentation is given by:[18]

$$F_{ws} = S_f K_d c_w \quad (1)$$

where: F_{ws} is the flux of a heavy metal migrating to the sediment due to sedimentation, S_r is the net sedimentation rate (kg m^{-2} s^{-1}), $K_d = c_s c_w^{-1}$; and c_s (mg kg^{-1}) and c_w (mg m^{-3}) are the concentrations of heavy metals in the sediment and river water, respectively. The flux from water to sediment was calculated according to Eq. (1) using 1.0×10^{-6} m s^{-1} as the value for the sedimentation velocity, taken from modelling studies.[19,20]

The fluxes of heavy metals on a yearly level comprised two fluxes: the flux from water to sediment (F_{wsa} (kg m^{-2} y^{-1}) and the re-suspension fluxes from the deposited sediment to the sediment water interface F_{srs} (kg m^{-2} y^{-1}). The yearly fluxes of the heavy metals from water to the sediment, as well as the fluxes due to sediment re-suspension from the bottom sediment, calculated as the difference of the fluxes F_{ws} at the low flow regime (below 3 m s^{-1}) and the same fluxes at the high flow regime, are presented in Figs. 2a and b (for site 1), 3a and b (for site 2) and 4a and b for site 3. The F_{srs} fluxes were much lower than the F_{wsa} fluxes, because the high flow regime lasted, yearly, between 1.5 and 3.0 months. Re-suspension of the sediment at a high flow, which resulted in the movement of heavy metals between the sediment and overlying water, apparently does not deteriorate the water quality (Table II) but increase the transport of heavy metals by the suspended sediment to the Danube River. The fluxes of heavy metals to the Sava River sediments (Figs. 2–4) were lower than the reported fluxes in the reservoir and lake sediments derived from industrial sites within the watershed.[21,22]

The heavy metal levels in the sediments were greatly reduced due to the transfer of suspended and re-suspended load. Suspension load of sediments in water varies broadly depending on characteristics of the river considered. For the Sava River, with an average flow rate of 1100 m^3 s^{-1}, the suspension load at its confluence is 1.0 10^{-1} kg m^{-3} or 3.5 10^6 t y^{-1}.[23] The distribution coefficients at

high flow were lower in the wet season than in the dry season, due to the re-suspension of the bottom sediment. A high flow rate did not prevent the storage of heavy metals in the sediments, but reduced their accumulation quantity, depending on the duration of the high water regime ($0 \leq F_{srs} \leq 10$ %, Figs. 2–4). The F_{srs} fluxes showed that the sediments would become a source of heavy metals to overlying water if hydraulic changes occurred in the Sava River.

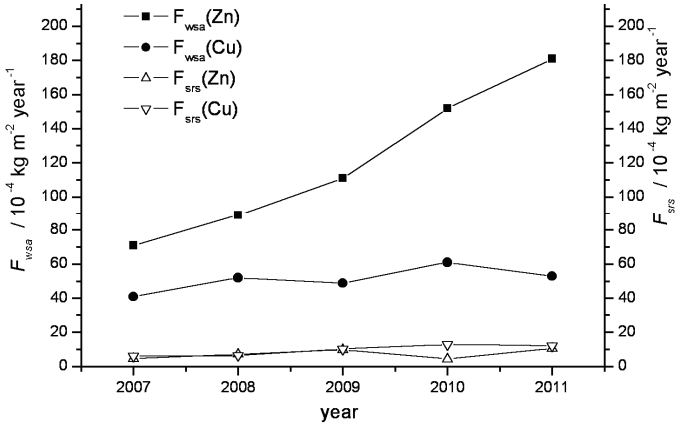

(a)

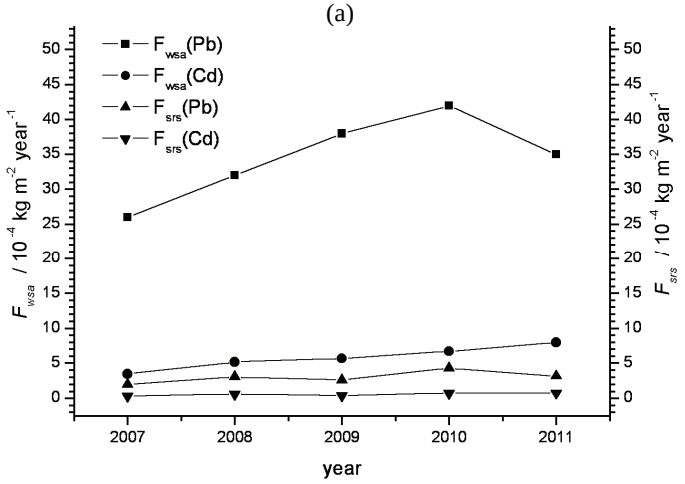

(b)

Fig. 2. The fluxes F_{wsa} / kg m^{-2} y^{-1} and F_{srs} / kg m^{-2} y^{-1} of a) Zn and Cu and b) Pb and Cd for location No. 1 in the five-year period.

The New Serbian Official Regulation on limiting values for pollutants in surface and ground waters and sediments[24] for the first time regulated the limiting values of heavy metals in sediments. By definition, sediment is an essential, dynamic and solid component of aquatic ecosystems, which, due to the strong

tendency to bind pollutants, becomes a reservoir of toxic and persistent compounds of anthropogenic origin.

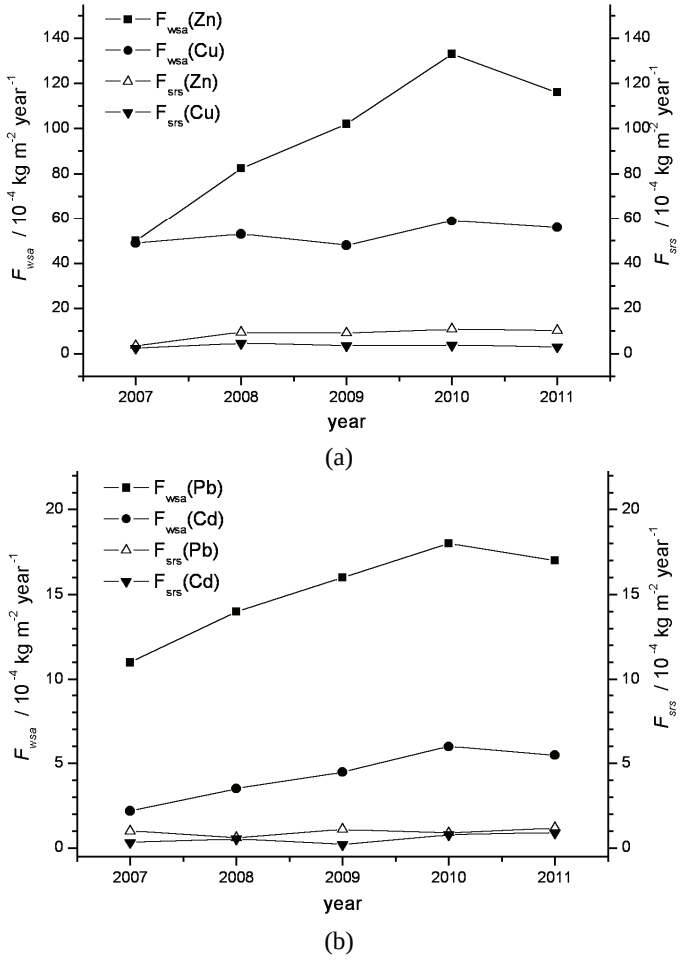

Fig. 3. The fluxes F_{wsa} / kg m^{-2} y^{-1} and F_{srs} / kg m^{-2} y^{-1} of a) Zn and Cu and b) Pb and Cd for location No. 2 in the five-year period.

The obtained results showed that anthropogenic input of heavy metals in the environment of the Sava River Basin in Serbia was not in known amounts. No high variability in analytical data obtained is indicative of modest external sources of heavy metals in the sediment and surface water, mainly due to poor regional industrial activity. An increase of F_{wsa} would be an indicator of the anthropogenic origin of heavy metals in Sava River Basin, because as mass accumulation fluxes they could quantify the contribution of human activities. The fluxes F_{wsa} and F_{srs} were not previously determined.

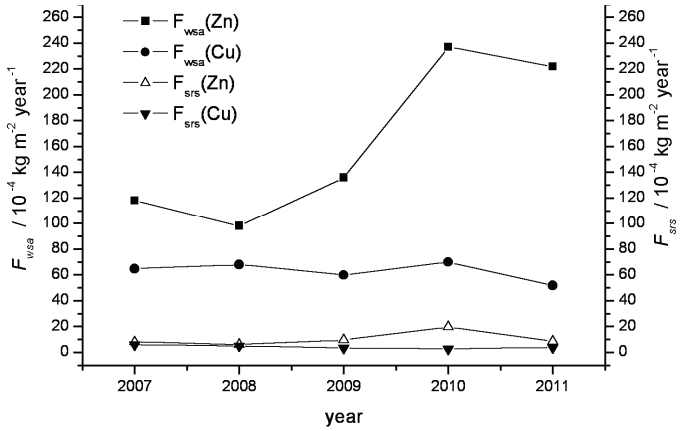

(a)

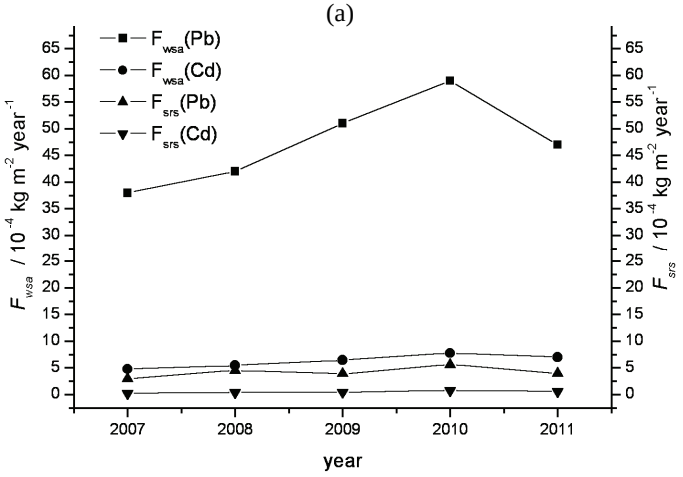

(b)

Fig. 4. The fluxes F_{wsa} / kg m^{-2} y^{-1} and F_{srs} / kg m^{-2} y^{-1} of a) Zn and Cu and b) Pb and Cd for location No. 3 in the five-year period.

TABLE II. The minimum, maximum and mean concentration of heavy metal in the river water of the studied sites, for 5 years, from spring 2007 to autumn 2011; total number of sediment samples: 60

Heavy metal (season)	River water concentration, mg m^{-3}		
	Min.	Mean±*SD*	Max.
Zn (spring)	19.3	49.3±16.8	61.4
Zn (autumn)	24.3	45.3±26.5	78.4
Cu (spring)	7.1	17.3±9.9	29.2
Cu (autumn)	9.2	20.1±11.2	33.6
Pb (spring)	2.2	4.6±2.2	6.3
Pb (autumn)	2.9	4.8±2.1	6.7
Cd (spring)	0.3	0.7±0.3	0.9
Cd (autumn)	0.4	1.3±1.1	4.1

CONCLUSIONS

The performed analyses of heavy metals in the Sava River water and sediment at three selected sites in Serbia showed that their accumulation in the sediments was predominantly influenced by natural factors. The fluxes of heavy metals from the river water to the sediments and heavy metal re-suspension fluxes due sediment re-suspension under favourable hydraulic conditions were determined. The study indicated that the Sava River sediment is a sink for heavy metals, but also the source of heavy metal transfer to the water column under favourable hydraulic condition. At high flow, fluvial erosion occurs and removes part of the previously deposited heavy metals from the sediments.

Acknowledgement. This work was provided with financial support by the Ministry of Education, Science and Technological Development of the Republic of Serbia, under Project No. 43009.

И З В О Д

ТРАНСПОРТ И СКЛАДИШТЕЊЕ ТЕШКИХ МЕТАЛА У БАЗЕНУ РЕКЕ САВЕ

ДУБРАВКА ВУКОВИЋ[1],СРБОЉУБ СТАНКОВИЋ[2], ЖИВОРАД ВУКОВИЋ[2] и КСЕНИЈА ЈАНКОВИЋ[3]

[1]Институт ветеринарске медицине, Војводе Тозе 24, Београд, [2]Институт за нуклеарне науке „Винча“, Београд и [3]Институт за испитивање материјала – ИМС,Војводе Мишића 43,Београд

Испитивани су изабрани тешки метали (Cu, Zn, Pb и Cd) у речном систему Саве на три локације у близини индустријских и урбаних насеља (Шабац,Обреновац и Београд) у периоду пролеће 2007.–јесен 2011.године. Одређени су флуксеви тешких метала из воде у седимент, као и повратни флуксеви из седимента због ресуспензије седимента у воду при високом протоку, применом модела за процену транспорта полутаната у реци. Ови флуксеви потичу првенстено од природних извора.

(Примљено 28. јануара, ревидирано 21. августа 2013)

REFERENCES

1. K. P. Sing, D. Mohan, V. K. Singh, A. Malik, *J. Hydrol.* **312** (2005) 14
2. B. Xu, X. Yang, Z. Gu, Y. Zhang, Y. Chen, Y. Lv, *Chemosphere* **75** (2009) 442
3. A. Naji, A. Ismail, A. R. Ismail, *Microchem. J.* **95** (2010) 285
4. M. Varol, B. Sen. *Catena* **92** (2012) 1
5. S. M. Sakan, D. S. Djordevic, D. D. Manojlovic, P. S. Polic, *J. Environ. Manag*. **90** (2009) 3382
6. K. P. Sing, A. Malik, N. Basant V. K. Singh, A. Basant, *Chemom. Intell. Lab. Syst.* **87** (2007) 185
7. A. L. Tuna, F. Yilmaz, A. Demirak, N. Ozdemir, *Environ. Monit. Assess*. **125** (2007) 47
8. D. Karamanis, K. Stamoulis, K. Ionaidis, D. Patius, *Desalination* **224** (2008) 250
9. Z. Yang, Y. Wang, Z. Shen, J. Niu, Z. Tang, *J. Hazard. Mater.* **166** (2009) 1186
10. V. Orescanin, L. Mikelic, S. Lulic, G. Pavlovic, N. Coumbassa, *Nucl. Instrum. Methods, B* **263** (2007) 85
11. S. Murko, R. Milacic, M. Veber, J. Scancar, *J. Serb. Chem. Soc*. **75** (2010) 113
12. Z. Vukovic, Lj. Markovic, M. Radenkovic, D. Vukovic, S. J. Stankovic, *Arh. Hig. Rada Toksicol*. **63** (2011) 13

13. Z. Vukovic, M. Radenkovic, S. J. Stankovic, D. Vukovic, *J. Serb. Chem. Soc*. **76** (2011) 795
14. Y. Song, J. Ji, Z. Yang, X. Yuan, C. Mao, R. L. Frost, G. A. Ayoko, *Catena* **85** (2011) 73
15. H. S. Chon, D. H. Ohandja, N. Voulvoulis, *Chemosphere* 2012
16. *Standard methods for the Examination of Water and Wastewater*, 19th ed., A. E Greenberg, Ed., American Public Health Association, Washington DC, 1995
17. *Regulations on the hygienic correctness of drinking water*, Official gazette of the FRY **42** (1998) (in Serbian)
18. S. Audry, G. Blanc, J. Schafer, *Sci. Total Environ.* **319** (2004) 197
19. L. Monte, P. Boyer, J. E. Brittain, L. Hakanson, S. Lepicard, J. T. Smith, *J. Environ. Radioact.* **79** (2005) 273
20. S. Audry, J. Schafer, G. Blanc, J. M. Jonannean, *Sci. Total Environ.* **132** (2004) 413
21. J. G. Arnason, B. A. Fletcher, *Environ. Pollut.* **123** (2003) 383
22. H. Bing, Y. Wu, Z. Sun, S. Yao, *J. Environ. Sci.* **23** (2011) 1671
23. M. Babic-Mladenovic, *Sediment regime of the Danube River*, Foundation Andrejevic, Belgrade, 2007
24. *Regulation on limit values for pollutants in surface and ground waters and sediments, and the deadlines for their achievement, Serbian Official Gazette* **50** (2012) 1 (in Serbian).